Climate Variability and Trend on Interannual-to-Centennial timescales

from Global Observations and Atmosphere-Ocean Model Simulations

by

Houk Paek

A Dissertation Presented in Partial Fulfillment
of the Requirements for the Degree
Doctor of Philosophy

Approved March 2013 by the
Graduate Supervisory Committee:

Huei-Ping Huang, Chair
Ronald Adrian
Zhihua Wang
James Anderson
Marcus Herrmann

ARIZONA STATE UNIVERSITY

May 2013

ABSTRACT

The numerical climate models have provided scientists, policy makers and the general public, crucial information for climate projections since mid-20th century. An international effort to compare and validate the simulations of all major climate models is organized by the Coupled Model Intercomparison Project (CMIP), which has gone through several phases since 1995 with CMIP5 being the state of the art. In parallel, an organized effort to consolidate all observational data in the past century culminates in the creation of several "reanalysis" datasets that are considered the closest representation of the true observation. This study compared the climate variability and trend in the climate model simulations and observations on the timescales ranging from interannual to centennial. The analysis focused on the dynamic climate quantity of zonal-mean zonal wind and global atmospheric angular momentum (AAM), and incorporated multiple datasets from reanalysis and the most recent CMIP3 and CMIP5 archives. For the observation, the validation of AAM by the length-of-day (LOD) and the intercomparison of AAM revealed a good agreement among reanalyses on the interannual and the decadal-to-interdecadal timescales, respectively. But the most significant discrepancies among them are in the long-term mean and long-term trend. For the simulations, the CMIP5 models produced a significantly smaller bias and a narrower ensemble spread of the climatology and trend in the 20th century for AAM compared to CMIP3, while CMIP3 and CMIP5 simulations consistently produced a positive trend for the 20th and 21st century. Both CMIP3 and CMIP5 models produced a wide range of the magnitudes of decadal and interdecadal variability of wind component of AAM (M_R) compared to observation. The ensemble means of CMIP3 and CMIP5 are not statistically

distinguishable for either the 20th- or 21st-century runs. The in-house atmospheric general circulation model (AGCM) simulations forced by the sea surface temperature (SST) taken from the CMIP5 simulations as lower boundary conditions were carried out. The zonal wind and M_R in the CMIP5 simulations are well simulated in the AGCM simulations. This confirmed SST as an important mediator in regulating the global atmospheric changes due to GHG effect.

DEDICATION

To my family

ACKNOWLEDGMENTS

TABLE OF CONTENTS

Page

LIST OF TABLES

LIST OF FIGURES

Chapter 1

1   INTRODUCTION

Human beings have tried to understand and predict the weather and climate for centuries. The rigorous numerical physical-mathematical modeling and simulation of climate owing to the invention of electric computer have played important roles in the modern weather forecast and climate projection since mid-20th century. Statistical and empirical approaches looking for recurring weather and climate patterns from the past have also been developed.

The climate changes such as temperature change, precipitation change, extreme events and sea level rise will impact significantly on water resources, food security, settlements, society and ecosystem. Improved scientific understanding of the climate due to the technical advancement will substantially contribute to the economy and society of the nations in the world.
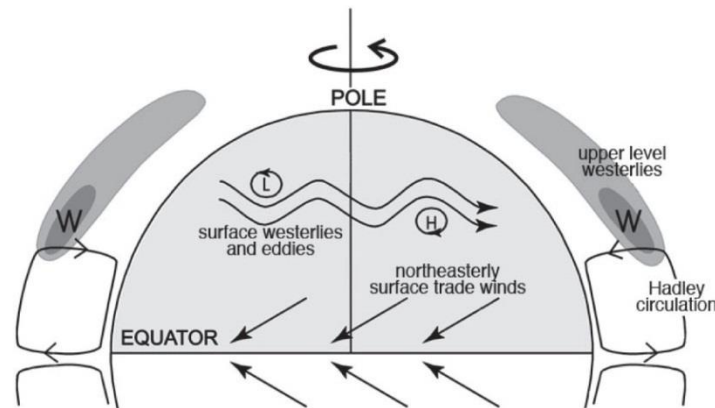
Figure 1: Schematic of the observed atmospheric general circulation for annual averaged conditions. The upper level westerlies (eastward wind) are shaded to reveal the core of the subtropical jet stream on the poleward flank of the Hadley circulation. The surface westerlies and surface trade winds are also marked, as are the highs and lows of middle latitudes. Only the northern hemisphere is shown. The vertical scale is greatly exaggerated (Marshall and Plumb 2007).

The climate is governed by the general circulation of the atmosphere, ocean and their interaction. The climate models numerically solve the equations of conservation of momentum, continuity and thermodynamic energy over three dimensionally discretized global domain (see Figs. 1 and 2).
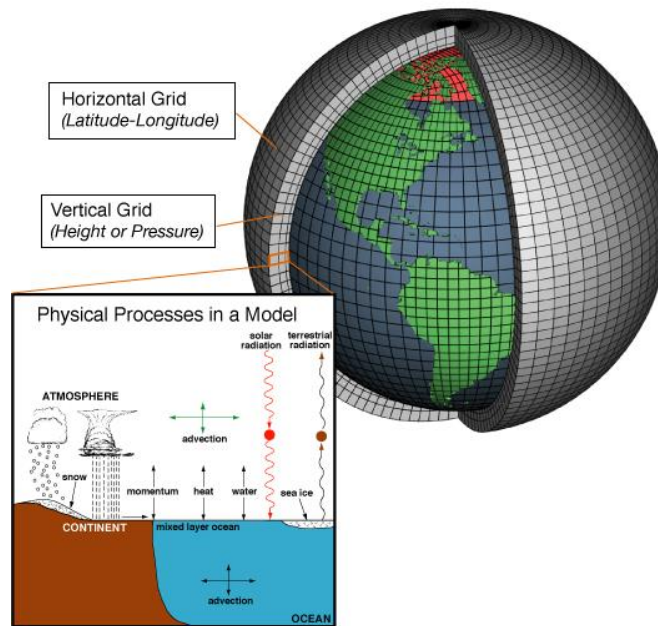
Figure 2: Schematic representation of the component of climate system and their interaction, and the 3-dimensional discretization of the earth (National Oceanic and Atmospheric Administration).

The atmospheric general circulation models (AGCMs; Kasahara and Washington 1967, Manabe et al. 1965, Mintz 1965, Smagorinsky et al. 1965) and the ocean general circulation models (OGCMs; Bryan 1969, Cox 1970) were firstly developed in the United States. The coupled ocean-atmosphere general circulation model (AOGCM) was created by Manabe et al. (1975) and Bryan et al. (1975). Based on these fundamental models, many models were developed in 1970-1980s in different modeling groups over

the world. The AOGCM are now the standard for long-term climate simulations (Meehl et al. 2007, Talyor et al. 2012).

Under the umbrella of the World Climate Research Programme (WRCP)'s Working Group on Coupled Modelling (WGCM), the Program for Climate Model Diagnosis and Intercomparison (PCMDI) has volunteered to collect standard sets of the centennial climate simulations from modeling groups around the world, and has released the data to climate research community since 1995. This unique data archive is organized by the Coupled Model Intercomparison Project (CMIP). More than 20 modeling groups in more than 10 countries participate in producing simulations for CMIP. The CMIP phase 3 (CMIP3; Meehl et al. 2007) collected 36 TB of simulation datasets and the phase 5 (CMIP5; Talyor et al. 2012) collected 1483 TB. The data archive is widely used for climate research. For example, more than 250 journal articles till 2007 were published using CMIP3 data.

Meanwhile, the Intergovernmental Panel on Climate Change (IPCC) established by the World Meteorological Organization (WMO) and the United Nations Environmental Program (UNEP) publishes assessment reports on the current state of the science, which are widely used for policy making over the world. The latest Fourth Assessment Report of IPCC (AR4; IPCC 2007) was published in 2007 using CMIP3 archive, and the Fifth Assessment Report (AR5) will be published based on CMIP5 archive in 2013.
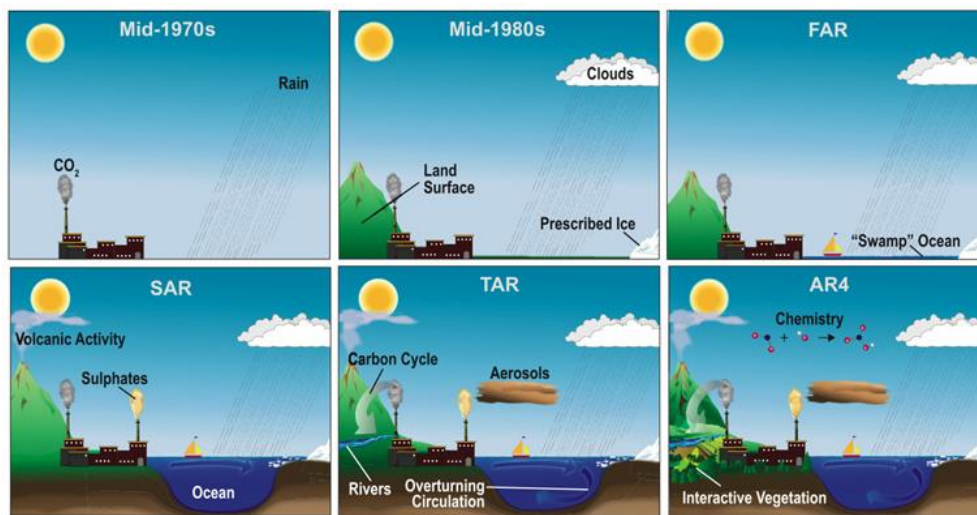
Figure 3: The complexity of climate models has increased over the last few decades. The additional physics incorporated in the models are shown pictorially by the different features of the modeled world. FAR stands for the First Assessment Report (IPCC 1990), SAR for the Second Assessment Report (IPCC 1996), TAR for the Third Second Assessment Report (IPCC 2001) and AR4 for the Fourth Assessment Report (IPCC 2007).
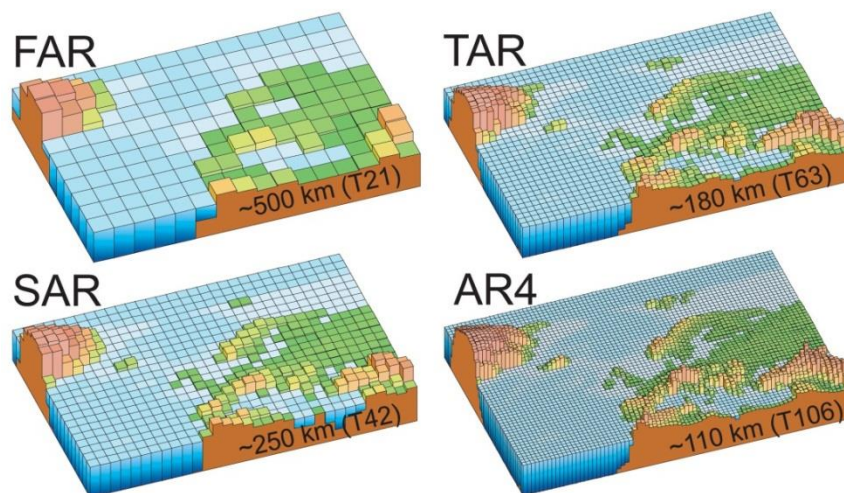
Figure 4: Horizontal resolutions and geographic representation of the generations of climate models used in the IPCC Assessment Reports (IPCC 2007).

The features of CMIP models such as the complexity of the components, spatial resolutions and parameterization schemes have been improved from generation to generation (see Figs. 3 and 4). The most recent CMIP3 and CMIP5 incorporated many key techniques unavailable to the previous generations of the models. For example, the majority of the model in CMIP3 can produce a reliable long term climatology without "flux correction" (Sausen et al. 1988, Manabe et al. 1991) for air-sea interaction (Meehl el al. 2007), and the "Earth System" models in CMIP5 are among the first generation to have dynamic treatments for global biogeochemical cycle (Taylor et al. 2012).

It is understood that the global AOGCM including CMIP models still contains inherent error and biases, not least because of its heavy reliance on subgrid-scale (SGS) parameterizations (e.g., Covey et al. 2003) due to the relative coarse resolution adopted by the models (e.g., Fig. 4), but the validation of models by observation and other models has not been done well due to the lack of computer and human resources. At the same time, the analysis of CMIP simulations is widely used for policy making (e.g., based on IPCC 2007).

In this sense, a systematic validation, diagnosis, and intercomparison of the climate models are important for the following purposes :

1) Identifying the common biases in climate models as a way to help assessing the mechanisms responsible for model differences in poorly understood feedbacks associated with external and boundary forcing.

2) Quantifying the reliability of the global reanalysis data as a representation of the true observation, and assessing the feasibility of using them to deduce 20th century climate trend.

3) Assessing the realism of the climate variability and trends over the 2nd half of the 20th century in climate model simulations.

In parallel, several reanalysis datasets have been created since the NCEP/NCAR Reanalysis I (Kalnay et al. 1996), assimilating various observational data using a frozen numerical model, and spanning the timeseries for several decades. The reanalysis dataset has been served as a valuable basis for climate research. The recent construction of the 20th Century Reanalysis (20CR) dataset (Compo et al. 2011) spanning from 1871 to date, presented an opportunity to meaningfully validate CMIP simulations on the decadal-to-interdecadal timescales while the other datasets cover only the 2nd half of 20th century. Despite the recent interest in this decadal-to-interdecadal variability (e.g., Meehl et al. 2009) filling a gap between seasonal forecast and climate projections, there has been limited progress because one can extract only a small number of degrees of freedom for decadal/interdecadal oscillations from the short observational record before 20CR.

A unique but less understood interdecadal event in 20th century is the 1976/77 climate regime shift (e.g., Trenberth 1990, Miller et al. 1994, Huang et al. 2005), at which the atmospheric and ocean state changed from one regime to another with a large amplitude at a short period (e.g., shift in atmospheric angular momentum; Fig. 5). Understanding this event is important for the near-term prediction (10-30 years) because the magnitude of the shift can be comparable or overwhelm the long-term trend induced by greenhouse gas (GHG) forcing (Meehl et al. 2009). The recent recognition of this point led to introduction of new suites of simulations called "Decadal prediction experiment" for near-term integration in CMIP5 (Talyor et al. 2012).

6
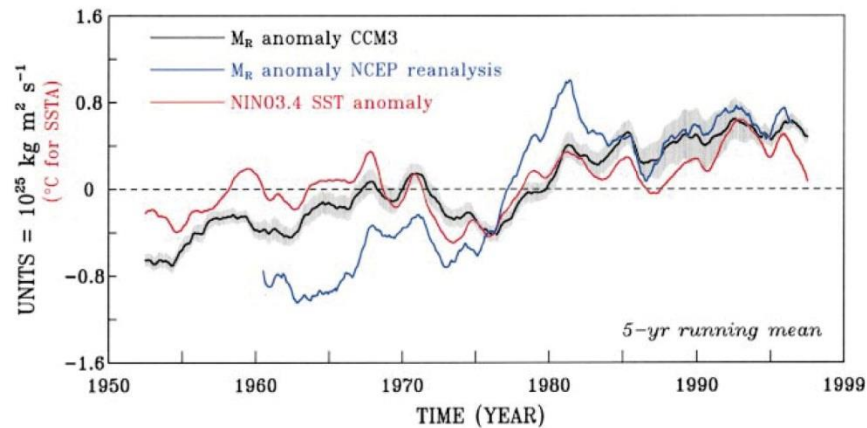
Figure 5: The 5-yr running means of the monthly mean timeseries of globally integrated atmospheric (relative) angular momentum (M_R) from observation (blue) and from AGCM simulations (black) with observed global sea surface temperature (SST) (red is Nino3.4 index) (Huang et al. 2003). The shift in M_R of NCEP reanalysis (0.6×10^{25} kg m^2 s^{-1}) is comparable to that of CMIP3 20th century simulations (0.5×10^{25} kg m^2 s^{-1}).

The idealized forcing experiments have been central to CMIP simulations to understand the climate response to natural and anthropogenic forcings (e.g., increased surface temperature and sea level rise under GHG forcing; IPCC 2007). Many studies still use either AGCM or OGCM to analyze the relation between the response of the atmosphere or ocean to the specific forcing (e.g., stratospheric ozone recovery of Polvani et al. 2011) because simplification of model and isolation of a component help in interpreting their interaction and finding an underlying mechanism. This approach is computationally, less costly.

Given this background, the main objectives of this research is to answer the following questions :

7

1) How confident are we on the quality of the reanalysis data that is used for major climate assessments despite only being a partial representation of the real observation?

2) How well do state-of-the-art climate models reproduce the observed climate variability and trend in the 20th century? How does the model bias depend on the timescale of the variability? How diverse are the behaviors of the individual climate models in their simulations of the low-frequency variability?

3) How well does an AGCM forced by SST of CMIP simulations reproduce the dynamic response of the original CMIP simulations? Does an AGCM simulation help in interpretation of the relation between the response and the forcing, and finding an underlying mechanism?

The analysis will help us quantify the interplay between interannual-to-multidecadal variability and long-term trend in climate models and understand the dynamics and predictability of climate shift events. The expected outcome will have practical implications for both near-term and centennial climate prediction.

This dissertation is outlined as follows. Chapter 2 describes the observational datasets used in this study, followed by an introduction to climate modeling and Coupled Model Intercomaprison Project (CMIP) in Chapter 3. Chapter 4 discusses the climate indices that are used for the validation and intercomparison of the data. In Chapter 5 and 6, the climate variability and trend on the interannual-to-centennial timescales in reanalysis datasets are inter-compared and validated with geodetic measurement of length-of-day. Chapter 7 consists of a comprehensive intercomparison and validation of

climate model simulations of decadal-to-interdecadal variability and trend. In Chapter 8, CMIP simulations under GHG forcing will be compared to AGCM simulations forced by SST of the CMIP simulations. The goal is to understand the dynamic response of the atmosphere to SST trend induced by GHG forcing. The annual-to-decadal predictability using CMIP5 Decadal simulations will be discussed in Chapter 9. A summary of accomplishments of this study is in Chapter 10.

Chapter 2

2   OBSERVATIONS AND REANALYSIS

2.1   Reanalysis

Reanalysis is a synthetic approach for constructing a physically consistent long-term global climate record, by assimilating historical observational data from different sources such as in-situ observations, satellite, and aircraft measurements using a frozen state-of-the-art numerical model. The reanalysis datasets have been served as a valuable basis for climate research. This study considers only atmospheric reanalysis, which contains 2-D variables such as precipitation, sea level pressure, surface temperature, and 3-D variables such as wind, air temperature, geopotential height in rectangular or Gaussian grids.

Since the inception of NCEP/NCAR Reanalysis I (Kalnay et al. 1996, Kistler et al. 2001), several reanalysis datasets have been created as summarized in Table 1. They were constructed by using different numerical models with different spatial resolutions and parameterization schemes. The reanalysis models also used different approaches in air-sea coupling and data assimilation, ranging from three dimentional variational scheme (3D-Var; e.g., Courtier et al. 1998), to 4D-Var (e.g., Courtier et al. 1994, Veerse and Thepaut 1998; used in ERA-Interim) and Ensemble Kalman Filter (EnKF; e.g., Whitaker et al. 2004; used in 20CR). The 20CR dataset assimilated only surface observations (Whitaker et al. 2004) while all other datasets assimilated the full 3-D field observations. These differences are expected to lead to differences in the assimilated meteorological fields in the final products of reanalysis. It is therefore important to analyze these differences in order to assess the reliability of reanalysis.

10

Table 1: A summary of the reanalysis datasets used in this work.

Name	Time coverage	Resolution	Assimilation	Reference
NCEP/NCAR Reanalysis I (NCEP R-1) [1]	1948/01-present	2.5°×2.5° 17 lev.(10-1000 hPa)	3D-VAR	Kalnay et al. 1996, Kistler et al. 2001
NCEP-DOE Reanalysis II (NCEP R-2) [1]	1979/01-present	2.5°×2.5° 17 lev.(10-1000 hPa)	3D-VAR	Kanamitsu et al. 2002
NCEP Climate Forecast System Reanalysis (CFSR) [2]	1979/01-present	0.5°×0.5° 38 lev.(1-1000 hPa)	3D-VAR	Saha et al. 2010
20th Century Reanalysis (20CR) [1]	1871/01-2010/12	2.0°×2.0° 24 lev.(10-1000 hPa)	EnKF	Compo et al. 2006, 2011
ERA 40 year Reanalysis (ERA-40) [3]	1957/09-2002/08	2.5°×2.5° 23 lev.(1-1000 hPa)	3D-VAR	Uppala et al. 2005
ERA Interim Reanalysis (ERA-Interim) [3]	1979/01-present	1.5°×1.5° 37 lev.(1-1000 hPa)	4D-VAR	Dee et al. 2011
Japanese 25-year Reanalysis (JRA-25) [4]	1979/01-present	1.25°×1.25° 23 lev.(0.4-1000 hPa)	3D-VAR	Onogi et al. 2007
NASA Modern Era Reanalysis for Research and Applications (MERRA) [5]	1979/01-present	0.667°×0.5° 42lev.(0.1-1000 hPa)	3D-VAR	Rienecker et al. 2011

The datasets were archived at :

[1] NOAA ESRL/PSD web archive (www.esrl.noaa.gov/psd)

[2] CISL Research Data Archive (http://dss.ucar.edu)

[3] NOAA ESRL/PSD web archive (www.esrl.noaa.gov/psd)

[4] JRA-25 website (http://jra.kishou.go.jp/JRA-25)

[5] CMIP5 Data Portal (http://pcmdi3.llnl.gov).

2.2   Length of day (LOD) dataset

The total angular momentum consisting of the momentum of the solid earth and that of the atmosphere, is nearly conserved (e.g., Peixoto and Oort 1992). Using this conservative property, the complicated atmospheric large-scale motion can be validated

by the independent measurement of length-of-day (LOD) dataset. The details will be discussed in the sections 4.1 and 4.2.
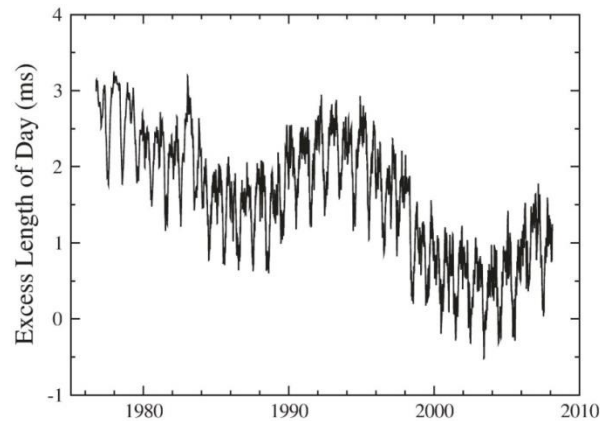
Figure 6: Excess length-of-day as given by the combined Earth orientation series, COMB2007 (Ratcliff and Gross 2009).

Independent Earth orientation measurements taken by the space-geodetic techniques of lunar and satellite laser ranging, very long baseline interferometry, and the Global Positioning System have been combined using a Kalman filter. The resulting combined Earth orientation series, SPACE2007, consists of values and uncertainties for Universal Time, polar motion, and their rates that span from September, 1976 to March, 2008. COMB2007 extends SPACE2007 by additionally incorporating the optical astrometric polar motion and UT1 series, and their rates span from January, 1962, to March, 2008 (Ratcliff and Gross 2009). The dataset can be obtained at ftp://euler.jpl.nasa.gov/keof/combinations/2007.

2.3   Reconstructed Sea Surface Temperature (SST)

The "Reconstructed SST" is a product that resulted from the assimilation and interpolation of observed sea surface temperature and sea ice concentration spanning over the last century. The Met Office Hadley Centre's sea ice and sea surface temperature dataset (HadISST; obtained at http://www.metoffice.gov.uk/ hadobs/hadisst/) is one of the products on a 1° lat.-lon. global grid from 1870 to date. The temperatures are reconstructed using a two-stage reduced space optimal interpolation procedure (RSOI; Kaplan et al. 1997) based on EOF techniques, followed by superposition of quality-improved gridded observations onto the reconstructions to restore local detail. The sea ice fields are made more homogeneous by compensating satellite microwave-based sea ice concentrations for the impact of surface melt effects on retrievals in the Arctic and for algorithm deficiencies in the Antarctic and by making the historical in situ concentrations consistent with the satellite data. SSTs near sea ice are estimated using statistical relationships between SST and sea ice concentration (Rayner et al. 2003).
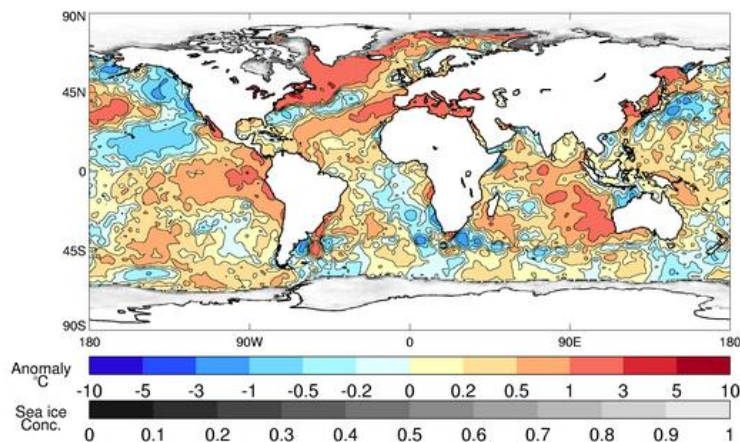
Figure 7: SST anomaly and sea ice concentration in June 2012 from HadISST (http://www.metoffice.gov.uk/hadobs/hadisst/).

In this study, Kaplan Extended SST anomalies Version 2 (Kaplan SST) on 5 °lat.-lon. grid from 1856 to present (Kaplan et al. 1998; http://iridl.ldeo.columbia.edu/ SOURCES/.KAPLAN/.EXTE-NDED/.v2/) and the National Oceanic and Atmospheric Administration (NOAA) Extended Reconstructed SST Version 3 (ERSST) on 2 °lat.-lon. grid from 1854 to present (Smith et al. 2007; http://www.esrl.noaa.gov/psd/ data/gridded/data.noaa.ersst.html) will also be used.

The SST data served as the lower boundary conditions for the production of atmospheric reanalysis and for AGCM simulations. The datasets themselves are used to evaluate the coupled AOGCMs and to improve the understanding of natural and human-induced climatic variations.

Chapter 3

3 CLIMATE MODELING AND COUPLED MODEL INTERCOMPARISON PROJECT (CMIP)

3.1 Climate modeling

The climate is governed by the general circulation of the atmosphere, the ocean, and the interactions between components including land and sea ice. Climate modeling is a numerical approach to solve the equations of conservation of momentum, continuity and thermodynamic energy and the equation of state, forward in time, over 3-D discretized global domain (see Fig. 2).

The primitive equations on the large-scale motion in the atmosphere and the ocean in spherical coordinate system including the Coriolis force are given as :

$$\frac{du}{dt} - \left(f + u\frac{\tan\varphi}{a}\right)v = -\frac{1}{a\cos\varphi}\frac{1}{\rho}\frac{\partial p}{\partial \lambda} + F_\lambda ,$$ (3.1)

$$\frac{dv}{dt} + \left(f + u\frac{\tan\varphi}{a}\right)u = -\frac{1}{\rho a}\frac{\partial p}{\partial \varphi} + F_\varphi ,$$ (3.2)

$$g = -\frac{1}{\rho}\frac{\partial p}{\partial z} ,$$ (3.3)

$$\frac{\partial \rho}{\partial t} = -\frac{1}{a\cos\varphi}\left[\frac{\partial}{\partial \lambda}(\rho u) + \frac{\partial}{\partial \varphi}(\rho v\cos\varphi)\right] - \frac{\partial}{\partial z}(\rho w) ,$$ (3.4)

$$C_p\frac{dT}{dt} - \frac{1}{\rho}\frac{dp}{dt} = Q ,$$ (3.5)

$$p = \rho R T ,$$ (3.6)

with

$$\frac{d}{dt} = \frac{\partial}{\partial t} + \frac{u}{a\cos\varphi}\frac{\partial}{\partial \lambda} + \frac{v}{a}\frac{\partial}{\partial \varphi} + w\frac{\partial}{\partial z}$$ (3.7)

and

$$u = a\cos\varphi\frac{d\lambda}{dt}, \quad v = a\frac{d\varphi}{dt}, \quad u = \frac{dz}{dt}$$ (3.8)-(3.10)

where, λ, φ and z are the longitudinal, latitudinal and vertical direction, respectively, u v, and w represents the wind in λ, φ and z directions, t is the time, ρ is the density, p is the pressure, T is the temperature, R is the gas constant, f is the Coriolis parameter ($2\Omega sin\ \varphi$), Ω is the rotational speed of the earth, F_λ and F_φ are the frictional forces in λ and φ directions, and Q is the diabatic heating term.
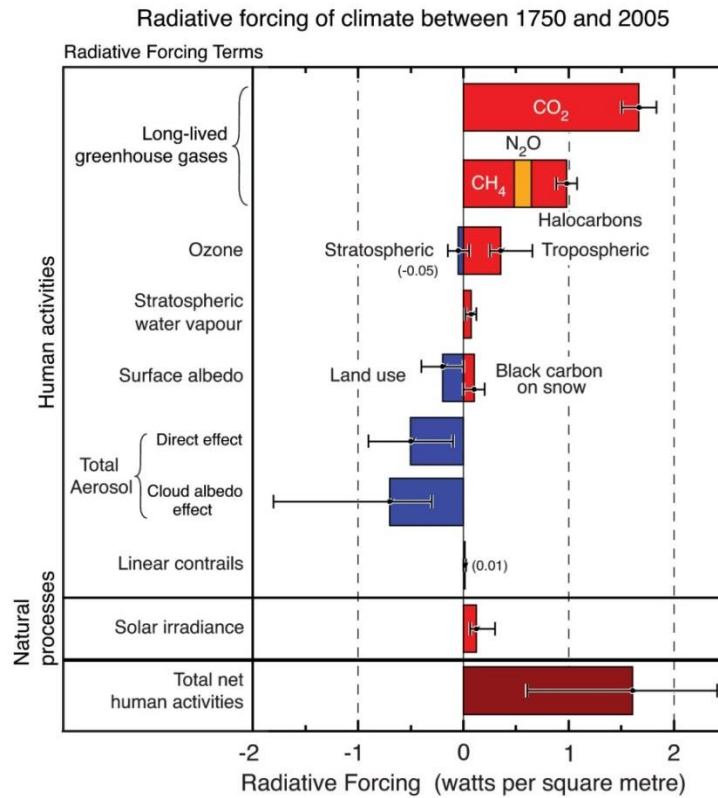
Figure 8: Summary of the principal components of the radiative forcing of climate change. All these radiative forcings result from one or more factors that affect climate and are associated with human activities or natural processes as discussed in the text. The values represent the forcings in 2005 relative to the start of the industrial era (about 1750). Human activities cause significant changes in long-lived gases, ozone, water vapour, surface albedo, aerosols and contrails. The only increase in natural forcing of any significance between 1750 and 2005 occurred in solar irradiance. Positive forcings lead to warming of climate and negative forcings lead to a cooling. The thin black line attached to each coloured bar represents the range of uncertainty for the respective value (IPCC 2007).

16

In imposing forcing to the model simulations, total forcing term (Q) in Eq. (3.5) can be expressed as the sum of individual component of forcing as :

$$Q = \sum Q_i \tag{3.11}$$

where, Q_i is the individual component of forcing. i can be volcano eruption, CO_2 emissions, ozone recovery, and so on. For example, greenhouse gases such as CO_2 and CH_4 lead to positive radiative forcing but aerosol and deforestation lead to negative radiative forcing (see Fig. 8).

The first generation Atmospheric General Circulation Models (AGCMs) were created in the 1960s such as the Geophysical Fluid Dynamics Laboratory (GFDL) model (Smagorinsky et al. 1965, Manabe et al. 1965), the University of California Los Angeles (UCLA) model (Mintz 1965), and the National Center for Atmospheric Research (NCAR) model (Kasahara and Washington 1967). The first Ocean General Circulation Models (OGCMs) were developed at GFDL (Bryan 1969; Cox 1970). The coupled Atmosphere-Ocean GCM (AOGCM) representing the nature of the earth was created by Manabe et al. (1975) and Bryan et al. (1975). Based on these fundamental models, many models were developed in 1970-1980s in different institutes over the world. They were shown to have the capability to successfully simulate the major aspects of the general circulations such as the easterly trade winds, mid-latitude jet streams in the atmosphere, the Gulf Stream and other major currents in the ocean (e.g., Washington and Parkinson 2005). The AOGCM is now the standard for long-term climate model simulations (Meehl et al. 2009, Taylor et al. 2012).

17
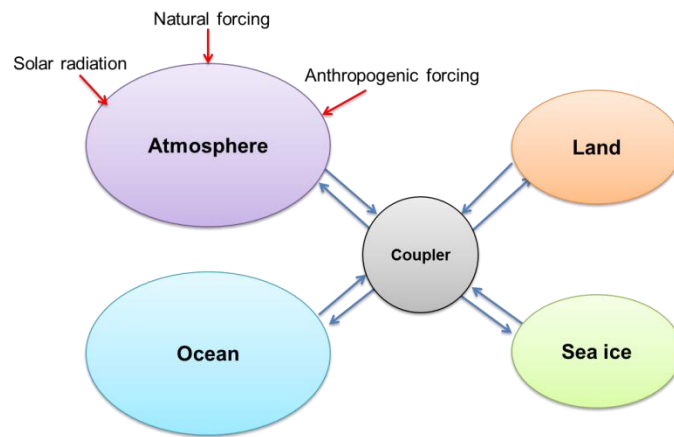
Figure 9: Schematic architecture of the fully coupled model. The colored bubbles represent the components of the climate system, gray circle is the coupler, blue arrows are the flux interactions among them, and red arrows are forcing.

The AGCM is driven by solar radiation and a prescribed SST in the lower boundary condition. The OGCM is driven by the imposed wind stress and heat flux in the upper boundary condition. The recent AOGCM is fully coupled with AGCM, OGCM, land model and sea ice model, and is driven by forcing. The fluxes between the model components such as heat, momentum and water are exchanged using a software package called "Coupler" (see Fig. 9).

3.2   Model errors

Even though the climate models are based on the physical laws, they have model errors by the limited grid representation of the Earth, and the complexity of the individual Earth components (e.g., atmosphere, ocean, land, etc.) and their coupling.

In coarse resolution global models (Fig. 4), the terms representing source, sink and forcing that are not resolved (Q, $F\varphi$ and F_λ in Eqs. (3.1)-(3.3)). They should be evaluated by the resolved large-scale variables using subgrid-scale (SGS) "Parameterization". Comprehensive studies have been done to improve those terms that represent the processes associated with the unresolved SGS, such as radiation, convection and cloud formation, and surface processes (e.g., Arakawa 2004). Different choices of parameterization schemes result in the model biases.

The models have been evolved to incorporate the complexity of the Earth components and physical processes. For example, the Earth system models in CMIP5 include biochemical and interactive carbon cycles. Some models have embedded chemical cycles. The levels of understanding of the processes and their representation by parameterization schemes contribute to the model errors.

The observations also serve as a source of model errors. Some parameters are tuned based on the observations, and the uncertainty in the observational fields propagates into the tuning of parameters. The numbers of degree of freedom in the observations are much more than those of tunable parameters in the models. This limitation results in a good representation of a certain key climate variable and variability, but a bad representation of others.

The models have been improved to reduce errors by finer numerical grids, more complete set of physical processes, and better parameterization schemes. In parallel, the multi-model ensemble simulations provide a better statistical estimate of uncertainty rather than any single model simulations.

19

3.3   Coupled Model Intercomparison Project (CMIP)

The CMIP initiated by WGCM under WCRP (see Fig. 10 for the organizations), have provided climate scientists with a database of the centennial AOGCM simulations since 1995.
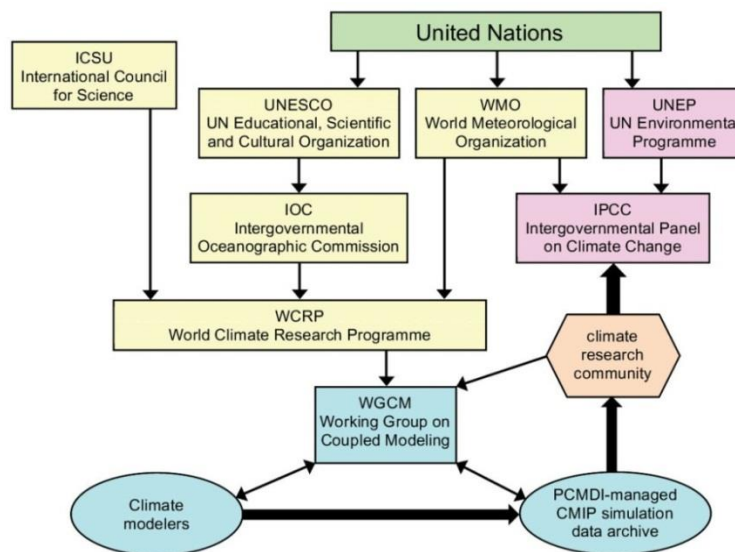
Figure 10: The relationship of CMIP5 to organizations established to coordinate climate research activities internationally and to the IPCC, the modeling centers, and the climate research community (Taylor et al. 2012).

The CMIP is the project that manages the unique data archive, in which more than 20 modeling groups in more than 10 countries participate. The data is collected up to 36 TB for CMIP3 and 1483 TB for CMIP5. Some model groups are still preparing simulations for CMIP5. It is widely used in the climate research. For example, more than 700 and 100 journal articles as of March 2013 were published using CMIP3 and CMIP5 archives, respectively (http://apps.webofknowledge.com). Also, the IPCC established by WMO and UNEP, publishes assessment reports on the current state of science, which are

widely used for policy making over the world. The AR4 was published in 2007 based on the researches using CMIP3 archive, and the AR5 will be published in late 2013 based on CMIP5 archive.
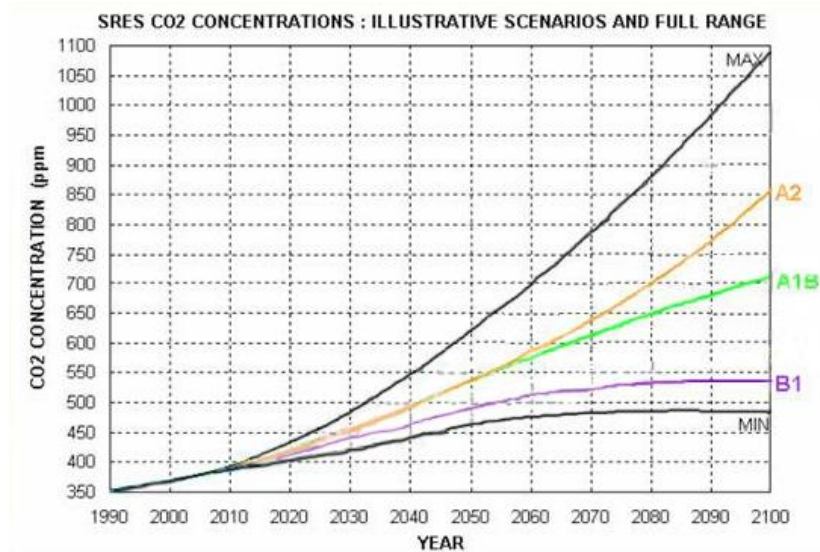
Figure 11: Atmospheric CO_2 Concentrations Projected by the SRES Scenarios. CO2 concentrations reach 850 ppm in the year 2100 under A2 scenario, 720 ppm under A1B and 550 ppm under B1 (NCAR).

CMIP provides model groups with the standard sets of experiments such as centennial timescale integration for past, present and future in both CMIP3 and CMIP5, and the near-term integration (10-30yr) for present in CMIP5. For future projections, the standard forcing is provided based on future scenarios. CMIP3 adopted the "Special Report on Emission Scenarios" (SRES) based on the socio-economic scenarios, which are categorized by the future world of economy, population, technology, environment and governance (Nakicenovic et al. 2000). The time varying CO_2 concentrations for each scenario are shown in Fig.11. Rather than starting with socio-economic scenarios in CMP3, CMIP5 uses "Representative concentration pathways" scenarios (RCP), of which

the level of radiative forcing in 2010 and the shape of pathway are fixed (see Fig. 12; Moss et al. 2010).
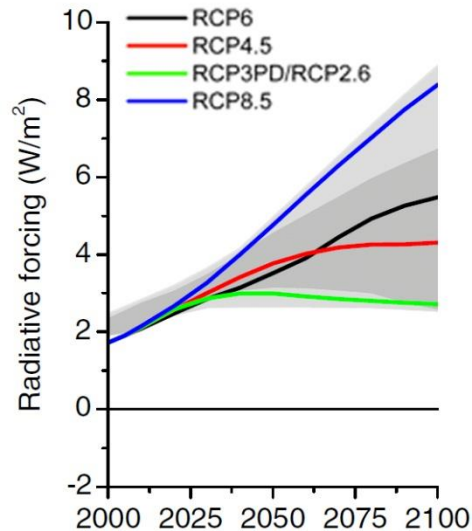
Figure 12: Radiative Forcing of the Representative Concentration Pathways for each scenario. RCP8.5 has rising radiative forcing pathway leading to 8.5 W m^2 in 2100. RCP6 has Stabilization without overshoot pathway to 6 W m^2 at stabilization after 2100. RCP4.5 has stabilization without overshoot pathway to 4.5 W m^2 at stabilization after 2100. RCP2.6 Peak in radiative forcing at ~ 3 W m^2 before 2100 and decline. (Moss et al. 2010).

In this study, the CMIP models summarized in Tables 2 and 3 will be used, and three types of centennial simulations are included: the "Historical" or "Climate of the 20th Century" (20C3M) runs that incorporate the solar/aerosol and GHG forcing for the 20th Century; the "Pre-industrial control" (PICNTRL) runs under a fixed pre-industrial level of GHG concentration, and the 21st century simulations based on the "720 ppm stabilization" (SRES-A1B) scenario for CMIP3. Likewise the "Historical" and "Pre-industrial" runs as straightforward counterparts of CMIP3 and the simulations under RCP8.5 scenario will be included for CMIP5.

Table 2: The CMIP3 models used in Chapter 7.

No.	Model	Institute
1	BCCR-BCM2.0	Bjerknes Centre for Climate Research, Norway
2	CCSM3	National Center for Atmospheric Research, USA
3	CGCM3.1(T47)	Canadian Centre for Climate Modelling and Analysis,
4	CGCM3.1(T63)	Canada
5	CNRM-CM3	Centre National de Recherches Meteorologiques, France
6	CSIRO-MK3.0	CSIRO Atmospheric Research, Australia
7	CSIRO-MK3.5	
8	ECHAM5/ MPI-OM	Max Planck Institute for Meteorology, Germany
9	FGOALS-g1.0	Institute of Atmospheric Physics, China
10	GFDL-CM2.0	Geophysical Fluid Dynamics Laboratory, USA
11	GFDL-CM2.1	
12	GISS-AOM	Goddard Institute for Space Studies, USA
13	GISS-EH	
14	GISS-ER	
15	INGV-SXG	INGV, National Institute of Geophysics and Volcanology, Italy
16	INM-CM3.0	Institute for Numerical Mathematics, Russia
17	IPSL-CM4	Institut Pierre Simon Laplace, France
18	MIROC3.2(hires)	Center for Climate System Research/ National Institute for Environmental Studies/ Frontier Research Center for Global
19	MIROC3.2(medres)	Change, Japan
20	MRI-CGCM2.3.2	Meteorological Research Institute, Japan
21	PCM	National Center for Atmospheric Research, USA
22	UKMO-HadCM3	Hadley Centre for Climate Prediction, Met Office, UK
23	UKMO-HadGEM1	

Table 3: The CMIP5 models included in Chapter 7.

No.	Model	Institute
1	BCC-CSM1.1	Beijing Climate Center(BCC),China Meteorological Administration, China
2	BNU-ESM	College of Global Change and Earth System Science, Beijing Normal University, China
3	CanESM2	Canadian Centre for Climate Modelling and Analysis, Canada
4	CCSM4	National Center for Atmospheric Research, USA
5	CNRM-CM5	Centre National de Recherches Meteorologiques, France Centre Europeen de Recherches et de Formation Avancee en Calcul Scientifique, France
6	CSIRO-Mk3.6	Australian Commonwealth Scientific and Industrial Research Organization Marine and Atmospheric Research in collaboration with the Queensland Climate Change Centre of Excellence , Australia
7	FGOALS-s2	Institute of Atmospheric Physics, China
8	FIO-ESM	The First Institute of Oceanography, China
9	GFDL-CM3	Geophysical Fluid Dynamics Laboratory, USA
10	GFDL-ESM2G	
11	GFDL-ESM2M	
12	GISS-E2-H	Goddard Institute for Space Studies, USA
13	GISS-E2-R	
14	HadCM3	Met Office Hadley Centre, UK
15	HadGEM2-AO	National Institute of Meteorological Research, South Korea
16	HadGEM2-CC	Met Office Hadley Centre, UK
17	HadGEM2-ES	
18	INM-CM4	Institute for Numerical Mathematics, Russia
19	IPSL-CM5A-LR	Institut Pierre Simon Laplace, France
20	IPSL-CM5A-MR	
21	MIROC-ESM	Japan Agency for Marine-Earth Science and Technology/
22	MIROC-ESM-CHEM	Atmosphere and Ocean Research Institute/ National Institute for
23	MIROC5	Environmental Studies, Japan
24	MPI-ESM-LR	Max Planck Institute for Meteorology, Germany
25	MPI-ESM-MR	
26	MPI-ESM-P	
27	MRI-CGCM3	Meteorological Research Institute, Japan
28	NorESM1-M	Norwegian Climate Centre, Norway

3.4   NCAR Community Atmosphere Model (CAM)

The majority of this study will use CMIP archives and the reanalysis datasets. The AGCM simulations will be used only in Chapter 8 to understand the dynamic response of the atmosphere to the lower boundary condition.

The Community Atmosphere Model (CAM) 3.1 used in Chapter 8 is the fifth generation of the National Center for Atmospheric Research (NCAR) AGCM, and also serves as the atmospheric component of the coupled NCAR Community Climate System Mode (CCSM) models.
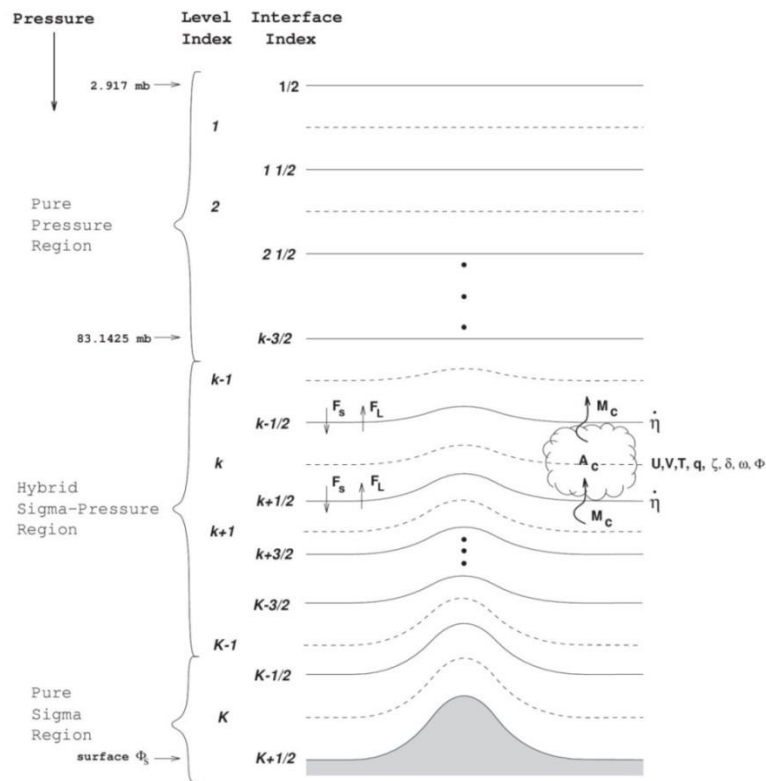
Figure 13: Terrain-following hybrid vertical coordinate of CAM (Collins et al. 2006).

The model consists of the spectral Eulerian dynamical core to solve the differential Eqs. (3.1)-(3.6), and a suite of the physics, which are parameterized on the precipitation processes, clouds and radiation, surface model and turbulent mixing. The dynamical core has switchable spectral resolutions: T31 (48 lat.×96 lon; approximately 3.75° resolution), T42 (64×128; approx. 2.8°), and T85 (128×256; approx. 2°), with 26 vertical levels and a rigid lid at 2.917 hPa. The primitive equations in a terrain-following hybrid vertical coordinate (Fig. 13) equivalent to Eqs. (3.1)-(3.6) are solved using a semi-implicit, leap frog time integration scheme, the spectral transform method is used to treat the dry dynamics (Collins et al. 2006).

To run the model, the basic initial data for atmospheric variables such as pressure and wind should be specified on the Gaussian grid at time t=0. In addition to the initial conditions, a seasonally varying sea surface temperature and sea ice concentration dataset is used to prescribe the time evolution of these surface quantities as a lower boundary conditions. The initial conditions and boundary conditions are provided with the release of the model, and can also be prescribed for the purpose of the simulations by the user.

Chapter 4

4   CLIMATE INDEX

For this study, the dynamic climate variable of zonal-mean zonal wind is mainly

used for validation and intercomparison. The zonal-mean zonal wind is the major feature

of the atmosphere general circulation (Fig. 14). It is useful to understand the global

circulation pattern, the atmosphere-ocean interaction, the impact of the increased

greenhouse gases (GHG) and surface phenomena such as storm track by the strength and

latitudinal location of the large-scale zonal jet even though it is an upper troposphere

phenomena.
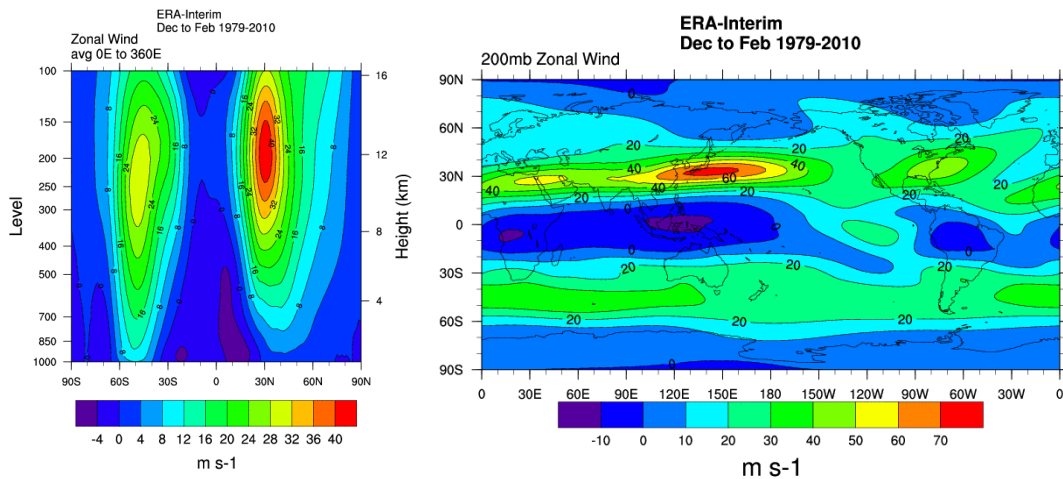
Figure 14: (left) The vertical structure of the observed zonal wind from ERA-Interim in Winter (DJF) over 1979-2010. Jet streams (colored in red and yellow) are located at about 200 hPa and 10-12km height at mid-latitudes. (right) The observed zonal wind at 200 hPa. The strong eastward wind bands (jet streams) at mid-latitudes are observed in both Hemispheres. (http://www.esrl.noaa.gov/psd/)

4.1   Atmospheric Angular Momentum (AAM)

The globally integrated Atmospheric Angular Momentum (AAM) is the climate

index which is known to usefully represent the variability of tropospheric zonal flow. It

tends to increase as the zonal jet moves equatorward or is enhanced under increased GHG forcing, and to decrease as the jet shifts poleward or is weakened under decreased radiative forcing (see Fig. 15).
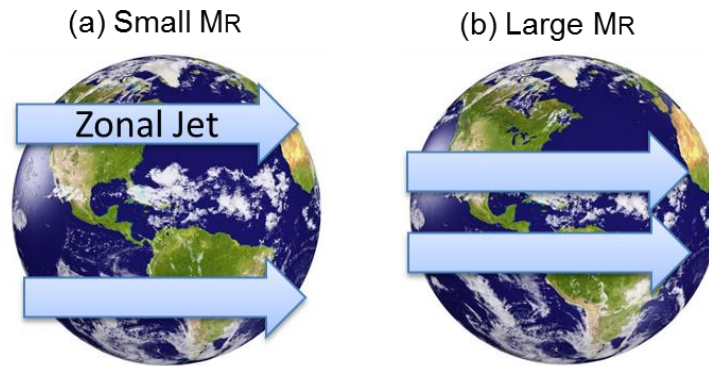
Figure 15: Relation between AAM and zonal wind. (a) Small M_R (wind component of AAM) for the higher latitudinal location of zonal wind. (b) Larger M_R for the lower latitudinal location of zonal wind.

The index is widely used for the large-scale atmospheric circulation that reflects the variation of atmospheric zonal wind associated with major climatic phenomena ranging from Madden-Julian Oscillation (e.g., Feldstein and Lee 1995, Weickmann et al. 1997), El Niño (e.g., Black et al. 1996, Huang et al. 2003), Quasi-biennial Oscillation (QBO; Chao 1989, Abarca del Rio et al. 2000), global warming (Abarca del Rio 1999, Huang et al. 2001, de Viron et al. 2002, Räisänen 2003), to decadal-to-interdecadal variability (Paek and Huang 2012) .

The global AAM is the sum of the relative angular momentum (M_R), which reflects the strength and distribution of zonal wind, and the mass or "omega" angular momentum (M_Ω), which depends on atmospheric mass distribution. The former

28

dominates the variability of the total AAM. The two components of the total AAM are evaluated as (Peixoto and Oort 1992):

$$M_R = \frac{a^3}{g} \int_{10hPa}^{1000hPa} \int_0^{\pi/2} \int_{-\pi/2}^{\pi/2} u \cos^2\theta \, d\theta d\lambda dp \,, \tag{4.1}$$

$$M_\Omega = \frac{a^4\Omega}{g} \int_0^{\pi/2} \int_{-\pi/2}^{\pi/2} p_s \cos^3\theta \, d\theta d\lambda \,, \tag{4.2}$$

where, $a = 6.371 \times 10^6$ m is the mean radius of the Earth, Ω is the rotation rate of the Earth, g=9.81 m s^{-2} is gravitational acceleration, u is the 3-D zonal wind as a function of latitude θ, longitude λ and pressure p, and p_s is the surface pressure as a function of latitude θ and longitude λ. We will denote 1×10^{25} kg m^2 s^{-1} as 1 Angular Momentum Unit (AMU) for AMM.

While different reanalysis and CMIP datasets have different vertical resolutions, for a fair comparison we keep the upper bound of the integration in Eq. (4.1) at 10 hPa for all of them. It is found that it does not affect the conclusion.

Since the anomaly of M_R is generally dominated by the variability of upper tropospheric zonal wind, another index is also used (Huang and Sardeshmukh 2000),

$$M_{200} = a^2 \int_0^{2\pi} \int_{-\pi/2}^{\pi/2} u_{200} \cos^2\theta \, d\theta d\lambda \,, \tag{4.3}$$

where, u_{200} is the zonal wind at 200 hPa, to quantify the contribution of the upper level zonal wind to M_R.

A few previous studies have analyzed the budget of AAM for a small subset of the reanalysis datasets considered in this study. For example, a detailed budget of AAM for NCEP R-1 was calculated by Huang et al. (1999) and a comparison of the AAM and torques in NCEP R-1 and ERA was carried out by Egger et al. (2003).

4.2   Length-of-day (LOD)

Given the near conservation of the total (atmosphere plus Earth) angular momentum of the earth system on interannual timescale (e.g., Peixoto and Oort 1992, Egger et al. 2007), an increase in the total AAM should accompany an increase in LOD (i.e., a decrease in the rotation rate of the Earth).

The anomaly of LOD will be approximately linearly proportional to the anomaly of AAM. For example, previous studies (Rosen and Salstein 1983, Peixoto and Oort 1992) have adopted the approximation,

$$\Delta LOD \approx 0.168 \Delta AAM , \tag{4.4}$$

where, Δ denotes the anomaly, ΔLOD is in ms, and ΔAAM ($= \Delta M_R + \Delta M_\Omega$) is in AMU.
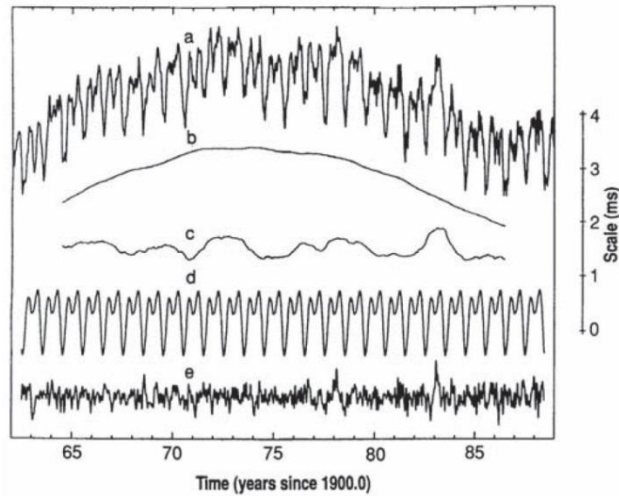
Figure 16: Timeseries of irregular fluctuation in the length of the day (LOD) from 1963 to 1992 (curve a) and its decadal, interannual, seasonal, intraseasonal, components (curves b, c, d, and e, respectively). The decadal (curve b) component largely reflects angular momentum exchange between solid Earth and the underlying liquid metallic outer core produced by torques actinf at the core-mantle boundary. The components (curves c, d and e) largely reflect angular momentum exchange between the atmosphere and the solid Earth produced by toques acting directly on the solid Earth over continental regions of the Earth's surface and indirectly over oceanic regions (Hide and Dickey 1991).

Using this relation, an independent LOD dataset from geodetic measurements is useful to validate AAM from the atmospheric observations on the interannual timescale but the relation holds less accurately at longer (e.g., interdecadal) timescales; Processes related to core-mantle coupling in Earth's interior occur at those timescales (e.g., Lambeck 1980, Hide and Dickey 1991) that can cause variations in LOD without a change in AAM.

4.3   Nino 3.4 Index

El Nino is well-recognized interannual variablility, and defined as the events at which 5-month running means of SST anomalies in the Niño 3.4 region bounded by 120°W-170°W and 5°S-5°N exceed 0.4°C for 6 months or more (Trenberth 1997; Fig. 17).

The interannual variability of ΔAAM is known to be closely related to El Nino (e.g., Black et al. 1996, Huang et al. 2003). Previous studies have explored the correlation between ΔAAM and the commonly used Nino3.4 index (without 5-month running mean). The relative AAM increases during El Nino because of the enhancement of subtropical jets as a canonical response to an increase in the equatorial Pacific SST (Black et al. 1996). Since this connection can sometimes be disrupted by other processes unrelated to El Nino (e.g., Huang et al. 2003), the correlation between ΔAAM and Nino3.4 is generally not as high as that between ΔAAM and ΔLOD. While one cannot use Nino3.4 or similar SST indices to rigorously validate the ΔAAM in reanalysis, a correlation analysis for Nino3.4 and ΔAAM remains useful since the spread of the correlation

31

coefficient among different reanalysis datasets will provide a measure of the uncertainty

in reanalysis.

(a)

(b)
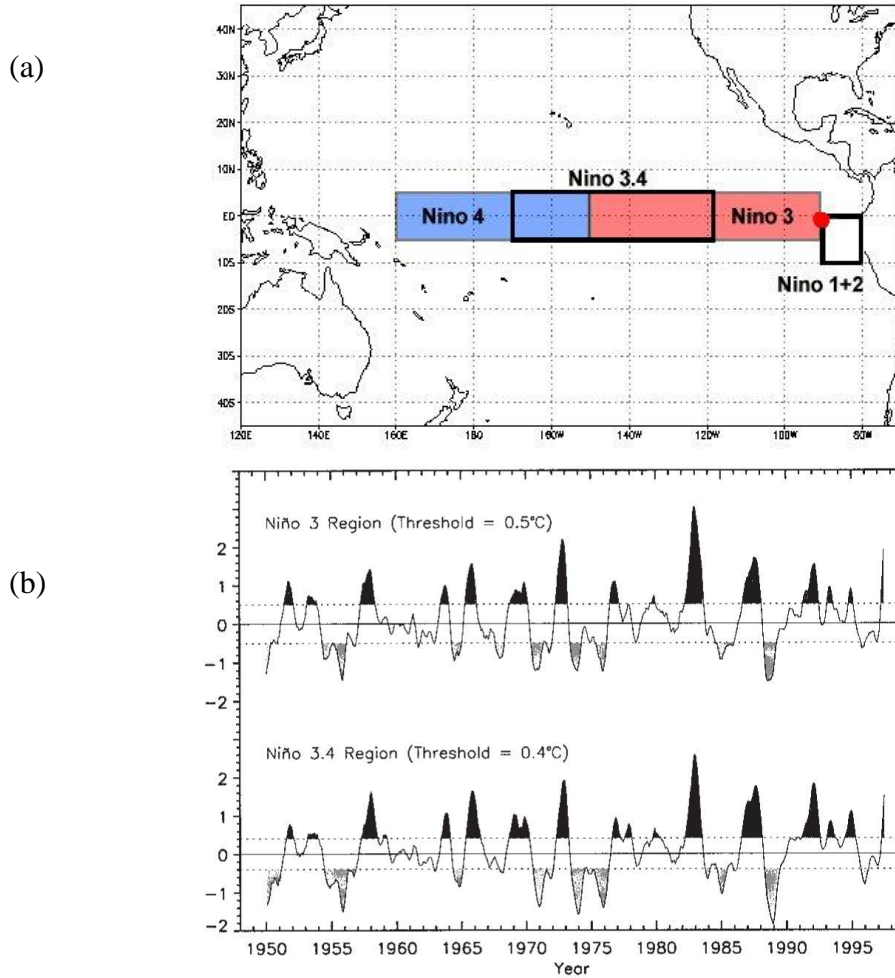
Figure 17: (a) Boxes for Nino regions. (b) Time series plots of the Niño 3 (upper) and Niño 3.4 SST indices as 5-month running means using data from NOAA and relative to a base period climatology from 1950 to 1979. Values exceeding thresholds of ±0.5℃ for Niño 3 and ±0.4℃ for Niño 3.4 are stippled to indicate ENSO events (Trenberth 1997).

Chapter 5

5   OBSERVATIONS: INTERANNUAL VARIABILITY AND VALIDATION
     WITH LOD

The reanalysis datasets created in the past decade have greatly advanced climate
and weather applications. They were produced based on the assimilation of different
sources of observations, using numerical models with a wide range of spatial resolution
and different levels of sophistication for atmosphere-ocean coupling (see section 2.1).
Despite their importance in research and application, a systematic comparison of the
climate variability and trend in the major reanalysis datasets is still lacking.

An intercomparison of the major reanalysis datasets is beneficial in two respects.
First, the difference among the datasets can be used to measure the uncertainty in the
climate variables in reanalysis. Secondly, by cross validating the reanalysis with other
independent observations, one might be able to determine the relative quality of the
reanalysis datasets for a specific variable. This will help guide practitioners to choose a
suitable dataset for a specific application.

Given this background, this study will cross validate the total AAM (relative
AAM + mass AAM) in reanalysis with the length-of-day (LOD) data obtained from
independent geodetic measurements. Given the near conservation of the total
(atmosphere plus Earth) angular momentum of the earth system on interannual time scale,
an increase in the total AAM should accompany an increase in LOD (see section 4.2).

Given the well-known influence of El Nino on atmospheric angular momentum,
the intercomparison for AAM will also be extended to the correlation between the
anomalies of AAM and tropical Pacific SST. This will complement the analysis of the

AAM-LOD connection because the correlation of AAM and SST reflects the upward influence of SST on atmospheric circulation which is largely confined to within the troposphere, whereas the correlation of AAM and LOD can be further affected by the representation of the variability of stratospheric zonal wind in a reanalysis dataset. We will complete the intercomparison by synthesizing the results of the correlation analysis for AAM-AAM, AAM-LOD, and AAM-SST with the AAM computed from eight reanalysis datasets.

5.1   Datasets and analysis method

The monthly mean variables from the eight reanalysis datasets summarized in Table 1 are used for the intercomparion. While there is a significant overlap of the observational data used in creating those datasets, differences among them can arise because they were produced by different global models that employed different techniques for data assimilation. As two notable examples, while most of the datasets were produced with an atmosphere-only model, the CFSR datasets were based on a coupled atmosphere-ocean model. The 20CR dataset is unique in that it assimilates only the surface observations in order to maintain long-term homogeneity of the observations over a century, in contrast to all other datasets that assimilate the full 3-D fields.

For our analysis, the zonal wind and surface pressure fields are used to calculate AAM, which is evaluated as Eqs. (4.1) and (4.2). The length-of-day data used in this study is adapted from COMB2007. From the original daily data of LOD for 1962-2008, we construct the monthly mean LOD and retain the post-1979 portion of the time series

34

for the cross validation with the AAM data. For a visual comparison of the ΔLOD and ΔAAM time series, Eq. (4.3) is used to convert ΔLOD to an equivalent ΔAAM.

Our intercomparison will use the 1979-2007 (1979-2001 for ERA-40) portion of the reanalysis and LOD data. To focus on the interannual variability of ΔLOD and ΔAAM, we first construct the anomaly of LOD and AAM by removing the mean annual cycle (defined as the sum of the annual, semiannual, and triannual harmonics) from the time series of the monthly mean data. Next, we remove the slow components (with their periods longer than the interannual time scale) defined as the long-term mean plus the first seven harmonics for the 29-year record except for the slightly shorter ERA-40 dataset for which we remove the first five harmonics for the 23-year record. A Hann window is used for tapering in conjunction with the Fourier analysis. To prevent the end-point effect from contaminating the correlation analysis, we remove the first and last 1.5 years of the time series that are not properly filtered. The detailed procedure is similar to that used by Huang et al. (2003). Hereafter, we will use ΔLOD and ΔAAM to denote anomalies of LOD and AAM after they are processed by the procedure described above.

5.2   Atmospheric angular momentum and length-of-day

The ΔAAM from the eight reanalysis datasets are shown in Figs. 18a-18h. The ΔLOD, converted to an equivalent ΔAAM by Eq. (4.3), is superimposed to all panels in Fig. 18. One can immediately see a qualitative agreement among the ΔLOD and different ΔAAM time series for the reanalysis datasets. However, differences in detail do exist. To quantify them, Table 4 summarizes the correlation of two ΔAAM time series or that of ΔLOD and ΔAAM for all possible pairings of the reanalysis and LOD datasets.
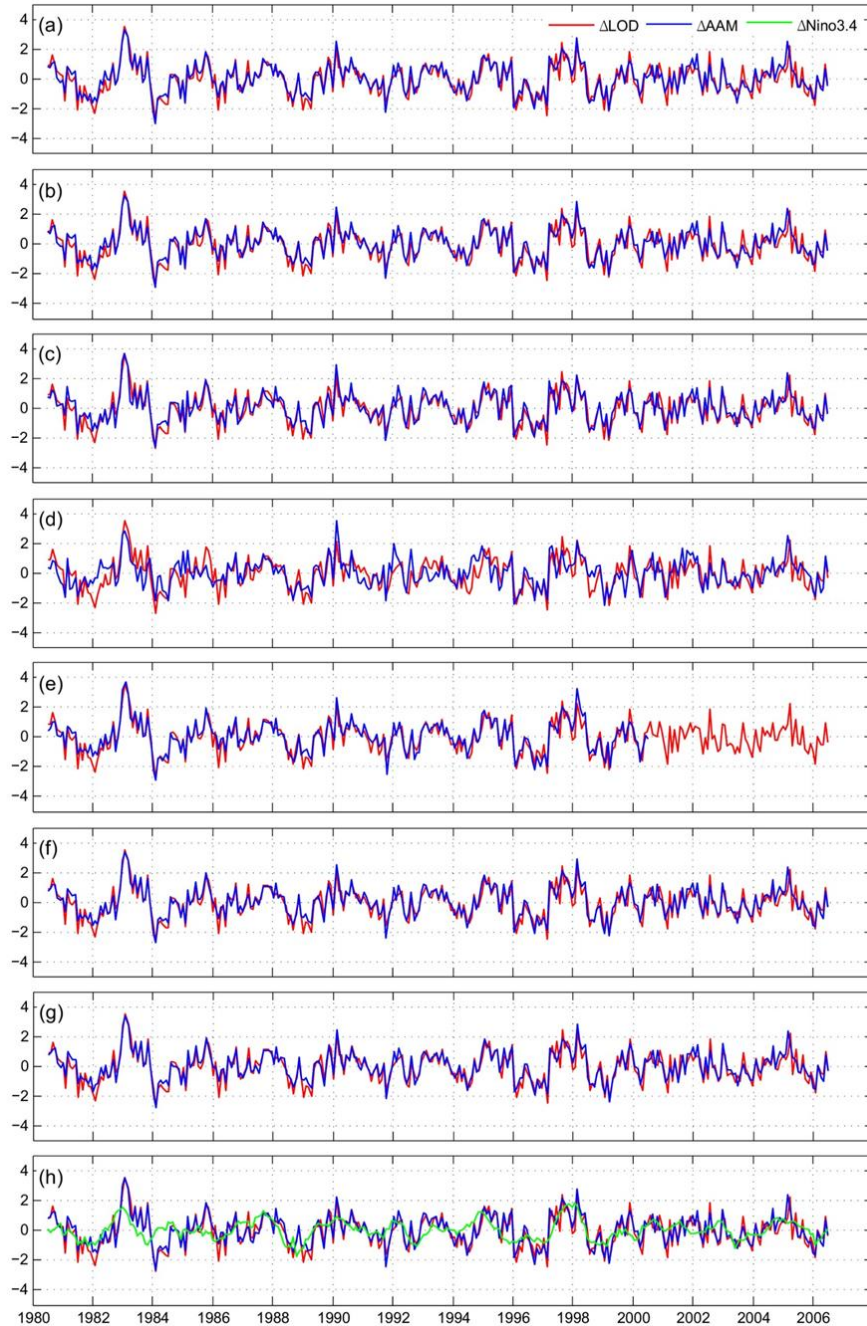
Figure 18: The time series of ΔLOD (red curve, converted to an equivalent ΔAAM using Eq. (4.3)) and ΔAAM (blue curve) from different reanalysis datasets: (a) NCEP R-1, (b) NCEP R-2, (c) CFSR, (d) 20CR, (e) ERA-40, (f) ERA-Interim, (g) JRA-25, and (h) MERRA. The time series of ΔNino3.4 from HadISST is imposed as the green curve in panel (h). The units for ΔAAM and ΔNino3.4 are 10^{25} kg m^2 s^{-1} and °C, respectively. The time series for ΔAAM in panel (e) is slightly shorter due to the shorter record of the ERA-40 dataset.

36

In general, ΔLOD is highly correlated with ΔAAM with the correlation coefficient ranging from 0.717 for 20CR to 0.905 for NCEP R-1. All those numbers are at 99% significance level with the given degrees of freedom (~78) of the individual time series (e.g., von Storch and Zwiers 2002). Of course, this high level of correlation is well-known (e.g., Peixoto and Oort 1992) and it attests to the strong physical constraint of the conservation of angular momentum of the Earth-atmosphere system. For the intercomparison among the reanalyses, the difference in the correlation of (ΔLOD, ΔAAM) between any two reanalysis datasets is not statistically significant at 95% level, except when the ΔAAM is computed from 20CR. In that case, the correlation of (ΔLOD, ΔAAM) for 20CR is lower than that for any other reanalysis dataset at 95% significance level.

The correlation in Table 4 does not reflect the amplitude of the individual time series. To supplement it, the standard deviation (square root of variance) is calculated for the AAM time series in Fig. 18. We found the values to be (0.973, 0.961, 0.969, 0.926, 0.918, 0.992, 0.963, 0.980) in AMU for the ΔAAM of (NCEP R-1, NCEP R-2, CFSR, 20CR, ERA-40, ERA-Interim, JRA-25, MERRA). The standard deviation of the equivalent ΔAAM from the observed ΔLOD is 1.022 AMU. This suggests a close agreement in the amplitude of the interannual variability among the reanalysis datasets.

The correlation of (ΔAAM$_1$, ΔAAM$_2$) where ΔAAM$_1$ and ΔAAM$_2$ are the anomalies of angular momentum from two reanalysis datasets is also shown in Table 4. All of the pairings in Table 4 lead to a correlation exceeding 0.95, except when one of the ΔAAMs comes from 20CR then the correlation falls below 0.8. This behavior is consistent with the correlation of (ΔLOD, ΔAAM) listed in Table 4.

Table 4: The correlation coefficients for different pairs of (ΔAAM, ΔAAM) or (ΔAAM, ΔLOD) where ΔAAM is calculated from reanalysis and ΔLOD is derived from the COMB2007 dataset. The correlation is performed for 1979-2008 (1979-2001 if the ΔAAM is from ERA-40; the related numbers are in parenthesis), excluding the endpoints in the first and last 18 months that are affected by tapering. The numbers in the top and left margins are shorthand for (1) ΔLOD, (2) NCEP R-1, (3) NCEP R-2, (4) CFSR, (5) 20CR, (6) ERA-40, (7) ERA-Interim, (8) JRA-25, and (9) MERRA, where (2)-(9) are for ΔAAM.

	(1)	(2)	(3)	(4)	(5)	(6)	(7)	(8)	(9)
(1)	1	0.905	0.900	0.875	0.718	(0.907)	0.899	0.903	0.900
(2)		1	0.996	0.956	0.793	(0.972)	0.982	0.983	0.978
(3)			1	0.958	0.794	(0.972)	0.982	0.984	0.978
(4)				1	0.779	(0.946)	0.966	0.963	0.971
(5)					1	(0.771)	0.781	0.783	0.775
(6)						1	(0.983)	(0.978)	(0.974)
(7)							1	0.993	0.990
(8)								1	0.989
(9)									1

To visualize the difference between 20CR and other datasets, Fig 19a shows the difference between ΔLOD, converted to an equivalent ΔAAM by Eq. (4.3), and the ΔAAM of the eight reanalysis datasets. (Since the choice of the constant, 0.168, in Eq. (4.3) is somewhat *ad hoc*, the figure here only serves as a way to visualize but not rigorously quantify the absolute difference between ΔLOD and ΔAAM). Figure 19b shows the difference between the ΔAAM of NCEP R-1 (which has the highest correlation with ΔLOD) and the ΔAAM of the other seven reanalysis datasets. These figures show that 20CR clearly stands out. The blue curves for 20CR in Figs. 19a and 19b exhibit organized low-frequency variation which we should explore further.
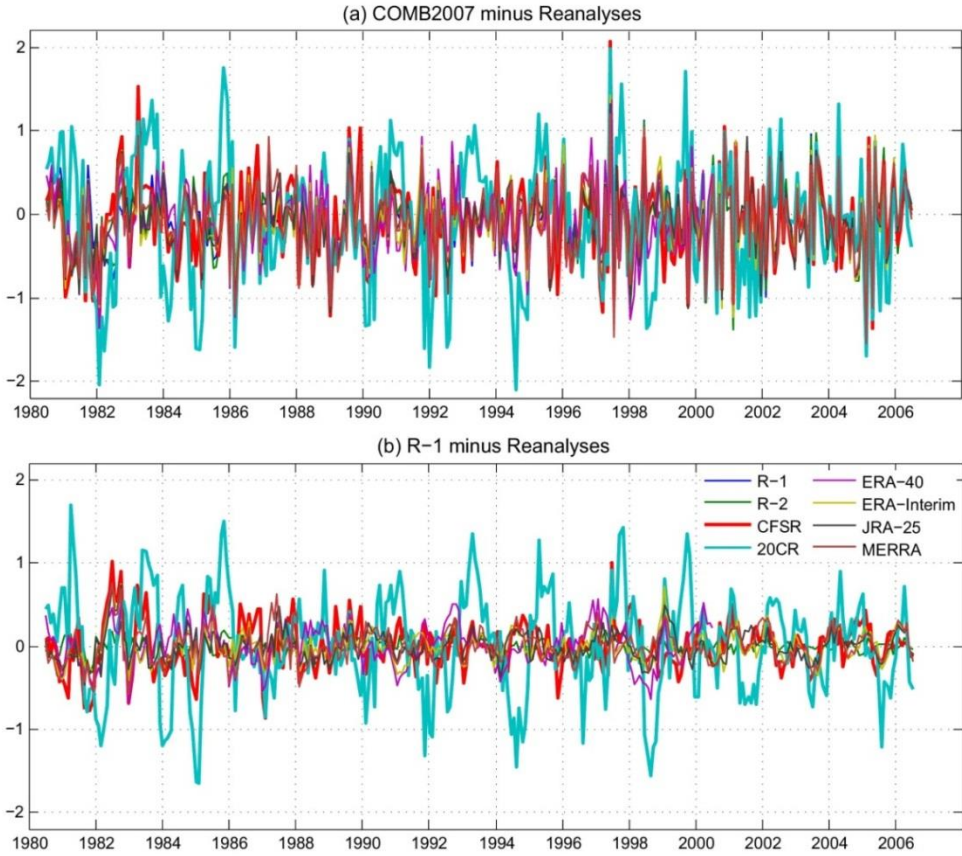
Figure 19: (a) The time series of the difference between ΔLOD (converted to an equivalent ΔAAM using Eq. (4.3)) and the ΔAAM from the eight reanalysis datasets. (b) The time series of the difference between the ΔAAM of NCEP R-1 and the ΔAAM from the other seven reanalysis datasets. The unit for ΔAAM is AMU and the reanalysis datasets are labeled in panel (b).

5.3   The 20CR data and impact of stratospheric zonal wind on AAM

Since the 20CR dataset assimilated only surface observations, it is intuitive to guess that the relatively low correlation between the ΔAAM of 20CR and ΔLOD is related to the difference in the structure of zonal wind at the upper troposphere and stratosphere between 20CR and other reanalysis datasets (This mainly affects ΔM_R, but for the comparison to we will keep the total ΔAAM for the discussion). Previously, Paek

39

and Huang (2012) showed that the Quasi-biennial oscillation (QBO) is absent in 20CR, which contributes to a negative bias in the long-term climatology of relative AAM in that dataset. To quickly illustrate that the absence of QBO is a unique feature of 20CR, Fig. 20a shows the time series of the "stratospheric component" of ΔM_R, (hereafter denoted as $\Delta M_{R,STRAT}$), for which the M_R is calculated by Eq. (4.1) but with the vertical integral carried out from 100 hPa to 10 hPa only. The time series of $\Delta M_{R,STRAT}$ for 20CR stands out in that it does not have a clearly identifiable QBO. Since QBO is known to contribute to the interannual variability of LOD (Chao 1989, Abarca del Rio et al. 2000), we expect the absence of the former to have some impact on the correlation between ΔAAM and ΔLOD in 20CR.
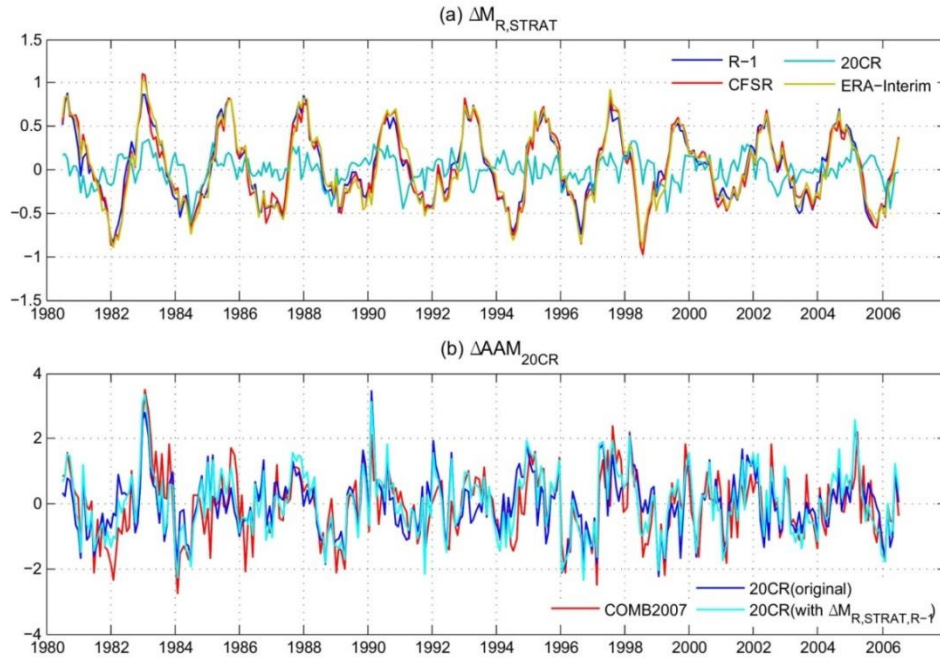
Figure 20: (a) The time series of $\Delta M_{R,STRAT}$ for four selected reanalysis datasets including 20CR. (b) The original (dark blue) and the modified ΔAAM (light blue) for 20CR. The modified ΔAAM is calculated by replacing the zonal wind in the stratosphere by that from NCEP R-1. See text for detail. The time series of ΔLOD (converted to an equivalent ΔAAM using Eq. (4.3)) is also shown as the red curve. The unit for ΔAAM is AMU.

40

To quantify it, we repeat the calculation of the ΔAAM for 20CR by artificially replacing its $\Delta M_{R,STRAT}$ component by that calculated from NCEP R-1. The time series of the original and modified ΔAAM for 20CR, and ΔLOD, are shown in Fig. 20b. The correlation between the modified ΔAAM of 20CR and ΔLOD is 0.823, compared with 0.718 using the original ΔAAM of 20CR. The correlation is further increased to 0.842, 0.857, and 0.868 if the replaced $\Delta M_{R,STRAT}$ component is defined as the integral from 150-10, 200-10 and 250-10 hPa, respectively. These results clearly indicate that the bias in the AAM in 20CR is related to the inaccurate zonal wind in the stratosphere.

5.4   Relation between AAM and Tropical SST

Given our suggestion in Sec 5.3 that the relatively low correlation between ΔAAM and ΔLOD in 20CR comes from the bias in tropical stratospheric zonal wind, it will also be interesting to test whether the correlation between Nino3.4 and ΔAAM for 20CR is closer to that for other reanalysis datasets since the connection between El Nino and AAM is mostly regulated by processes within the troposphere.

For the analysis of the relation between Nino3.4 index and ΔAAM, we first use the monthly mean SST from the HadISST dataset to construct the Nino3.4 index. The time series of the Nino3.4 index, similarly processed as the AAM data, is superimposed to the bottom panel of Fig. 18. (We will hereafter denote the processed Nino3.4 index as ΔNino3.4. The "Δ" indicates that it has been filtered in the same manner as ΔAAM following the procedure described in Sec 5.3.). It shows a very good correspondence between an El Nino (positive ΔNino3.4) event and a positive ΔAAM. The ratio of ΔAAM/ΔNino3.4 ≈ 1 AMU °C^{-1} is consistent with Huang et al. (2003, 2004). The time

series of ΔNino3.4 are also constructed from the Kaplan SST and ERSST datasets. They are not shown as they agree very closely with HadISST for the post-1979 period. The correlation coefficients of ΔNino3.4 and ΔAAM (or ΔLOD) for all possible pairing from the three SST and eight reanalysis (plus one LOD) datasets are summarized in Table 5. Notably, the correlation between ΔNino3.4 and ΔAAM for 20CR is comparable to those for the other reanalysis datasets. In fact, ΔNino3.4 has the lowest correlation with the ΔAAM of not 20CR, but CFSR reanalysis. It may be worth noting that, unlike the majority of the reanalysis datasets, CFSR used a coupled model for data assimilation. Nevertheless, the difference in the correlation of (ΔNino3.4, ΔAAM) between any two reanalysis datasets is not statistically significant at 95% level.

Table 5: The correlation for different pairs of (ΔAAM, ΔNino3.4) or (ΔLOD, ΔNino3.4), and (ΔNino3.4, ΔNino3.4) where ΔNino3.4 is constructed from the HadISST, Kaplan, and ERSST datasets and ΔAAM from eight reanalysis datasets. The numbers in the first column are shorthand for (1) ΔLOD, (2) NCEP R-1, (3) NCEP R-2, (4) CFSR, (5) 20CR, (6) ERA-40, (7) ERA-Interim, (8) JRA-25, and (9) MERRA, where (2)-(9) are for ΔAAM.

	HadISST	Kaplan SST	ERSST
(1)	0.473	0.499	0.457
(2)	0.511	0.527	0.484
(3)	0.522	0.538	0.497
(4)	0.434	0.444	0.406
(5)	0.472	0.497	0.469
(6)	(0.535)	(0.559)	(0.515)
(7)	0.495	0.514	0.475
(8)	0.472	0.494	0.455
(9)	0.489	0.511	0.474
HadISST	1	0.971	0.966
Kaplan SST		1	0.981
ERSST			1

The correlation of (ΔNino3.4, ΔAAM) in Table 5 is not sensitive to the choice of the SST dataset. This simply reflects the close agreement in the interannual variability of tropical Pacific SST among the three SST datasets in the modern (post-1979) era. Given such, the difference in the SST datasets used for data assimilation is likely a minor factor in producing the difference in ΔAAM among the reanalysis datasets.

Since the correlation between ΔNino3.4 and ΔAAM reflects the upward influence of tropical SST on global zonal wind, the fact that 20CR is indistinguishable from other reanalysis datasets in Table 5 indicates that this upward influence is well captured by the data assimilation system for 20CR which incorporated only the surface observations. Indeed, the existence of a strong vertical coupling between the surface boundary condition (or near-surface circulation) and upper-air circulation in the observation is crucial for the success of 20CR. The results from Sec 5.3 indicate that this vertical coupling does not penetrate into the stratosphere as far as interannual variability is concerned. Nevertheless, concerning the variability within the troposphere, 20CR appears to be as good as any other reanalysis datasets.

5.5   Conclusion

This study compared the interannual variability of atmospheric angular momentum calculated from eight reanalysis datasets and further cross validated them with the length-of-day data for the post-1979 era. The intercomparison for angular momentum revealed a close agreement among almost all reanalysis datasets, with the correlation of the AAM anomalies of any two datasets exceeding 0.95 for the post-1979 era. The only exception is the correlation between 20CR and any of the remaining seven

43

datasets, which falls below 0.8. The cross validation with the independent LOD data also showed a similar behavior: The correlations of the LOD anomaly and the AAM anomaly for the seven (excluding 20CR) reanalysis datasets consistently fall within a narrow range of 0.87-0.91, in contrast to a correlation of less than 0.72 between the LOD and the AAM of 20CR. The reduced correlation associated with the 20CR data is mainly due to the bias in the stratospheric (and part of upper tropospheric) zonal wind in that dataset. If the upper-level zonal wind in 20CR is artificially replaced by its counterpart from a different reanalysis dataset, a higher value of the correlation is restored. This also corroborates our previous finding (Paek and Huang 2012) of the absence of coherent low-frequency variability, notably the QBO, in the stratospheric zonal wind in 20CR.

Interestingly, for the correlation between the Nino3.4 index of tropical Pacific SST and the AAM anomaly, 20CR does not have a noticeably lower value compared to other reanalysis datasets. This indicates that the upward influence of SST on the tropospheric circulation (or the vertical coupling between the near-surface and tropospheric circulation) is well captured by the data assimilation system of 20CR, which only explicitly incorporated the surface observations. At the same time, our results of the reduced correlation of the AAM of 20CR and LOD clearly indicate that this upward influence or vertical coupling that is crucial for the success of 20CR does not extend to the stratosphere. Other than the case with 20CR, this study demonstrates the close agreement in the interannual variability of zonal wind (using AAM as an index) among the reanalysis datasets.

Chapter 6

6 OBSERVATIONS : DECADAL-TO-INTERDECADAL VARIABILITY AND TREND

The reanalysis dataset was created using a single numerical model, eliminating temporal discontinuities in the routine daily archive of global analysis due to upgrades of weather forecast models. Nevertheless, the known temporal inhomogeneities in the quality and quantity of observations still raise concerns about the feasibility of using reanalysis to determine climate variability and trend on interdecadal and longer time scales (Thorne and Vose 2010, 2011, Dee et al. 2011). Assimilating only surface observations (Whitaker et al. 2004), the recently released 20CR extended reanalysis back to 1871. Because it is based on a temporally more homogeneous subset of observations, the prospect of using 20CR to extract interdecadal and long-term trend has been suggested and debated elsewhere (e.g., Thorne and Vose 2010, 2011, Dee et al. 2011). To contribute to this line of research, this study will compare the decadal-to-interdecadal variability and trend in 20CR with their counterparts in other reanalysis datasets that assimilated 3-D observations for the second half of the 20th century. The outcome will be used to determine the reliability of the interdecadal variability and trend in 20CR in the pre-1950 era.

For our purpose, M_R is chosen as the key index for the intercomparison, and a comparison in the variability of M_R with other reanalysis datasets forms a stringent test for 20CR. As a further motivation, previous studies have suggested the possibility of interdecadal climate regime shifts, based mostly on a unique event in 1976/77 (e.g., Trenberth 1990, Miller et al. 1994; Huang et al. 2005, Meehl et al. 2009), which is known

45

to be associated with a large upward shift in M_R (Huang et al. 2001, 2003) and a shift in surface torques (Marcus et al. 2011). If the 20CR data also exhibits this large shift in M_R in 1976/77, one may use such a shift as an indicator to search for other climate shift events in the pre-1950 era using that dataset.

6.1   Datasets and analysis method

The reanalysis datasets used to cross validate 20CR are NCEP R-1, NCEP R-2, ERA-40, ERA-Interim, ERA-Interim, CFSR, MERRA and JRA25, as summarized in Table 1.

The global relative angular momentum is evaluated as Eq. (4.1), along with another index of M_{200} as Eq. (4.3). To focus on low-frequency variability, we first suppressed the high-frequency components and seasonal cycle by applying a 1-year low-pass filter to the time series of M_R or M_{200}. Hereafter, the symbol M_R or M_{200} denotes this low-pass filtered quantity. The anomaly of angular momentum, denoted as ΔM_R and ΔM_{200}, is defined as the departure from the long term mean. To further focus on decadal and longer-term variability, a 5-year running mean is applied to the time series of ΔM_R and ΔM_{200}. To deduce the trend in ΔM_R or ΔM_{200}, the 5-year running averaged time series is least-square fitted with a 2nd degree polynomial in time. Then, we may detrend the time series by subtracting this 2nd degree polynomial from ΔM_R or ΔM_{200}. To test the robustness of our conclusion, an additional calculation based on linear instead of quadratic fit will also be performed.

6.2   Decadal-to-interdecadal variability

The 5-year running means of ΔM_R and ΔM_{200} (with the long-term mean removed but without further detrending) for the eight reanalysis datasets are shown in Figs. 21a and 21b.
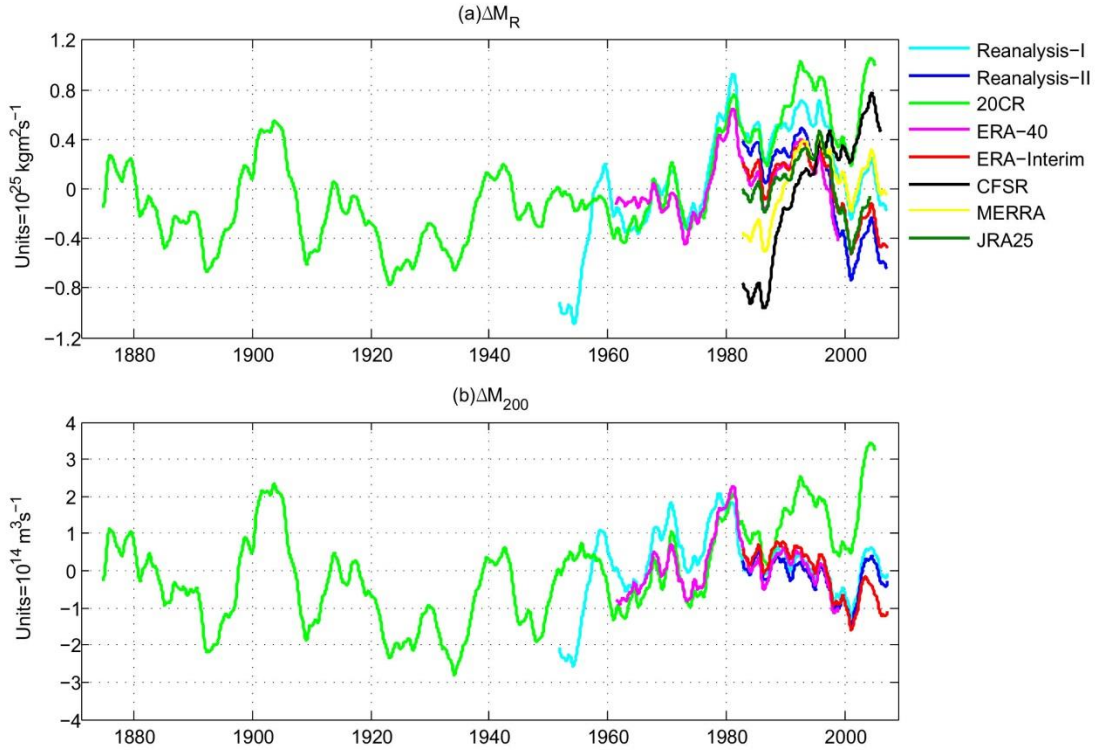
Figure 21: (a) The 5-year running averaged monthly anomalies of global relative angular momentum, ΔM_R, for the eight reanalysis datasets. (b) Same as (a) but for ΔM_{200}, the angular momentum (per unit pressure thickness) calculated at only 200 hPa level.

In the post-1970 era, all eight datasets qualitatively agree on the up and down in decadal variability of ΔM_R, although 20CR exhibits an overall upward trend from 1970-present that differs from the other datasets. The sharp increase in M_R during the 1976/77 transition, previously shown by Huang et al. (2001, 2003) using NCEP R-1, is robustly reproduced in other datasets including 20CR. In Fig. 21b, for ΔM_{200} the departure of

20CR from the other 4 datasets is substantial, while those 4 other datasets are tightly packed together for the last 20 years of record. This indicates that the discrepancy in ΔM_R between 20CR and other datasets in Fig. 21a comes mainly from the differences in the upper-level zonal wind. Given the agreement among all datasets on the increase in M_R during the 1976/77 transition, it is interesting to note that in the 140 years of record of 20CR the 1976/77 event has the most dramatic increase in M_R, followed by two other events in the 1940's and the 1890's, which however recovered immediately at the turn of the 20th Century.

6.3   Comparison of trend and the effect of detrending

Because the eight reanalysis datasets have varied lengths and cover very different periods, we investigate the trend in these datasets by looking at two periods, 1949-1978 and 1979-2008, each sees a substantial overlap of the coverages by multiple datasets. A least-square quadratic fit is applied to the ΔM_R time series to deduce the trend, and detrending is done by subtracting the quadratic curve from the time series as described in Sec. 6.3. We use selected five reanalyses but it does not affect the conclusion.

Figure 22a shows the quadratic fits for ΔM_R for NCEP R-1, 20CR, and ERA-40 for 1949-1978. Aside from the disagreement in the pre-1960 era between 20CR and NCEP R-1, which might be related to the quality of upper-air observation in pre-1960 era (Kistler et al. 2001), a good agreement is found in the post-1960 era among the three datasets on the overall trend and on the decadal variability after the data are detrended, as shown in Fig. 22b. Figures 22c and 22d are similar to Figs. 22a and 22b but for 1979-2008 and with the addition of NCEP R-2 and ERA-Interim data. Notably, while all

datasets that assimilated 3-D winds exhibit a downward trend in ΔM_R for this period, the 20CR data shows a mild upward trend instead. Nevertheless, once the data are detrended (Fig. 22d), all five datasets show remarkable agreements on the decadal-to-multidecadal variability over this period. In particular, detrending brings 20CR to a tighter agreement with all other datasets. This implies that the decadal-to-multidecadal variability in 20CR is trustworthy, only that the long-term trend needs to be treated with caution.
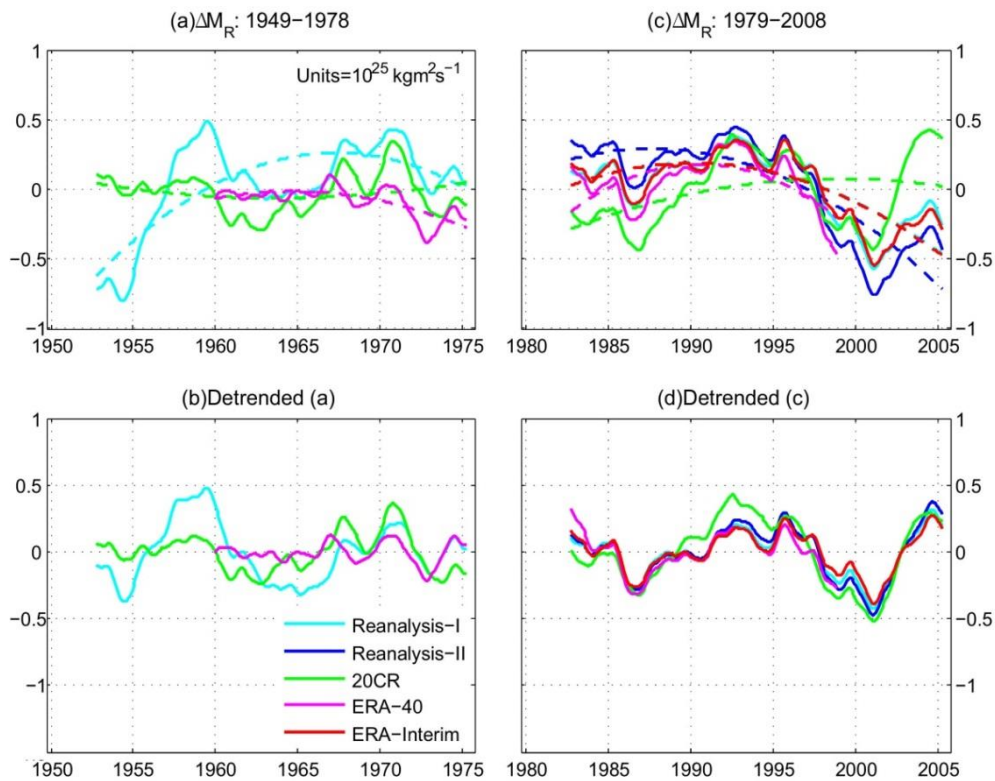
Figure 22: (a) The least-square quadratic fit (dashed curve) to ΔM_R for NCEP R-1, ERA-40, and 20CR for 1949-1978. (b) The "detrended" time series for the same period, with the quadratic curve removed from the time series. (c) As (a) but for 1979-2008 and with the addition of NCEP R-2 and ERA-Interim. (d) As (b) but for 1979-2008 and with the addition of NCEP R-2 and ERA-Interim.

While we regarded the quadratic curves from the least square fit in Figs. 22a and 22c as the "trend", they might alternatively be viewed as part of the ultra-low frequency variability on the centennial time scale, for which the 1979-2008 segment shown in Fig. 22c could be just a quarter of a full period (analogous to a winter season vs. the whole year). In this context, our use of the quadratic fit is meaningful since the time evolution within a quarter of an oscillation needs not be linear. Nevertheless, since the choice of the quadratic fit is somewhat a mathematical convenience, we next test the robustness of our conclusion by replacing it with a least square linear fit. Detrending is then performed by removing the straight line from the time series of ΔM_R, and the corresponding curves (not shown here) are qualitatively agreed on Figs. 22a-22d. In general, it remains true that detrending leads to much closer agreements among the reanalysis datasets.

6.4   Long-term mean

In the preceding sections we have removed the long-term mean in M_R to focus on low-frequency variability and trend. If the long-term mean is retained, i.e., if we consider M_R instead of ΔM_R, a systematic negative bias is found in 20CR compared to other reanalysis datasets, as shown in Figs. 23a (for M_R) and 23b (for M_{200}). While there also exist systematic differences in M_R among the other 4 reanalysis datasets, they are much smaller and the differences appear to diminish towards the last 20 years of record. For M_{200}, from 1990-present NCEP R-1 and R-2 clustered together, while ERA-40 agreed with ERA-Interim, but a systematic difference still exists between these two groups.

50
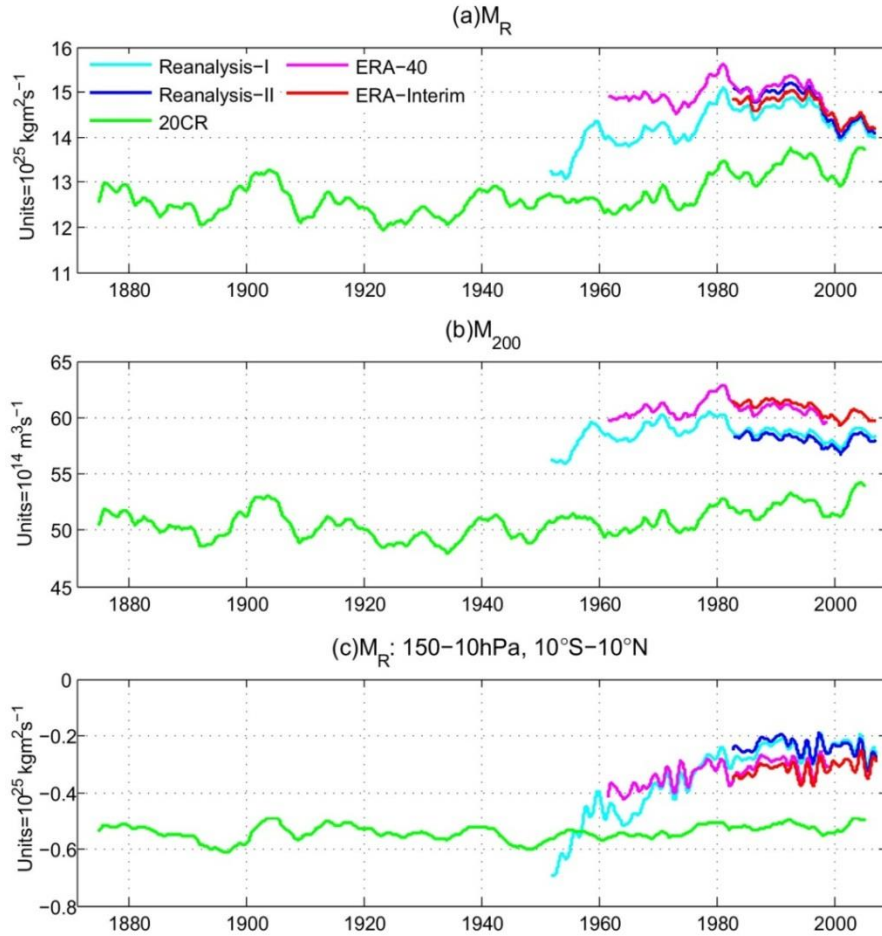
Figure 23: (a) The global relative angular momentum, M_R, with the long-term mean retained, for the five reanalysis datasets. (b) Same as (a) but for M_{200}. (c) Same as (a) but with the integration in Eq. (1) carried out only from 150-10hPa and $10°S$-$10°N$ to show the contribution from tropical upper atmosphere.

To visualize the differences in zonal mean zonal wind that contribute to the biases shown in Fig. 23, Figs. 24a, 24b, 24e, 24f, 24i and 24j show the 1979-2008 seasonal (June-August for summer and December-February for winter) and annual climatology of zonal mean zonal velocity for 20CR and ERA-Interim. The most notable difference is a stronger upper-tropospheric easterly flow on the equator in 20CR, which is further highlighted in Figs. 24c, 24g and 24k, the difference between 20CR and ERA-Interim.

51
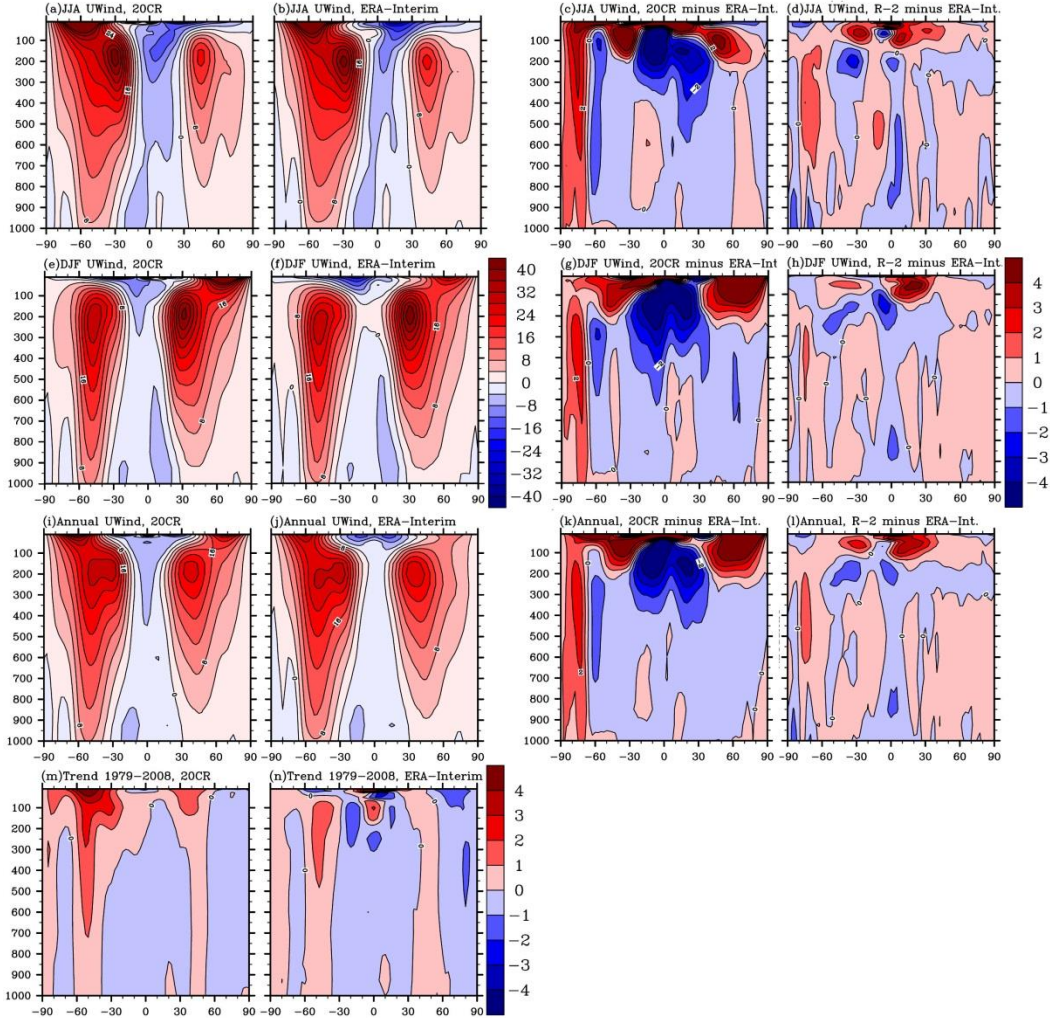
Figure 24: (a) The summer (June-August) climatology of zonal mean zonal wind from 1979-2008 for 20CR. (b) As (a) but for ERA-Interim. (c) The difference between 20CR and ERA-Interim, i.e., (b) minus (a). (d) is similar to (c) but for the difference between NCEP R-2 and ERA-Interim. (e)-(h) are similar to (a)-(d) but for winter (December-February). (i)-(l) are similar to (a)-(d) but for the annual mean. (m) and (n) are the 1979-2008 linear trends for 20CR and ERA-Interim. Contour intervals are 4 m s^{-1} for (a), (b), (e), (f), (i), and (j); 1 m s^{-1} for (c), (d), (g), (h), (k), (l), (m) and (n). Color scales are shown at right.

Figures 24c, 24g and 24k also show that the upper-tropospheric zonal wind is stronger in 20CR in the higher latitudes. This, however, does not overcome the negative bias in the tropics, which is more important for angular momentum due to the latitudinal weight $\cos^2\theta$ in the integral for M_R. Figures 24d, 24h and 24l are similar to Figs 24c, 24g

52

and 24k but for the difference between NCEP R-1 and ERA-Interim, which is considerably smaller than the difference between 20CR and ERA-Interim. The slightly lower value of the long-term mean of M_R in NCEP R-2 is also due to a stronger tropical easterly zonal wind.
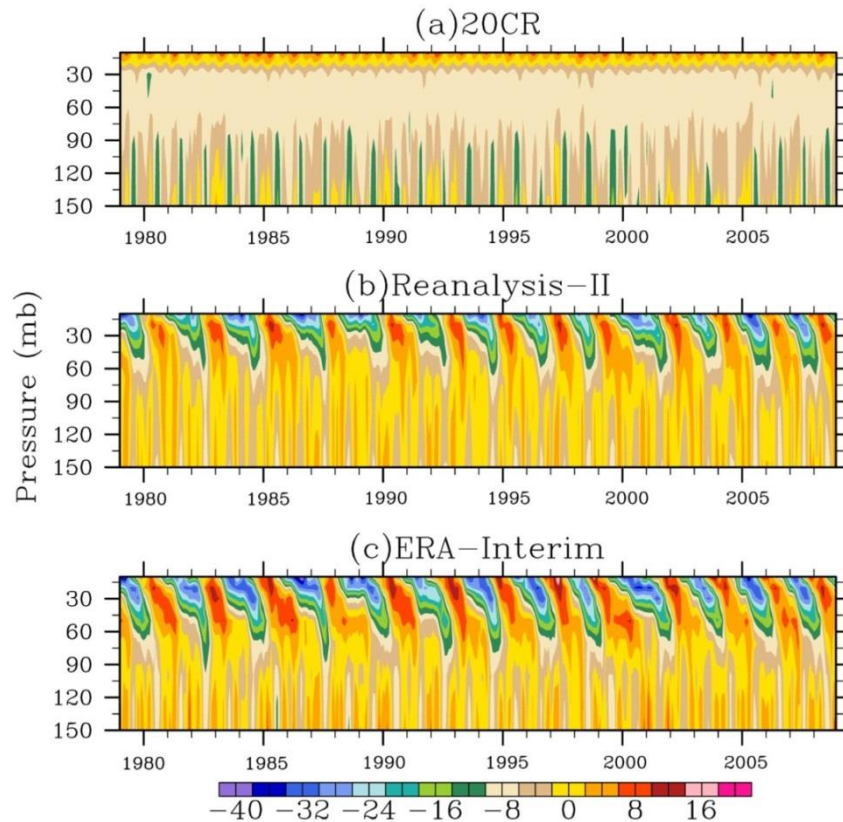
Figure 25: The time-pressure plots of zonal mean zonal wind on the equator from 150 to 10 hPa that illustrate the structure of QBO (or the lack of it) in (a) 20CR, (b) NCEP R-2, and (c) ERA-Interim. Monthly mean data are used without the 5-year running mean.

Although multiple factors may contribute to the difference in the long-term mean of M_R between 20CR and other reanalysis datasets, an important one to consider is the lack of realism in the stratosphere in 20CR. For example, Quasi-biennial Oscillation

53

(QBO) is entirely missing in 20CR, as demonstrated in Fig. 25. This leads to perpetual easterly zonal wind on the equator for 20CR, which contributes to a negative bias in M_R as further illustrated in Fig. 23c. Note that QBO itself has a nontrivial contribution to the variability of M_R (e.g., Chao 1989). This is not surprising since 20CR only assimilated the surface observation. A phenomenon that is initiated in the stratosphere then propagates or extends downward (e.g., in the sense of Baldwin and Dunkerton 1999 or Haynes et al. 1991) would not be correctly captured in the data assimilation process for 20CR. Although many of these phenomena have shorter periods, their absence could affect the long-term climatology.

Lastly, it is also interesting to show the trend in the zonal mean zonal wind that accompanies the trend in M_R. Figures 24m and 24n show the 1979-2008 linear trend of the zonal wind for 20CR and ERA-Interim. The increase in M_R during this period is associated in part with the strengthening of the two midlatitude zonal jets especially the one in the Southern Hemisphere; the trend has a strongly barotropic structure. The trend in the Southern Hemisphere zonal jet in 20CR is stronger than its counterpart in ERA-Interim. Again, this difference might ultimately come from the misrepresentation in 20CR of stratospheric processes that exert a downward influence on the zonal wind in the upper troposphere. The strengthening and poleward shift of the Southern Hemisphere zonal jet (which somewhat resembles the trend produced by double CO_2 in climate model simulations, e.g., Huang et al. 2001, Kushner et al. 2001, and is consistent with the findings on the expansion of the Hadley circulation, e.g., Seidel et al. 2008) is nevertheless qualitatively consistent between the two reanalysis datasets.

6.5   Conclusion

An intercomparison of the global relative angular momentum in eight reanalysis datasets reveals a good agreement on decadal-to-multidecadal variability among all datasets, including 20CR, for the 2nd half of the 20th Century. The discrepancies among different datasets are found to come mainly from the slowest component – the long-term trend – in the time series of angular momentum. Once the time series of ΔM_R are detrended, the resulted decadal-to-multidecadal variability shows even better agreements among all datasets. This key result, shown in Fig. 22d, is remarkable given that the variability of M_R is dominated by upper-tropospheric zonal wind while the 20CR datasets only assimilated surface observations. It indicates that 20CR can be reliably used for the analysis of decadal-to-interdecadal variability in the pre-1950 era, provided that the data is properly detrended. On the other hand, a nontrivial difference in the long-term trend exists between 20CR and other reanalysis datasets. Thus, one must exercise extreme caution when using 20CR to determine the trend on centennial time scale relevant to climate change. Although we have focused on angular momentum and zonal wind, the trend and low-frequency variability in M_R and zonal wind could potentially be used to cross validate those in temperature (e.g., Räisänen 2003, Allen and Sherwood 2008). Our results may provide a useful reference for such an analysis. Our conclusions pertain to the quantities that depend strongly on the upper-tropospheric zonal wind. The behavior of 20CR might be different for other climate indices that depend strongly on near-surface circulation and processes.

Chapter 7

7   SIMULATIONS: DECADAL-TO-INTERDECADAL VARIABILITY AND TREND

The long-term coupled model simulations archived by the Climate Model Intercomparison Project (CMIP) have served as an important basis for climate research and prediction. The scope of the multi-model intercomparison has also continued to expand, with a notable new focus being the validation and intercomparison of decadal-to-interdecadal variability. It is now recognized that a correct representation of decadal-to-interdecadal variability in the model is important for climate projection in the near term (e.g., Meehl et al. 2009), over which the trend induced by greenhouse-gas forcing does not yet fully overwhelm internal variability. Thus, it is useful to combine the intercomparisons of the trend and decadal-to-interdecadal variability for major climate variables. The validation of decadal-to-interdecadal variability in climate model simulations has seen limited progress, partly because one can extract only a small number of degrees of freedom for decadal/interdecadal oscillations from the short observational record. The recent construction of 20CR presented an opportunity to meaningfully validate the CMIP simulations of decadal-to-interdecadal variability. In a related work, by cross-validating multiple reanalysis datasets for the 2nd half of the 20th century, Paek and Huang (2012) affirmed the reliability of the decadal-to-interdecadal variability in 20CR. This allows us to confidently adopt the longer record in 20CR for model validation. For completeness, we will also compare the centennial trend in the CMIP simulations with 20CR, but with the caution that (as pointed out by Paek and Huang 2012)

there is less agreement among the reanalysis datasets concerning the trend in the 2nd half of the 20th century.

Given this background, this study will perform intercomparisons on the centennial trend and decadal-to-interdecadal variability for CMIP3 and CMIP5 simulations and validate them using the 20CR reanalysis. Relevant to this study, the total AAM has been found to increase under global warming in earlier versions (before CMIP3) of CMIP simulations for the 21st Century (Huang et al. 2001, de Viron et al. 2002, Räisänen 2003). Previous observational studies have also found an upward trend in AAM in the 2nd half of the 20th Century (Abarca del Rio 1999) and a sharp increase in AAM across the climate shift that occurred in 1976-77 (Huang et al. 2003, Paek and Huang 2012). These existing studies provide a useful background for the interpretation of the multi-model intercomparison in this study.

While the validation of the CMIP simulations can only be done for the 20th Century and the beginning of the 21st century, the intercomparison of the trend in CMIP3 and CMIP5 will be extended to the whole 21st century using the runs under strong greenhouse-gas forcing. We will also include a comparison of the decadal-to-interdecadal variability in the 20th and 21st centuries in CMIP simulations to determine if it is affected by greenhouse-gas forcing. Since the change in AAM largely reflects the variation of atmospheric circulation in the upper troposphere (e.g., Kang and Lau 1994, Huang and Sardeshmukh 2000), our analysis will complement those that focus on surface climate variables such as the global mean surface temperature. To aid the interpretation of the trend in AAM, we will also analyze the trend in zonal mean zonal wind.

57

7.1   Data and methodology

Tables 2 and 3 list the models in CMIP3 and CMIP5, respectively, that are used in this study. All models in CMIP3 are used. Because some simulations are still ongoing for CMIP5, we use only those that are currently available from the standard CMIP5 archive. Nevertheless, they already include the majority of CMIP5 models. For CMIP3, three types of centennial simulations are included: the "Historical" or "Climate of the 20th Century" (20C3M) runs that incorporate the aerosol and GHG forcing for the 20th Century; the "Pre-industrial control" (PICNTRL) runs under a fixed pre-industrial level of GHG concentration, and the 21st century simulations based on the "720 ppm stabilization" (SRES-A1B) scenario. For CMIP5, we likewise include those three types of runs. The "Historical" and "Pre-industrial control" runs are straightforward counterparts of CMIP3 while for the 21st century we analyze mainly the simulations under RCP8.5 scenario (detailed in Taylor et al. 2012). While the 20C3M group in CMIP3 and most members of the Historical and RCP8.5 groups in CMIP5 include multiple runs from each model, most of the SRES-A1B simulations in CMIP3 have only one run for each model. To give all models equal weight in the intercomparison, we choose only one run per model for all groups. A quick analysis of the multiple runs using the same model indicates that the ensemble members behave similarly such that adding them would not significantly alter our conclusion.

To validate the climate model simulations for the 20th century, the 20th Century Reanalysis (20CR) is used as the observation. Since we have recently found some differences in the climatological mean and trend in atmospheric angular momentum for the 2nd half of the 20th century between 20CR and other reanalysis datasets (Paek and

Huang 2012), we will also use the information from those additional datasets to partially address the uncertainty in reanalysis.

The main climate index used in this study, AAM is evaluated as Eqs. (4.1) and (4.2). The centennial trend of AAM (or the M_R or M_Ω component) is evaluated in a straightforward manner as the difference between the 20-year means of the last and first 20 years of a century. For the CMIP3 20C3M and CMIP5 Historical runs, the 20th century is considered. For the CMIP3 SRES-A1B and CMIP5 RCP8.5 runs, the 21st century is considered, except that a slightly shorter record from 2006-2099 is used for the latter since the RCP8.5 runs start from 2006. (In that case, the trend is calculated as 2080-2099 minus 2006-2025.) For the PICNTRL runs in CMIP3 and CMIP5, we only choose the last century of each run to evaluate the trend.

To quantify the decadal-to-interdecadal variability in the numerical simulations and observation, we perform spectral analysis on the angular momentum (focusing on M_R) using a centennial time series from the model output or reanalysis data. Because the CMIP5 RCP8.5 simulations cover only 2006-2099 to apply the same analysis to all four groups of CMIP3 and CMIP5 runs we choose to use only 94 years of data for each run (or observation): 1906-1999 for the 20th century and 2006-2099 for the 21st century. Each time-series of M_R is linearly detrended first, then transformed to frequency space using Fourier analysis. The decadal and interdecadal variances are defined as the sum of the power within the frequency bands with 7-15 year period and 16-35 year period, respectively,

$$variance \equiv \sum_{\omega_1 < \omega < \omega_2} |\Phi(\omega)|^2 \ , \tag{7.1}$$

59

where, ω is frequency (wavenumber in time) and $\Phi(\omega)$ is the Fourier component of the angular momentum with frequency ω. The variance or standard deviation is then used for the multi-model intercomparison and validation.

7.2   Relative angular momentum

7.2.1   Climatology and trend of M_R

Figure 26a shows the climatological value vs. centennial trend of the relative angular momentum, M_R, for the CMIP3 20C3M and SRES-A1B simulations. Since we have previously found some differences in the long-term mean of M_R for the 2nd half of the 20th century among the reanalysis datasets (Paek and Huang 2012b), to address the uncertainty in the reanalysis data we also add an extra point (a circle) to Fig. 26a with an adjustment on the climatological value for 20CR (but no alteration in the trend). The adjustment was deduced from the difference in the 1979-2007 climatology of M_R between 20CR and the ensemble mean of five reanalysis datasets used in Paek and Huang (2012b). Compared to the spread in the multi-model ensemble for either group of runs in Fig. 26a, the adjustment (or uncertainty in the reanalysis) is very small and does not affect our later discussions.

In Fig. 26a, the climatological value of M_R for 20C3M ranges from 13.6×10^{25} to 19.7 AMU, while its centennial trend for the 20th century ranges from 0.08 to 0.99 AMU with a multi-model ensemble mean of 0.48 AMU. All CMIP3 models produced a positive trend in M_R for the 20th century. This is qualitatively consistent with the 20CR reanalysis which exhibits a positive trend of 0.62 AMU for the 20th century. At the same time, the CMIP3 simulations all produced a greater climatological value of M_R (an ensemble mean

60

of 16.4 AMU) than the reanalysis (13.4 AMU). This indicates the propensity for the CMIP3 climate models to simulate either excessively strong westerly zonal jets in the subtropics and midlatitude or a muted easterly zonal flow on the equator, or both. The total M_R can be decomposed into a surface contribution and a baroclinc contribution (Räisänen 2003). The surface contributions are -2.5 AMU and -2.3 AMU for the CMIP3 ensemble mean and 20CR, respectively. In other words, the positive bias in M_R in CMIP3 comes mainly from the baroclinic contribution, which indicates that the models systematically exaggerate the meridional temperature gradient associated with the principal zonal jets.

In Fig. 26 we used the difference between 20CR (asterisk) and the average of four other reanalyses (circle) as a measure of the uncertainty of the climatological mean of M_R but did not extend this approach to the centennial trend (the ordinate in the figure). This is due to the concern that the "trends" deduced from the shorter (some cover only a few decades) reanalysis datasets could be part of interdecadal variability which do not represent the true nature of the centennial trend. We caution that uncertainty exists in the ordinate for the reanalysis in Fig. 26 which remains to be determined.

For the CMIP3 SRES-A1B runs, the trend in M_R for the 21st century ranges from 0.49 to 2.22 AMU with a multi-model ensemble mean of 1.14 AMU. The wide range indicates a still significant level of uncertainty in the projection. Nevertheless, all models produced a positive trend for the 21st century, consistent with previous studies using pre-CMIP3 simulations (Huang et al. 2001, de Viron et al. 2002, Räisänen 2003). For most models, the trend in the 21st century significantly exceeds that in the 20th century (the triangle in Fig. 26a is located far above the corresponding square), affirming the

dominant role of GHG forcing in producing the centennial trend. The numerical values of the trend in M_R are listed in Table 6. Similar quantities calculated from the CMIP3 PICNTRL runs are also listed in that table. Since there is no imposed long-term trend in the external forcing or boundary condition for the PICNTRL runs, the "centennial trends" from those runs are just the statistical residue of internal variability at centennial time scale. In some cases, climate drift might also be involved (Sen Gupta et al. 2012). The trends in the 20C3M and SRES-A1B simulations clearly rise above this level of statistical residue.

The climatological value and trend of M_R for the CMIP5 Historical and RCP8.5 runs are shown in Fig. 26b using the same arrangement as Fig. 26a. The numerical values of the trends are listed in Table 7. As a reference, the centennial "trends" (as a statistical residue of natural variability) of M_R from the CMIP5 PICNTRL runs are also listed in that table. For the CMIP5 Historical runs, the climatological value of M_R varies from 12.84 to 17.33 AMU with an ensemble mean of 14.83 AMU. Just like CMIP3, most of the CMIP5 models produced a climatological value of M_R that exceeds the observed value. Nevertheless, it is encouraging that the CMIP5 ensemble has moved much closer to the observation. Also notable is the narrowing of the spread of the CMIP5 Historical runs compared to CMIP3 20C3M. (The squares in Fig. 26b are more tightly packed together in the horizontal direction than their counterparts in Fig. 26a). The surface component of M_R is -2.3 AMU and the bias in the baroclinic component is reduced in the CMIP5 models compared to CMIP3. This shows an overall improvement in the simulated climatology of M_R from CMIP3 to CMIP5.
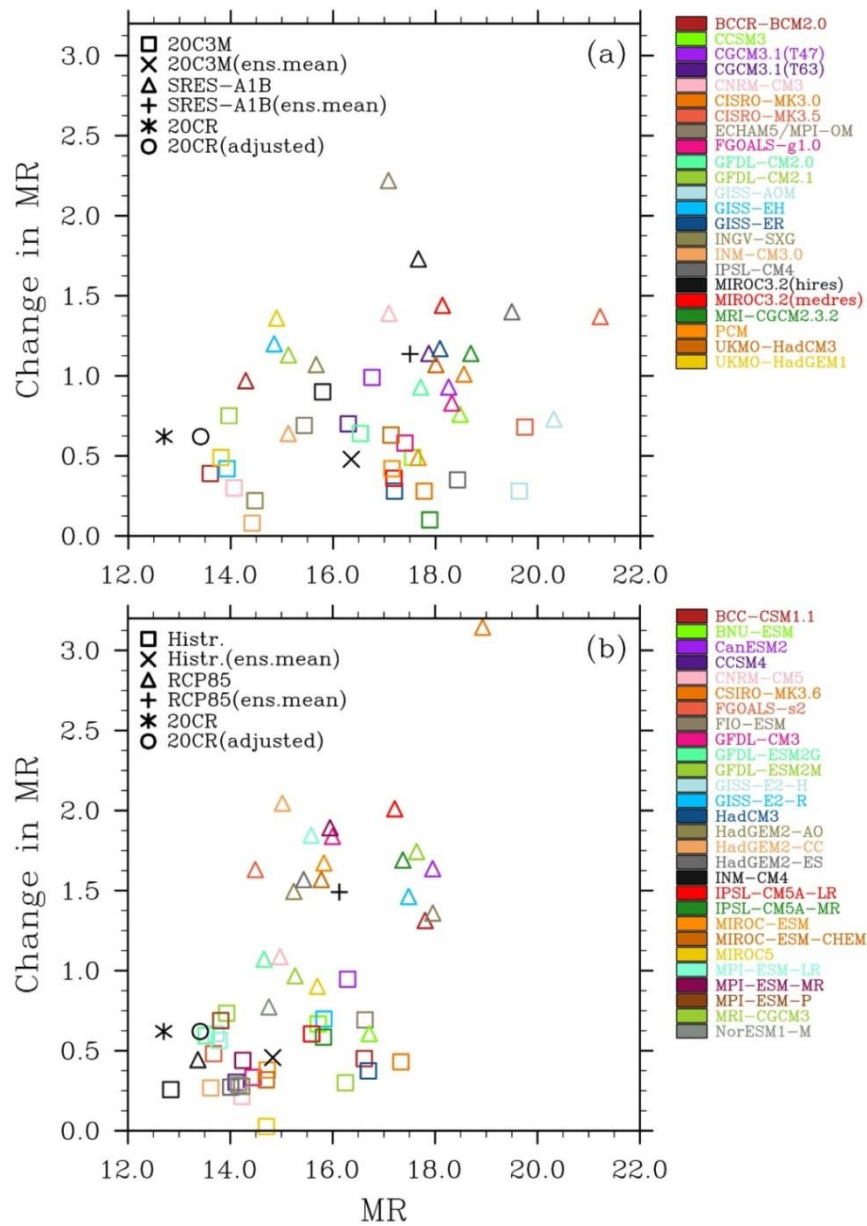
Figure 26: (a) The climatological value (abscissa) vs. the centennial trend (ordinate) of M_R for the CMIP3 20C3M (square) and SRES-A1B (triangle) simulations. (b) Same as (a) but for the CMIP5 Historical (square) and RCP8.5 (triangle) simulations. Each model is given a distinctive color as labeled at right. The multi-model ensemble means of the 20th and 21st century simulations are shown as a saltire and a cross, respectively. The observation for the 20th century from 20CR reanalysis is shown as an asterisk. The adjusted observation (see text) is shown as an open circle. The unit for M_R is AMU.

Table 6: A summary of the centennial trend in global atmospheric angular momentum and the equivalent change in LOD for CMIP3 simulations. Units are AMU for ΔM_R, ΔM_Ω and ΔAAM , and µs yr-1 for ΔLOD. The 20C3M and SRES-A1B runs are for the 20th and 21st century, respectively. The trend for the pre-industrial control (PICNTRL) runs is deduced from the last century of each simulation. An entry of "n.a." indicates that the required data for the specific calculation is not available from the CMIP3 archive. The observed values for the 20th century from 20CR reanalysis are listed at bottom.

No.	Model	20C3M (1980-99 minus 1901-20)				SRES-A1B (2080-99 minus 2001-20)				PICNTRL	
		ΔM_R	ΔM_Ω	ΔAAM	ΔLOD	ΔM_R	ΔM_Ω	ΔAAM	ΔLOD	ΔM_R	ΔM_Ω
1	BCCR-BCM2.0	0.39	0.12	0.52	1.1	0.97	0.50	1.47	3.1	0.16	0.05
2	CCSM3	0.49	0.15	0.64	1.4	0.76	0.37	1.13	2.4	-0.03	-0.02
3	CGCM3.1(T47)	0.99	0.00	0.99	2.1	0.93	0.16	1.09	2.3	0.17	0.10
4	CGCM3.1(T63)	0.70	0.01	0.71	1.5	1.14	0.16	1.30	2.8	-0.05	0.10
5	CNRM-CM3	0.30	0.17	0.47	1.0	1.39	0.50	1.89	4.0	-0.07	-0.07
6	CSIRO-MK3.0	0.28	0.11	0.39	0.8	1.01	n.a	n.a	n.a	-0.04	n.a
7	CSIRO-MK3.5	0.68	0.03	0.71	1.5	1.37	0.01	1.38	2.9	-0.28	0.14
8	ECHAM5/ MPI-OM	0.69	0.10	0.79	1.7	2.22	0.18	2.40	5.1	0.02	0.04
9	FGOALS-g1.0	0.58	-0.01	0.57	1.2	0.83	0.10	0.94	2.0	0.05	-0.04
10	GFDL-CM2.0	0.64	0.08	0.72	1.5	0.93	0.17	1.10	2.3	-0.17	0.12
11	GFDL-CM2.1	0.75	0.17	0.91	1.9	1.13	0.59	1.72	3.7	-0.02	-0.02
12	GISS-AOM	0.28	-0.05	0.23	0.5	0.73	0.44	1.17	2.5	0.00	-0.07
13	GISS-EH	0.42	0.03	0.45	1.0	1.20	0.22	1.42	3.0	-0.26	-0.04
14	GISS-ER	0.28	0.04	0.32	0.7	1.17	0.27	1.44	3.1	0.02	-0.07
15	INGV-SXG	0.22	0.04	0.27	0.6	1.07	0.07	1.13	2.4	-0.64	0.02
16	INM-CM3.0	0.08	0.05	0.13	0.3	0.64	0.00	0.65	1.4	0.19	-0.06
17	IPSL-CM4	0.35	0.04	0.39	0.8	1.40	0.16	1.55	3.3	0.12	0.05
18	MIROC3.2(hires)	0.90	0.26	1.16	2.5	1.73	0.65	2.38	5.1	0.12	n.a
19	MIROC3.2(medres)	0.36	0.16	0.52	1.1	1.44	0.68	2.12	4.5	0.07	-0.06
20	MRI-CGCM2.3.2	0.10	0.05	0.15	0.3	1.14	0.12	1.26	2.7	0.08	0.00
21	PCM	0.42	0.10	0.51	1.1	0.49	0.23	0.72	1.5	0.00	0.02
22	UKMO-HadCM3	0.63	-0.16	0.47	1.0	1.07	-0.22	0.85	1.8	0.12	-0.18
23	UKMO-HadGEM1	0.49	0.08	0.57	1.2	1.36	0.44	1.80	3.8	-0.26	-0.03
	Mean	0.479	0.069	0.547	1.16	1.136	0.263	1.405	2.99	-0.030	-0.002
	Standard deviation	0.240	0.088	0.261	0.56	0.373	0.231	0.487	1.04	0.191	0.077
	20CR	0.62	0.04	0.66	1.4						

Table 7: As Table 6 but for CMIP5. The Historical and RCP8.5 runs are for the 20th and 21st century, respectively. The trend for the pre-industrial control (PICNTRL) runs is deduced from the last century of each simulation.

		Historical (1980-99 minus 1901-20)				RCP8.5 (2080-99 minus 2006-25)				PICNTRL	
No.	Model	ΔM_R	ΔM_Ω	ΔAAM	ΔLOD	ΔM_R	ΔM_Ω	ΔAAM	ΔLOD	ΔM_R	ΔM_Ω
1	BCC-CSM1.1	0.45	0.18	0.63	1.35	1.31	0.63	1.94	4.41	-0.06	0.03
2	BNU-ESM	0.67	0.26	0.93	1.98	0.61	0.76	1.36	3.10	-0.16	-0.01
3	CanESM2	0.95	0.03	0.98	2.08	1.64	0.00	1.63	3.71	0.19	-0.06
4	CCSM4	0.30	0.14	0.45	0.95	n.a	n.a	n.a	n.a	n.a	n.a
5	CNRM-CM5	0.21	0.14	0.36	0.76	1.09	0.64	1.73	3.92	0.09	-0.10
6	CSIRO-Mk3.6	0.43	-0.01	0.42	0.90	3.15	0.16	3.31	7.51	-0.18	0.01
7	FGOALS-s2	0.48	0.11	0.59	1.26	1.63	0.17	1.80	4.09	-0.13	-0.06
8	FIO-ESM	0.69	0.20	0.89	1.90	1.36	0.65	2.01	4.57	-0.06	0.00
9	GFDL-CM3	0.33	0.08	0.42	0.89	1.84	1.07	2.90	6.59	0.10	0.03
10	GFDL-ESM2G	0.59	0.20	0.80	1.70	1.07	0.74	1.81	4.11	0.06	-0.01
11	GFDL-ESM2M	0.73	0.26	0.99	2.12	0.97	0.70	1.67	3.79	-0.14	-0.05
12	GISS-E2-H	0.61	0.08	0.68	1.45	n.a	n.a	n.a	n.a	-0.02	-0.06
13	GISS-E2-R	0.70	0.16	0.86	1.83	1.46	0.22	1.68	3.82	-0.04	-0.06
14	HadCM3	0.37	0.02	0.39	0.84	n.a	n.a	n.a	n.a	n.a	n.a
15	HadGEM2-AO	0.28	0.05	0.33	0.69	1.49	0.58	2.07	4.71	n.a	n.a
16	HadGEM2-CC	0.27	0.12	0.39	0.83	2.05	0.78	2.82	6.41	0.09	-0.03
17	HadGEM2-ES	0.27	0.00	0.27	0.57	1.57	0.60	2.17	4.92	-0.16	0.02
18	INM-CM4	0.26	0.10	0.36	0.76	0.44	0.06	0.50	1.14	-0.07	0.01
19	IPSL-CM5A-LR	0.60	0.13	0.74	1.57	2.01	0.28	2.29	5.21	0.07	-0.04
20	IPSL-CM5A-MR	0.58	0.09	0.67	1.43	1.69	0.37	2.07	4.69	0.19	0.07
21	MIROC-ESM	0.38	0.08	0.46	0.97	1.67	0.99	2.66	6.04	-0.08	-0.03
22	MIROC-ESM-CHEM	0.32	0.09	0.41	0.87	1.57	1.05	2.62	5.95	0.04	-0.05
23	MIROC5	0.03	0.13	0.16	0.34	0.90	0.94	1.84	4.19	-0.19	0.02
24	MPI-ESM-LR	0.56	0.10	0.67	1.42	1.85	0.21	2.06	4.67	0.14	0.00
25	MPI-ESM-MR	0.44	0.15	0.59	1.26	1.89	0.27	2.17	4.92	0.16	0.05
26	MPI-ESM-P	0.69	0.08	0.76	1.62	n.a	n.a	n.a	n.a	-0.04	0.01
27	MRI-CGCM3	0.30	0.09	0.39	0.83	1.74	0.04	1.78	4.04	0.19	0.01
28	NorESM1-M	0.29	0.12	0.40	0.86	0.77	0.55	1.32	3.01	0.01	-0.01
	Mean	0.457	0.114	0.571	1.215	1.491	0.519	2.010	4.562	-0.001	-0.013
	Standard deviation	0.205	0.068	0.232	0.494	0.564	0.331	0.584	1.326	0.124	0.041
	20CR	0.62	0.04	0.66	1.4						

65

The CMIP5 RCP8.5 simulations for the 21st century produced a significant centennial trend in M_R which ranges from 0.44 to 3.15 AMU with an ensemble mean of 1.49 AMU, comparable to its counterpart in CMIP3 A1B runs. The anthropogenic GHG forcing in the CMIP5-RCP8.5 and CMIP3-A1B runs are different (see Taylor et al. 2012, Moss et al. 2010). The RCP8.5 scenario is for a more severe increase in GHG concentration which generally leads to stronger future warming in the climate model projection; The 21st century trends (using the same definitions as those for angular momentum) of the global mean surface air temperature for the ensemble means of CMIP3 A1B and CMIP5 RCP8.5 are +2.1 °C and +3.4 °C, respectively. The trends in M_R from those two ensembles, if normalized by the respective trends in surface air temperature, are 0.54 and 0.44 AMU (°C)$^{-1}$ for CMIP3-A1B and CMIP5-RCP8.5. Like the 20th century runs, the spread of the CMIP5 ensemble of the climatology of M_R for the 21st century simulations has narrowed compared to CMIP3. Within CMIP5, because the multi-model ensembles of the 20th and 21st century runs have each become more tightly packed together, the separation between the two groups also becomes more distinctive as compared to CMIP3. (In Fig. 26a, the squares and triangles are mixed together while the two groups are more clearly separated in Fig. 26b.) Those quantitative differences aside, the results from CMIP3 and CMIP5 reaffirm the finding from the pre-CMIP3 studies (Huang et al. 2001, de Viron et al. 2002, Räisänen 2003) that GHG forcing induces a robust increase in the relative atmospheric angular momentum in the 21st century.

7.2.2   Zonal mean zonal wind

To relate the trend in M_R to changes in the upper-level zonal flow, the centennial trends (defined in a similar manner as that for M_R) of the annual zonal mean zonal wind for different groups of the CMIP runs and from reanalysis are shown in Fig. 27. Panels (c) and (d) are for CMIP3 20C3M and SRES-A1B runs and are consistent with a similar analysis for the zonal wind in CMIP3 already performed by Ihara and Kushnir (2009). The most robust feature in the 20th century simulations from both CMIP3 and CMIP5 (panel g) and 20CR reanalysis (panel a) is the intensification of zonal wind at around 60 °S and an accompanying weakening of zonal wind equatorward of it. This pattern is also prominent in the 21st century simulations from both CMIP3 (panel d) and CMIP5 (panel h). A similar structure has been identified in pre-CMIP3 simulations with GHG forcing, for example by Huang et al. (2001) and Kushner et al. (2001) who related it to a poleward shift of the Southern Hemisphere eddy-driven zonal jet.

While the structure of enhanced zonal wind at 60 °S appears in both 20th and 21st century runs (for both CMIP3 and CMIP5), in the Southern Hemisphere the 21st century simulations additionally produced an enhancement of the subtropical jet with the maximum of the trend confined to the upper troposphere. In the 20th century simulations (from both CMIP3 and CMIP5), this structure is much weaker and largely confined to the stratosphere.

In the Northern Hemisphere, the 21st century simulations from both CMIP3 and CMIP5 produced a poleward shift and enhancement of the westerly zonal jet, with a maximum of the trend in the upper troposphere. This poleward shift, along with its Southern Hemisphere counterpart, has previously been identified in the analyses of

67

CMIP3 and often discussed in the context of the poleward shift of storm tracks (e.g., Yin 2005). The 20th century simulations from both CMIP3 and CMIP5 also produce an enhancement of the westerly zonal jet in the northern Hemisphere but one cannot clearly identify a poleward shift of the jet. In 20CR, one can even see a hint of an enhancement and equatorward shift of the jet. This might have been influenced by the fact that the last 20 years of the 20th century includes several very strong El Nino events while the first 20 years of the century contains very few such events. (Note that an enhancement and equatorward shift of the Northern Hemisphere zonal jet is typical of the atmospheric response to El Nino.) By design, we do not expect the CMIP3 or CMIP5 20th century simulations to capture those specific El Nino events seen in observation. An alternative, but related, interpretation is that the absence of the equatorward shift of N. H. zonal jet might reflect a certain common bias in the climate models. Notably, Cai et al. (2009) pointed out that the common bias of a cold equatorial Central-Western Pacific SST in CMIP3 models generally leads to a muted atmospheric response to ENSO in those models. This might further weaken the footprint of El Nino on the N. H. zonal jet in the model simulations.
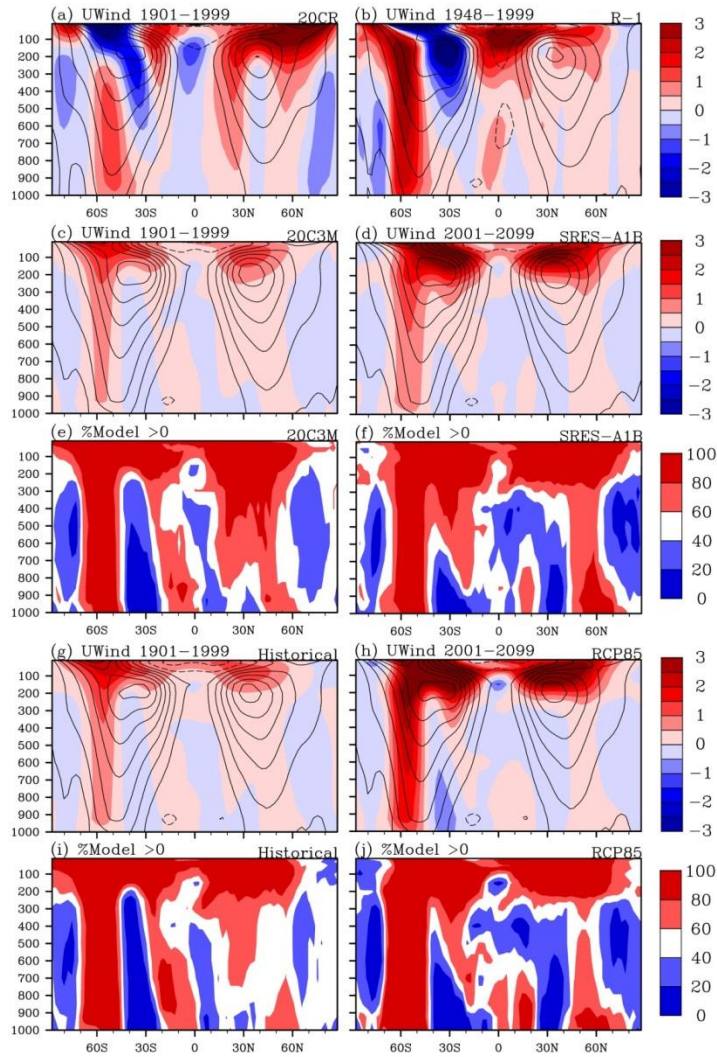
Figure 27: Panels (a), (c), (d), (g), and (h) show the centennial trend (the difference between the 20-year means of the last and first 20 years of a century; color shading) and the climatology of the first 20 years ("starting point") of the respective century (black contour) of annual zonal mean zonal wind from the observation and the ensemble mean of model simulations: (a) The observation for the 20th century from 20CR reanalysis; (c) The CMIP3 20C3M runs for the 20th century; (d) The CMIP3 A1B runs for the 21st century; (g) The CMIP5 Historical runs for the 20th century; (h) The CMIP5 RCP8.5 runs for the 21st century. Panel (b) is similar to (a) but the trend is for the second half of the 20th century as deduced from NCEP Reanalysis-I. The increment of the color shading for the trend is 0.5 m s^{-1}, with the scale shown at right. The contour interval for the black contours is 10 m s^{-1}. Panels (e), (f), (i) and (j) (each corresponds to the panel directly above it) show a measure of the consensus among the models. The color scale indicates the percent of models that produced a positive trend. Red (blue) means the majority produced a positive (negative) trend.

Paek and Huang (2012) have recently found some differences in the long-term mean and trend of atmospheric angular momentum for the 2nd half of the 20th century between 20CR and other reanalysis datasets that assimilated the 3-D observations. In Fig. 27, we use mainly 20CR to validate the 20th century simulations because it is the only reanalysis dataset with the centennial coverage. Nevertheless, as a reference we also show in Fig. 27b the trend in zonal mean zonal wind for only the 2nd half of the 20th century but from the NCEP Reanalysis-I (which has the second longest record next to 20CR). Even with the shorter period, the half-century trend has several structures that resemble the centennial trends in 20CR and the model simulations. Most notable among them is the poleward shift of the Southern Hemisphere eddy-driven jet that corresponds to a positive trend at 60 °S. Note that this is also the region where the CMIP3 and CMIP5 models show the highest level of consensus, as indicated in Figs 27e, 27f, 27i, and 27j. The half-century trend in Fig. 27b also shows an overall enhancement of the Northern Hemisphere westerly jet but its detailed structure differs from its counterpart in 20CR: The "equatorward shift" of the Northern Hemisphere subtropical jet in Fig. 27a is less pronounced in Fig. 27b. This hints that part of this feature might be a statistical residue of the internal variability and not a robust part of the long-term trend.

The trends in zonal wind in Fig. 27 consist of not only latitudinal shifts but also vertical (mostly upward) displacements of the zonal jets especially in the 21st century simulations.

To visualize the local contributions to the trend of M_R, the vertically integrated contributions of different vertical layers (10-200 hPa, 200-1000 hPa, and 10-1000 hPa) as a function of latitude (in the fashion of Fig. 4 in Räisänen 2003) are shown in Figs. 28a-28d for the ensemble means of the 4 sets of CMIP3 and CMIP5 runs. In all panels, the

70

Southern Hemisphere jet at 60 °S is found to be unique in that the local contribution to the trend in M_R is dominated by the trend in the zonal wind of the tropospheric column below 200 hPa (which reflects the latitudinal shift of the deep eddy-driven jet as mentioned before). Elsewhere, the increase in M_R associated with the subtropical jet in the Southern Hemisphere and the principal zonal jet in the Northern Hemisphere is dominated by the trend in zonal wind above 200 hPa level. Notably, for the 21st century simulations (panels b and d), at 30 °N the dominating positive contribution from the zonal wind above 200 hPa is accompanied by a smaller negative contribution from below 200 hPa, an indication of an upward shift and intensification of the jet core at that latitude.
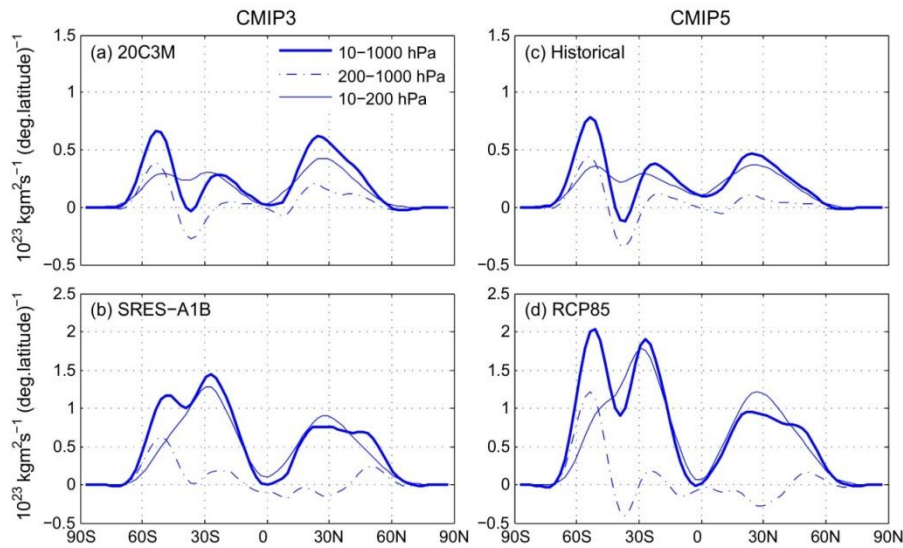
Figure 28: The contributions to the multi-model mean centennial trend (the difference between the 20-year means of the last and first 20 years of a century) in M_R from different vertical layers as a function of latitude. (a) CMIP3 20C3M runs, (b) CMIP3 SRES-A1B runs, (c) CMIP5 Histrorical runs. (d) CMIP5 RCP8.5 runs. The thick solid line is for the whole vertical column from 10 to 1000 hPa, thin solid line for the upper levels from 10-200 hPa, and the dot-dashed line for the lower levels from 200-1000 hPa. The unit is 10^{23} kg m^2 s^{-1} (1 °lat.)$^{-1}$.

7.3   Omega angular momentum

Figures 29a and 29b show the climatology vs. trend, in the same fashion as Fig. 26, for the "mass" or "omega" angular momentum, M_Ω, for CMIP3 and CMIP5 simulations. While the climatological value of M_Ω (from either observation or simulation) is much greater than M_R, the trend in M_Ω as shown in Figs. 29a and 29b is smaller than its counterpart in M_R such that the trend in the total AAM (= $M_R + M_\Omega$) is dominated by M_R. For the climatology of M_Ω from the 20th century simulations, the spread of the multi-model ensemble has narrowed substantially from CMIP3 to CMIP5 with the latter also moving much closer to the observation from 20CR.

In addition to M_Ω, we also calculated the total atmospheric mass which is proportional to $<p_s>$ where $<X>$ is the area-weighted global average of *X*. For the climatology of the 20th century, the multi-model ensemble mean of $<p_s>$ for the CMIP3 20C3M runs is 985.2 hPa, compared to 985.6 hPa for 20CR. The inter-model standard deviation of $<p_s>$ for CMIP3 20C3M is 1.1 hPa. In contrast, the multi-model ensemble mean of $<p_s cos^2\theta>$ (which is proportional to M_Ω) for CMIP3 20C3M is 661.9 hPa compared to 661.6 hPa for 20CR, and the inter-model standard deviation of that quantity is 2.6 hPa, more than twice its counterpart for $<p_s>$. This suggests that the bias and inter-model variation in M_Ω for the climate models are due to not only the variation of total mass but also substantial contributions from the differences in the meridional distribution of ps. This remark also generally holds for CMIP5 Historical runs, which otherwise has a smaller bias and ensemble spread for both $<p_s>$ and $<p_s cos^2\theta>$ compared to CMIP3 20C3M; The (ensemble mean, standard deviation) of $<p_s>$ and $<p_s cos^2\theta>$ for CMIP5 are (985.1, 0.8) hPa and (661.5, 0.6) hPa, respectively.
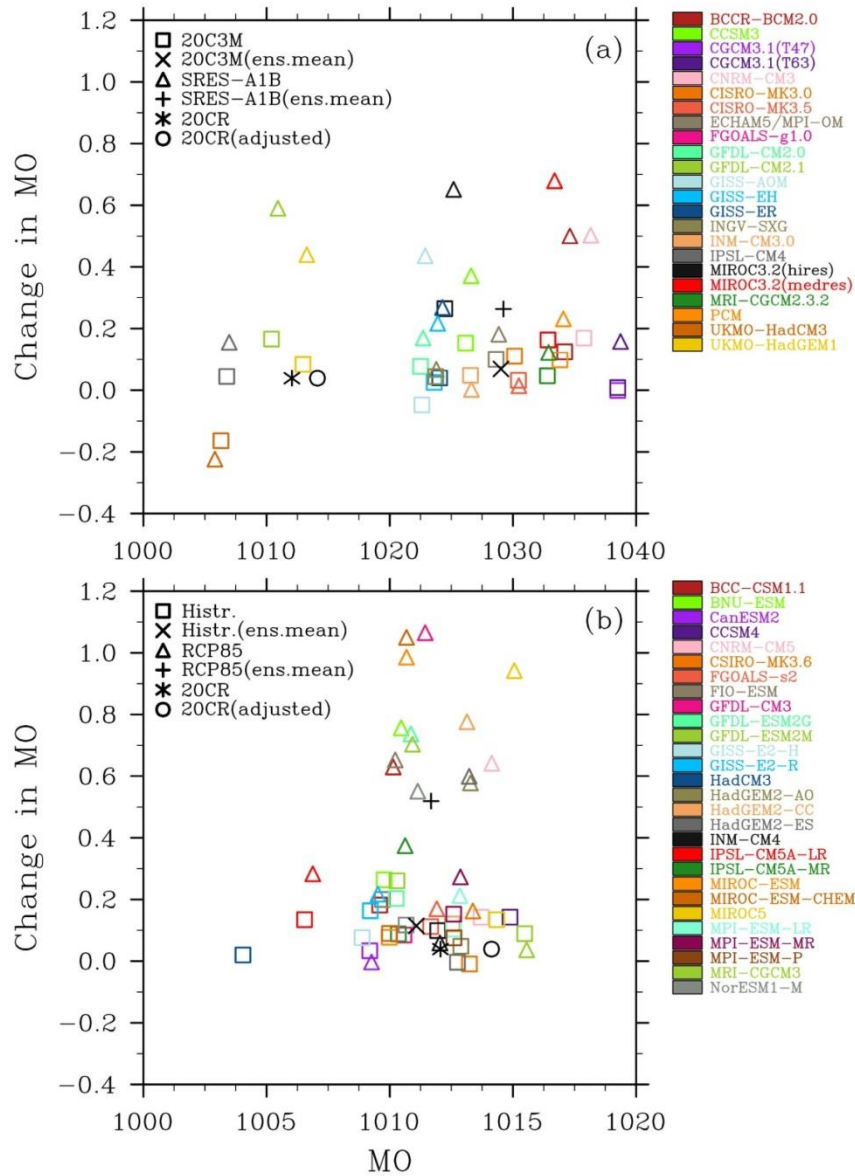
Figure 29: Similar to Fig. 26 but for the climatology and trend of the omega angular momentum. (a) The 20C3M (square) and A1B (triangle) runs from CMIP3. (b) The Historical (square) and RCP8.5 (triangle) runs from CMIP5. Note that the scale on the abscissa in panel (b) is only a half of that in panel (a). A model in CMIP3 produced an unusually large climatological value of M_Ω (over 1100 AMU) that is outside the range and not shown in panel (a). The unit for M_Ω is AMU.
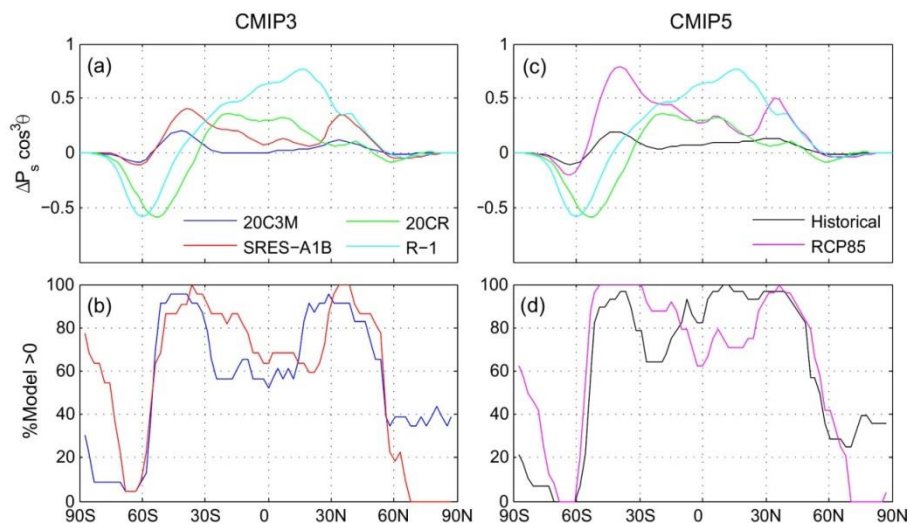
Figure 30: (a) The centennial trend (the difference between the 20-year means of the last and first 20 years of a century) in the annual zonal-mean surface pressure weighted by $\cos^3\theta$ from the ensemble mean of the CMIP3 20C3M runs (dark blue) and 20CR reanalysis (green), both for the 20th century, and from the CMIP3 A1B runs (red) for the 21st century. Also shown is the observed trend for only the second half of the 20th century from the NCEP Reanalysis-I (light blue). (b) The measure of consensus among the models as a function of latitude, for the CMIP 20C3M (dark blue) and A1B (red) runs. The ordinate is the percent of models that produced a positive trend as the ensemble mean of the trend. (c) Similar to (a) but the black and magenta curves are for the CMIP5 Historical and RCP8.5 runs, respectively. The two curves for the observation are copied from (a) and imposed to this panel as a reference. (d) Similar to (b) but the black and magenta curves are for the CMIP5 Historical and RCP8.5 runs, respectively. The unit for the surface pressure in (a) and (c) is hPa.

The multi-model ensemble means of the trends in M_Ω for the 20th century are 0.07

and 0.11 AMU from the CMIP3 20C3M and CMIP5 Historical runs while the

corresponding trend deduced from 20CR is 0.04 AMU. All three are small numbers

compared to their counterparts for M_R. With the small trend, it is not surprising that the

three numbers do not strongly agree with each other (although they are all positive). To

see where the difference comes from, Figs. 30a and 30c show the 20th and 21st century

trend in annual zonal-mean surface pressure weighted by $cos^3\theta$ from the CMIP3 and

74

CMIP5 runs, and 20CR. The half-century trend from NCEP Reanalysis-I (see the discussion in Sec. 7.1) is also shown. Figures 30a and 30c show an increase in the surface pressure in the tropics in reanalysis that is largely absent in the 20C3M and Historical runs (although the latter produced a small positive value across the tropics). On the other hand, the CMIP3 and CMIP5 simulations produced a "ridge" at around 45$°$S that is missing in 20CR and barely visible in NCEP R-1. Qualitatively, the two reanalyses and the CMIP3 and CMIP5 simulations all show a dip in surface pressure south of 60$°$S and an enhancement of meridional pressure gradient across the midlatitude of the Southern Hemisphere (consistent with the positive trend in zonal wind at 60$°$S shown in Fig. 27), although the dip is more pronounced for the reanalyses. Qualitatively, we find less agreement among the reanalyses and CMIP runs in the trend of surface pressure for the Northern Hemisphere, a behavior similar to the trend in zonal wind discussed in Sec. 7.2.2. To complement the ensemble mean shown in Figs. 30a and 30c, the multi-model "consensus" (defined in the same manner as Figs. 27e, 27f, 27i, and 27j) on the trend in surface pressure for the CMIP3 and CMIP5 simulations is shown in Figs. 30b and 30d. We find that the level of consensus has increased from CMIP3 to CMIP5.

The majority of the CMIP3 and CMIP5 models produce a positive trend in MΩ for the 21st century. The multi-model ensemble means of the trend are 0.26 and 0.52 AMU for the SRES-A1B and RCP8.5 runs, respectively. They are both significantly greater than their counterparts from the 20th century simulations, reflecting the influence of GHG forcing in producing the trends in the 21st century. This is qualitatively consistent with some previous studies using pre-CMIP3 simulations (Huang et al. 2001, Räisänen 2003), although a rigorous comparison is difficult since only a small number of

the models in the pre-CMIP3 archives have the surface pressure data. As pointed out by Räisänen (2003), the calculation of M_Ω can be sensitive to the procedure of converting sea level pressure and temperature to surface pressure. (Another study by de Viron et al. 2002 obtained a more negative trend in M_Ω for CMIP2.) The calculations of the $M\Omega$ in Figs. 29a and 29b directly used the surface pressure data in CMIP3 and CMIP5 archives and are devoid of the technical ambiguity raised by Räisänen (2003).

The 21st century trend in the zonal mean surface pressure from the CMIP3 and CMIP5 simulations are shown in Figs. 30a and 30c. They share a similar structure of a pair of "ridges" in the midlatitude in both hemispheres, in contrast to the 20th century simulations which produced only a ridge in the Southern Hemisphere. This corroborates the structure of the trend in zonal wind in Fig. 27 that the 21st century runs produced a poleward shift of the zonal jets in both hemispheres while for the 20th century runs the poleward shift is robust only in the Southern Hemisphere. For completeness, the level of consensus for the 21st century runs is also shown in Figs. 30b and 30d for CMIP3 and CMIP5, respectively. Again, CMIP5 models exhibit a higher level of consensus in this case.

7.4   Total AAM and LOD

Some previous studies have pointed out that the projected increase in the total AAM would imply a slowing down of Earth rotation or an increase in the length-of-day (LOD) (Abarca del Rio 1999, Huang et al. 2001, de Viron et al. 2002). On the interannual and shorter time scales, the total of Earth plus atmospheric angular momentum is nearly conserved such that the tendencies of AAM and Earth angular momentum are equal and

opposite in sign. This is no longer the case on centennial time scale due to the influences of tidal friction and other slow geological processes (such as post-glacial rebound) in the long term. Nevertheless, if the GHG-induced trend in AAM is large enough, it can still affect the total trend in LOD (Huang et al. 2001).

In that context, we adopted a commonly used empirical formula as Eq. (4.3) to convert the change in AAM for the CMIP simulations to an equivalent change in LOD as listed in Tables 6 and 7. Focusing on the 21st century, the multi-model ensemble means of the trend, ΔLOD, are 0.30 and 0.46 ms per century for the CMIP3 SRES-A1B and CMIP5 RCP8.5 simulations, respectively. They are comparable to previous findings using pre-CMIP3 simulations (e.g. Huang et al. 2001). Since the changes in LOD due to tidal friction and post-glacial rebound are about +2.3 and -0.6 ms per century, respectively (see a survey in Huang et al. 2001), the impact of the GHG-induced change in LOD is projected to be significant in the 21st century but not large enough to overwhelm the secular trend due to the astronomical and geological effects.

7.5   Decadal-to-interdecadal variability

We next quantify and compare the decadal-to-interdecadal variability in the CMIP3 and CMIP5 simulations by the spectral analysis described in Section 2.2. The magnitudes of the decadal and interdecadal variability are measured by the cumulative variance of the Fourier modes within the 7-15 yr and 16-35 yr bands. Because the variances of M_Ω in the decadal and interdecadal frequency bands are much smaller than their counterparts for M_R, we will focus only on M_R. (Note that the dominance of M_R

over M_Ω is also well known for interannual and shorter-term variability, e.g., Huang et al. 2003.)
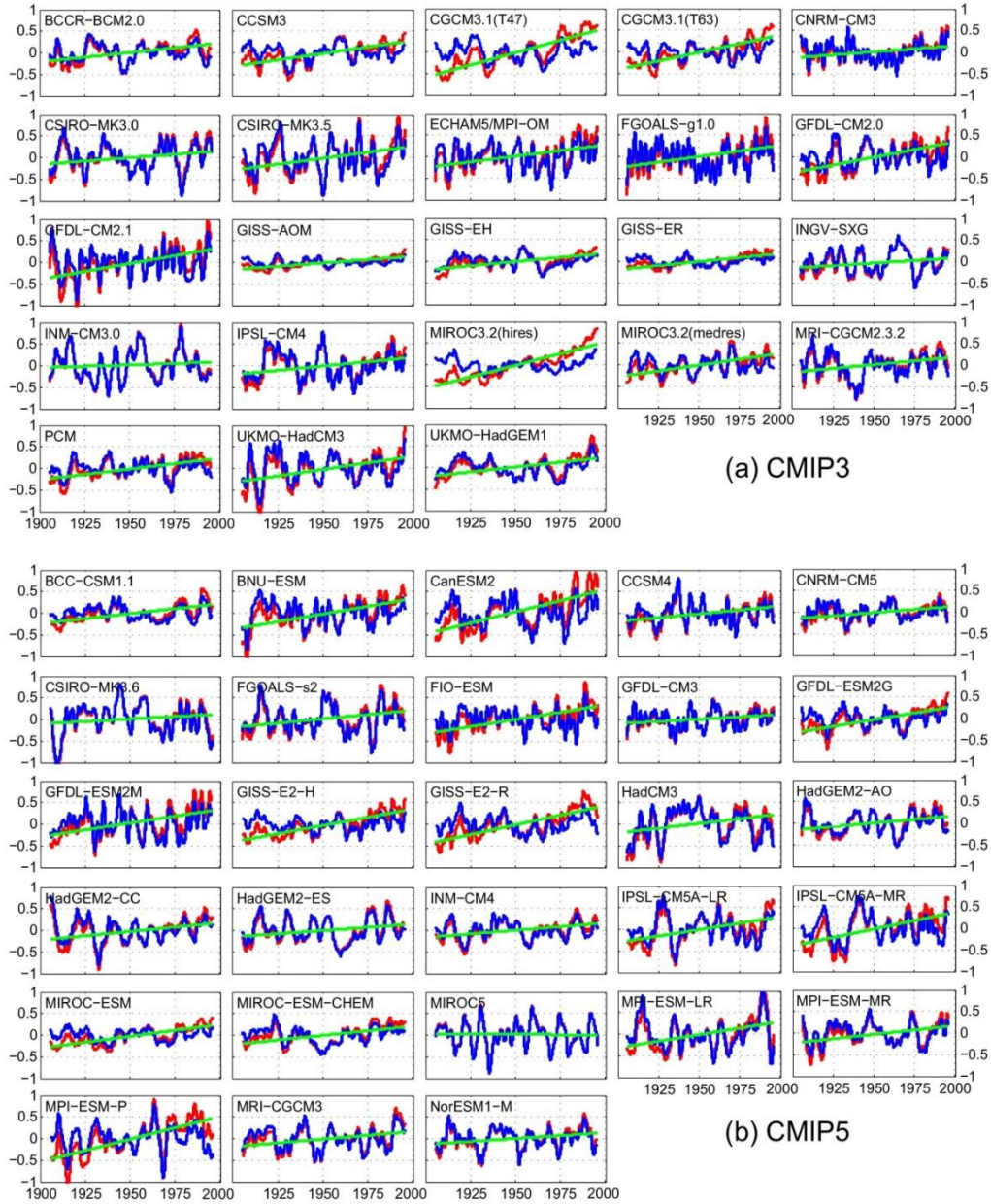
Figure 31: (a) Five-year running averaged monthly anomalies of global relative angular momentum (M_R) from the CMIP3 20C3M simulations. The red curve is the time series with the running average, green line the linear trend, and blue curve the detrended time series. To help visualization, the time series shown are the departure from the long-term mean (which is different for different models) for each individual model. (b) Same as (a) but for the Historical runs from CMIP5. The unit is AMU.
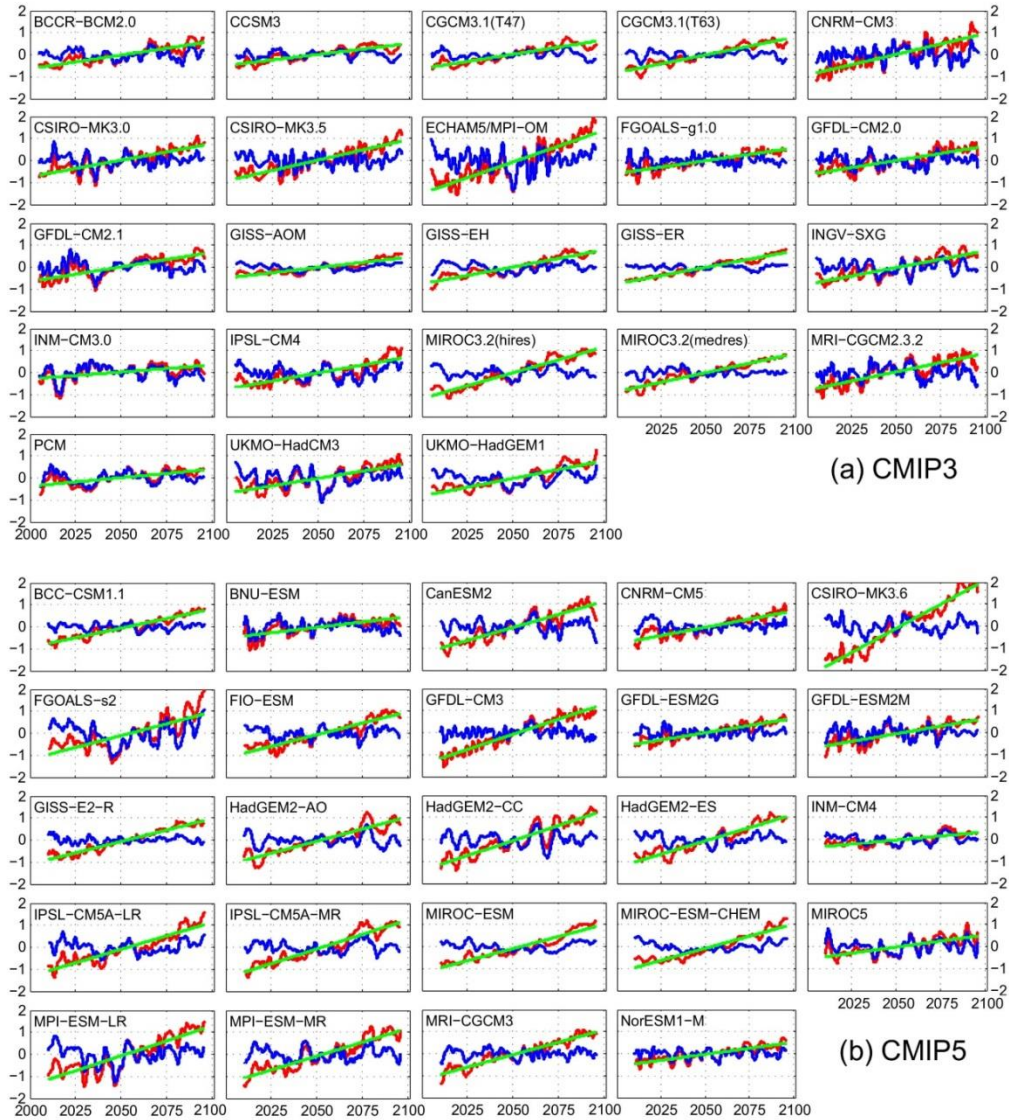
Figure 32: (a) Similar to Fig. 31 but for the SRES-A1B runs from CMIP3. (b) Same as (a) but for the RCP8.5 runs from CMIP5. Note that the scale on the ordinate is double that in Fig. 31.

To help visualize the behavior of the decadal-to-interdecadal variability of M_R in CMIP simulations, Figs. 31 and 32 show the 5-year running averaged time series of M_R (red curve), its linear trend (green line), and the corresponding detrended time series (blue curve) for all available CMIP3 and CMIP5 simulations for the 20th and 21st century.

79

From these figures, one can immediately see a very wide range of behavior of the simulated decadal-to-interdecadal variability, in contrast to the more robust upward trend in M_R for the 20th and 21st century produced by the majority of the models. From Fig. 32, the GHG-induced centennial trend of M_R for the 21st century is strong enough to overwhelm the background decadal-to-interdecadal variability. This is not so for the 20th century (Fig. 31), in which decadal-to-interdecadal variability can sometimes override the relatively weak secular trend.

Figures 33a and 33b are scatter plots of the standard deviation (square root of variance) of decadal variability (abscissa) vs. the standard deviation of interdecadal variability (ordinate) of M_R. For the convenience of comparing them to observation, the standard deviation of the simulated M_R for the decadal or interdecadal band is normalized by its counterpart from the 20CR reanalysis. The observation (20CR, shown as an asterisk) itself is located at (1.0, 1.0) in both panels in Fig. 33. For the 20th century runs from CMIP3 and CMIP5, although the scatter plots show a wide spread of the simulated decadal or interdecadal standard deviation, the bias in the decadal or interdecadal variability is more random compared to the systematic bias in the climatology of M_R in Fig. 26. As such, the average over all models brings the ensemble mean of the square root of variance (the saltire or "X" in Fig. 33) close to observation. The spread for both decadal and interdecadal variability is also found to narrow from CMIP3 to CMIP5. Most notably, the outliers in CMIP3 with unusually weak decadal/interdecadal variability (the symbols in the lower-left corner of Fig. 33a) are absent in CMIP5. Nevertheless, the narrowing of spread for the decadal/interdecadal variability is much less dramatic than

80

the case for the climatology of M_R in Figs. 26 and 29. These characteristics about the spread also hold true for the 21st century simulations (triangles) in Fig. 33.
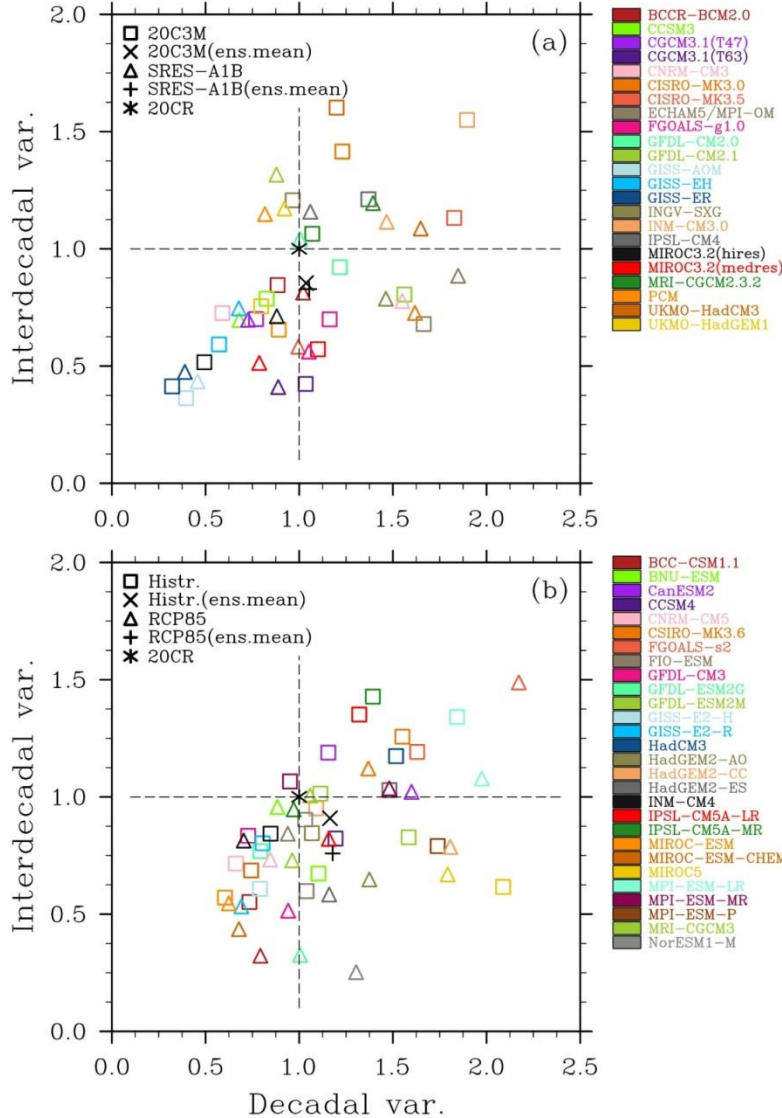
Figure 33: (a) The standard deviation of decadal variability (abscissa) vs. the standard deviation of interdecadal variability (ordinate) for M_R from the CMIP3 20C3M (square) and SRES-A1B (triangle) simulations. The multi-model ensemble means of the 20C3M and A1B runs are also shown as a saltire and a cross. The observation from 20CR is shown as an asterisk. To help the model validation, all quantities shown are normalized by their observed values (0.16 and 0.12 AMU for decadal and interdecadal variance, respectively) such that the observation itself is located at (1.0, 1.0) in the plot. Each model is given a distinctive color as labeled at right. (b) Similar to (a) but for the CMIP5 Historical (square) and RCP8.5 (triangle) runs.

Unlike Figs. 26 and 29 that show a clear change in the climatology from the 20th to the 21st century (a clear separation of the triangles and squares in those figures), in Fig. 33 the 20th and 21st century simulations are still mixed together without a clear trend. For both CMIP3 and CMIP5 simulations, using Welch's t-test, we cannot establish a shift in the mean from the 20th to the 21st century at 95% significant level for either decadal or interdecadal variability in Fig. 33. Since the probability distributions of the quantities in Fig. 33 may deviate from Gaussian (due to the presence of significant outliers), we have also used the Kolmogorov-Smirnov test to reconfirm that the ensembles of the 20th and 21st runs are not yet statistically distinguishable. Thus, the GHG forcing in the 21st century does not have as significant an influence on the decadal-to-interdecadal variability of M_R as it does on the climatological mean of M_R.

7.6   Conclusion

This study analyzed the centennial climatology, trend, and decadal-to-interdecadal variability of atmospheric angular momentum for the CMIP3 and CMIP5 simulations and validated them using the 20CR reanalysis. Both CMIP3 and CMIP5 models are found to produce a positive bias in the 20th century climatology of M_R but this bias is significantly reduced in CMIP5. The CMIP5 models also produced a narrower ensemble spread of the climatology and trend of both components (M_R and M_Ω) of angular momentum for the 20th century. An increase in both M_R and M_Ω is simulated by both CMIP3 and CMIP5 models and for the 20th and 21st century. The trend in the total angular momentum is dominated by the M_R component. The simulated increase in M_R for the 20th century is

82

consistent with observation. In all cases, the simulated trend in the 21st century is much greater than its 20th-century counterpart, affirming the role of the GHG forcing in producing the trend.

Both CMIP3 and CMIP5 simulations exhibit a wide range of behavior for the decadal-to-interdecadal variability. Using the standard deviation (square root of variance) of the M_R time series within the 7-15 yr and 16-35 yr band to define the magnitude of the decadal and interdecadal variability, it is found that the magnitude of the decadal or interdecadal variability for an individual model can vary from a half to twice of the observed value. Nevertheless, the bias in the decadal and interdecadal variability is relatively random, in contrast to the systematic bias in the climatology of M_R. As such, the multi-model averaging brings the ensemble mean of the magnitude of decadal or interdecadal variability to within 18% of the observed value for the 20th century. The CMIP5 simulations produced a slightly narrower ensemble spread in the decadal or interdecadal standard deviation compared to CMIP3. A notable type of outliers in CMIP3 with very weak decadal-to-interdecadal variability is absent in CMIP5. Otherwise, the CMIP3 and CMIP5 ensemble are close enough that the ensemble means of CMIP3 and CMIP5 are not statistically distinguishable for either the 20th or 21st century. More importantly, the 21st-century simulations from both CMIP3 and CMIP5 produced only a small trend in the decadal or interdecadal variability which is not statistically significant. Our results indicate that while the GHG forcing induces a significant increase in the climatological mean of atmospheric angular momentum, it does not significantly affect its decadal-to-interdecadal variability in the 21st century.

Chapter 8

8 SIMULATIONS: AGCM RESPONSE FORCED BY SST OF CMIP5 SIMULATIONS

Understanding the relation between the climate response to the forcing has been central to future climate projections. Many studies have been carried using AGCM simulations forced by the observed SST as a lower boundary condition (e.g., Graham et al. 1994, Lau 1997, Alexander et al. 2002, Compo and Sardeshmukh 2009, Deser and Phillips 2009) for present, and forced by the idealized SST of CMIP3 simulations (e.g., Schneider et al. 2009, Alexander et al. 2010, Hoerling et al. 2011) for future projections. Another study of Stephenson and Held (1993) diagnosed the AOGCM response under doubled CO_2 by using AGCM forced by prescribed SST taken from AOGCM. It showed the importance of the lower boundary condition to reproduce the original AOGCM response by AGCM simulations. With the outstanding improvement of the recent CMIP models (Taylor et al. 2012), extending to previous studies, this study will compare AGCM response forced by SST of CMIP5 simulations with the atmospheric states of the original CMIP5 simulations.

Our hypothesis is that the increased SST due to increased GHG forcing will force changes in the global atmospheric circulation as a boundary condition, enhance the subtropical zonal jets and increase M_R substantially. The aim of this study is to investigate the connection between SST and the tropospheric response in the warming world.

8.1   Numerical Experiments

The AGCM used in this study is the NCAR CAM 3.1 with T42 horizontal resolution (equivalent to 2.8°) and 26 hybrid vertical levels (Collins et al. 2006; see section 3.3). The model is initialized, and forced by default datasets and values provided with the model (e.g., ozone, solar constant), except sea surface temperature and sea ice concentration (SST hereafter including sea ice concentration). The repeated seasonal cycle AGCM experiments (hereafter AGCM) consist of 30-year runs forced by idealized global SSTs, which are constructed from the means of year 1981-2000 (hereafter 20C) in Historical simulations and year 2081-2100 (hereafter 21C) in RCP8.5 simulations from the CMIP5 models (hereafter AOGCM) in Table 8. The selection of the future scenario is arbitrary, but RCP8.5 will be expected to have more robustness in response than other scenarios because it has higher greenhouse gas (GHG) concentration (equivalent radiative forcing of 8.5 W m^{-2} and CO_2 concentration 1370 ppm in the year 2100) than other RCPs (Moss et al. 2010). The identical CO_2 concentration (355ppm as a default) is used for the AGCM experiments forced by both 20C and 21C SSTs because SSTs of RCP8.5 simulations carry radiative forcing effects by themselves as illustrated with globally increased SSTs in Fig. 34a. Note that the atmospheric component of CCSM4 is CAM4, which has improved finite volume core compared to the spectral core in CAM3 (Gent et al. 2011).

Table 8: A summary of the CMIP5 datasets used in Chapter 8.

Institute	Model	Resolution (Atmosphere)[1]	(Vertical level)[2]
Canadian Centre for Climate Modelling and Analysis (CCCma)	CanESM2	1.875 °×1.875 °L35	L22 (1-1000 hPa)
National Center for Atmospheric Research (NCAR)	CCSM4	1.25 °×0.9 °L26	L17 (10-1000 hPa)
Geophysical Fluid Dynamics Laboratory (GFDL)	GFDL-ESM2M	2.5 °×2.5 °L35	L17 (10-1000 hPa)
Met Office Hadley Centre (MOHC)	HadGEM2-ES	1.875 °×1.25 °L38	L17 (1-1000 hPa)
Atmosphere and Ocean Research Institute (The University of Tokyo), National Institute for Environmental Studies, and Japan Agency for Marine-Earth Science and Technology (MIROC)	MIROC-ESM	2.8 °×2.8 °L80	L35 (0.03-1000 hPa)
Max Planck Institute for Meteorology (MPI-M)	MPI-ESM-LR	1.875 °×1.875 °L47	L25 (0.1-1000 hPa)

[1] for the original components of the models

[2] for the provided data at http://pcmdi3.llnl.gov.
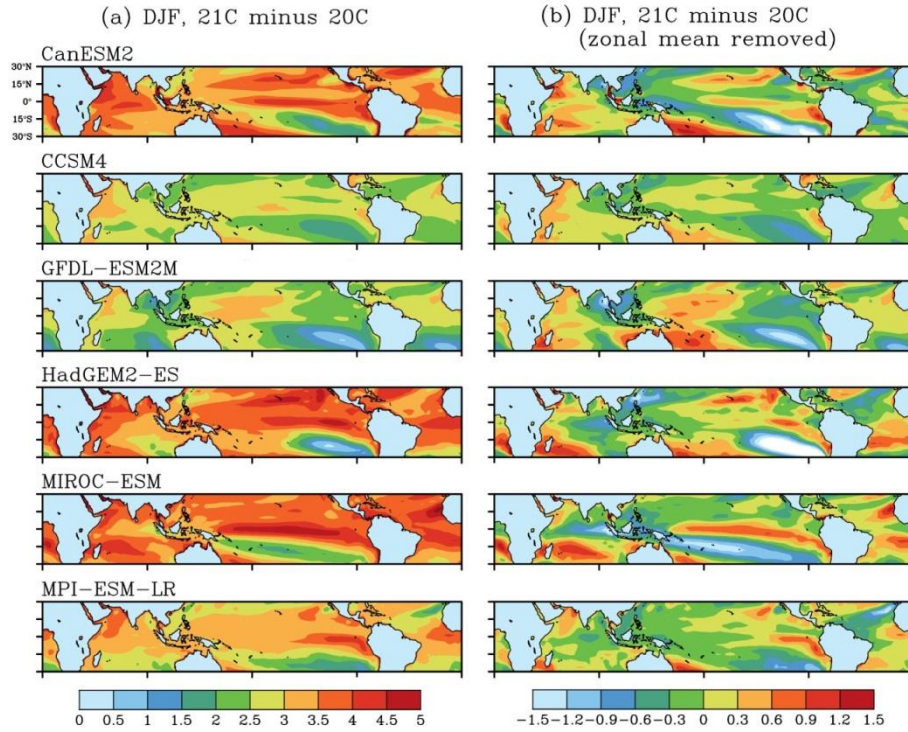
Figure 34: (a) Winter (Dec-Jan-Feb) mean SST of the difference between 20C and 21C (21C minus 20C). (b) As (a) but zonal mean reemoved from (a). Units in °C.

8.2   Atmospheric Angular Momentum response

Since the variability of AAM is contributed mainly by M_R, we focus on M_R only. The index is evaluated as Eq. (4.1). Compared with NCEP R-1 in Fig. 35 (in light blue) and Table 9, the AOGCMs (left panels in Figs. 35a-35e, in dark blue) in 20C simulated well the seasonal cycle of M_R in general, which is maximum in winter to spring, primary minimum in summer, and secondary minimum in winter (Huang and Sardeshmukh 2000). Under the increased radiative forcing, the whole seasonal cycle of M_R shifts up robustly in all the AOGCMs (i.e., differences between red and dark blue lines in left panels in Figs. 35a-35e) and the magnitude of their increases slightly larger in summer than in winter and annual mean: 2.0, 1.8 and 1.9 AMU, respectively. However, the standard deviation in winter is larger than that in summer for most models. The magnitude of the shifts of the AOGCMs is far larger than that in the observed 1976/77 transition, 0.64 and 0.67 AMU for R-1 and 20CR. It is comparable to those in the previous studies under global warming (Rosen and Gutowski 1992, de Viron et al. 2002, Räisänen 2003), and we also confirm that the response is positive in contrast with Rosen and Gutowski (1992).

SSTs taken from AOGCM can be thought to bear the effect of the increased radiative forcing by themselves. AGCMs with the prescribed SSTs of AOGCMs as a lower boundary condition, reproduce the responses of M_R of AOGCMs to the forcing qualitatively similar to the conclusion of Stephenson and Held (1993). The seasonal cycles agree well on those of AOGCMs and R-1, and the amount of increases under forcing is quite comparable to that in AOGCMs : 2.5, 1.3, 1.8 AMU in summer, winter and annual mean, respectively. However, CanESM and MIROC-ESM show small increases of M_R in winter, 0.6 and 0.3 AMU, respectively, even though AOGCMs have

robust increases, 2.0 and 2.1 AMU. CanESM has larger increase in summer to compensate the annual mean but MIROC-ESM does not. The shifts of M_R are more statistically significant than those of AOGCMs since the standard deviation is much smaller than that of AOGCMs.

Table 9: Winter (Dec-Jan-Feb), Summer (Jun-Jul-Aug) and Annual means of M_R of AOGCMs, AGCMs and R-1 in 20C, and $\Delta M_R/\Delta Nino3.4$ for 21C minus 20C. The numbers in the bracket stand for the difference between 20C and 21C (21C minus 20C).

| | M_R | | | | | | $\Delta M_R/\Delta Nino3.4$ | |
| | DJF | | JJA | | Annual | | | |
	AOGCM	AGCM	AOGCM	AGCM	AOGCM	AGCM	AOGCM	AGCM
CanESM2	18.5	16.7	14.1	14.0	16.8	15.7	0.54	0.52
	(+2.0)	(+0.6)	(+1.9)	(+2.9)	(+2.0)	(+2.0)		
CCSM4	15.2	16.4	12.2	13.9	14.2	15.4	0.40	0.45
	(+1.4)	(+1.1)	(+1.0)	(+1.6)	(+1.1)	(+1.3)		
GFDL-	14.8	14.9	12.6	13.1	14.3	14.7	0.57	0.80
ESM2M	(+1.4)	(+2.5)	(+2.0)	(+2.6)	(+1.5)	(+2.1)		
HadGEM2-	15.2	16.2	11.6	13.6	14.2	15.3	0.52	0.52
ES	(+1.8)	(+1.5)	(+2.6)	(+2.8)	(+2.1)	(+2.1)		
MIROC-	15.0	15.8	13.1	14.0	15.0	15.5	0.45	0.23
ESM	(+2.1)	(+0.3)	(+1.8)	(+1.5)	(+1.9)	(+1.0)		
MPI-ESM-	15.2	16.5	12.2	13.5	14.2	15.5	0.77	0.76
LR	(+2.2)	(+1.6)	(+2.9)	(+3.8)	(+2.5)	(+2.5)		
Multi-model	15.6	16.1	12.6	13.7	14.8	15.4	0.54	0.55
mean	(+1.8)	(+1.3)	(+2.0)	(+2.5)	(+1.9)	(+1.8)		
R-1	15.9		11.8		14.5			

Figure 35: Seasonal cycle of M_R for AOGCMs and AGCMs in 20C (blue), 21C (red) and 21C minus 20C (green), and that for R-1 (cyan). Shading stands for 1σ. Units in AMU.

8.3   Zonal-mean zonal wind response

We investigated the atmospheric response of an integrated quantity in the previous section, and will take a closer look at the embedded response of the zonal wind in M_R in this section.

89
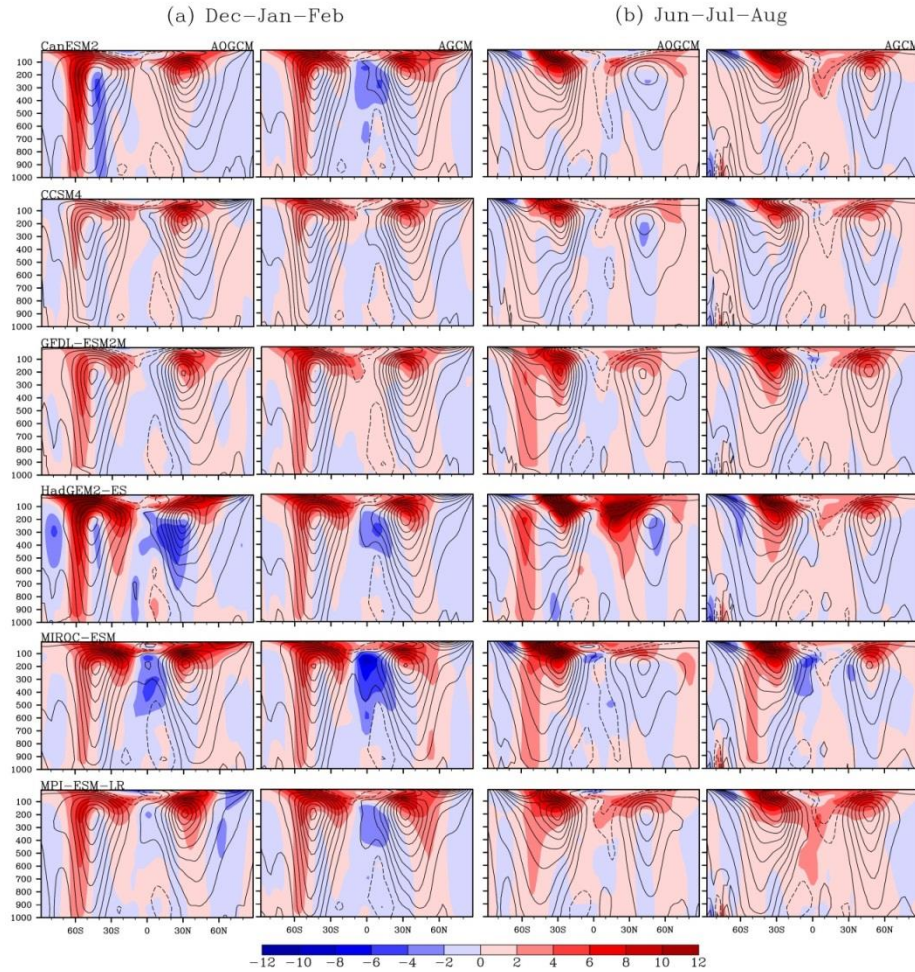
Figure 36: (a) Zonal-mean zonal wind in winter (Dec-Jan-Feb) for AOGCMs and AGCMs in 20C (black contour line) and 21C minus 20C (color contour). (b) As (a) but in summer (Jun-Jul-Aug). Units are in m s^{-1}, contour interval is 5 m s^{-1} with negative values in dash line.

Figure 36 shows the trend, defined as the difference between 20C and 21C (21C minus 20C), of the zonal-mean zonal wind in winter (Dec-Jan-Feb) and summer (Jun-Jul-Aug). Again, AGCMs reproduce well the response of AOGCMs to GHG forcing. The strengthening and poleward shift of the subtropical zonal jets, which is consistent with the trend in Reanalyses (Paek and Huang 2012) and findings on the expansion of the Hadley circulation and poleward shift of the storm tracks (e.g., Yin 2005, Lu et al. 2007),

are agreed between AOGCMs and AGCMs. The increase of MR is related to the increase

in the upper tropospheric zonal wind with maxima at around 30 ˚N, 30 ˚S and 60 ˚S, and

the latter has a tripole pattern in Southern Hemisphere, which is a robust feature in winter

time (Stephenson and Held 1993, Huang et al. 2001). On the other hand, the decreases in

the upper tropospheric zonal wind over the lower latitudes in AGCMs of CanESM2,

MPI-ESM-LR in winter and MIROC-ESM in both winter and summer, result in the

smaller increases of M_R than those of AOGCMs due to the latitudinal weight $\cos^2\theta$ in the

integral for M_R.

$ucos\theta$ at 200 hPa is a good proxy of seasonal cycle of M_R (Huang and

Sardeshmukh 2000). Figure 37 shows good agreements between AOGCMs and AGCMs

qualitatively, and depicts also the three zonal bands with substantial increases in zonal

wind trend clearly. However, the discrepancies between AOGCMs and AGCMs exist

locally and globally. The trend of the weighted zonal wind is much weaker in AGCMs of

CanESM2, MPI-ESM-LR in winter and MIROC-ESM in winter and summer than that in

corresponding AOGCMs, at the equatorial band with a minimum over central/eastern

tropical Pacific, which results in the smaller shift of M_R.

(a) Dec–Jan–Feb
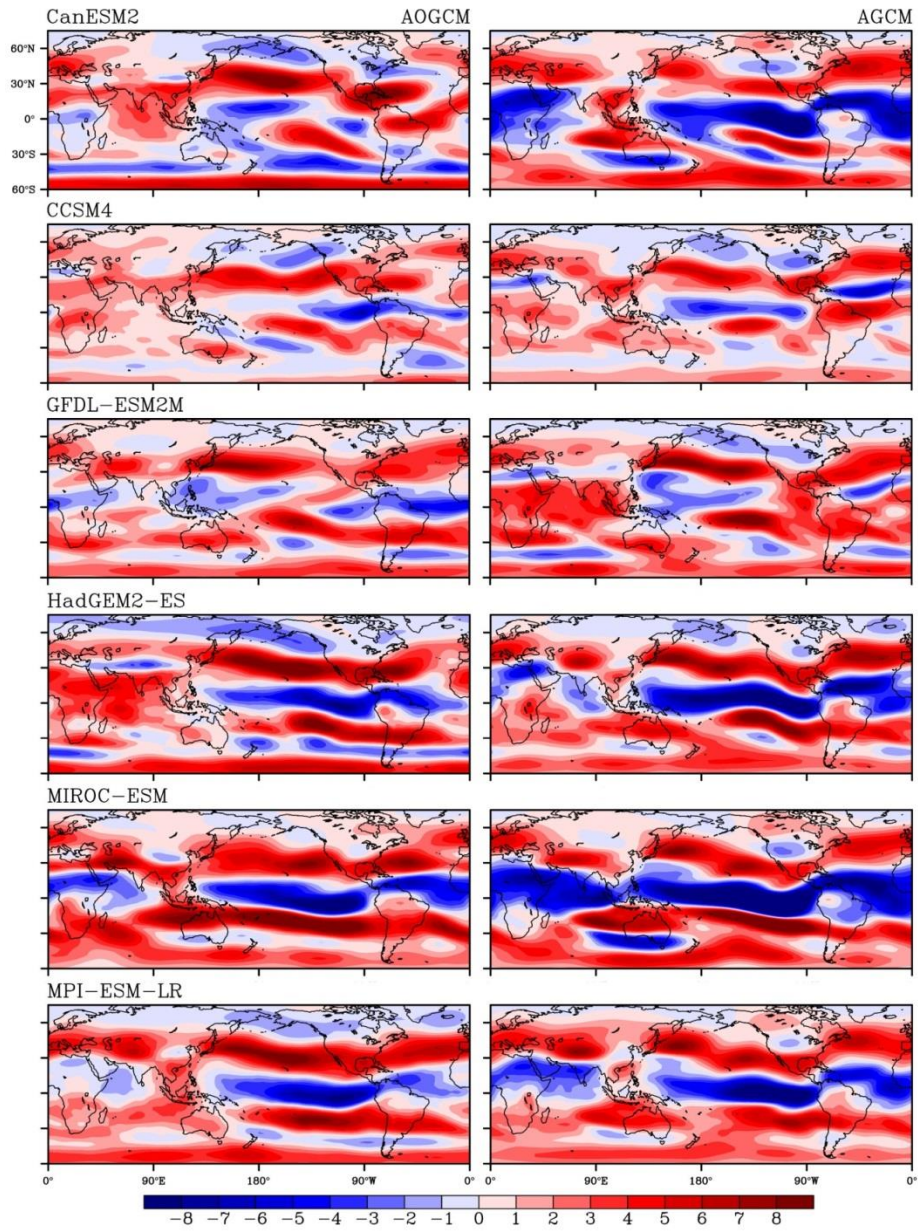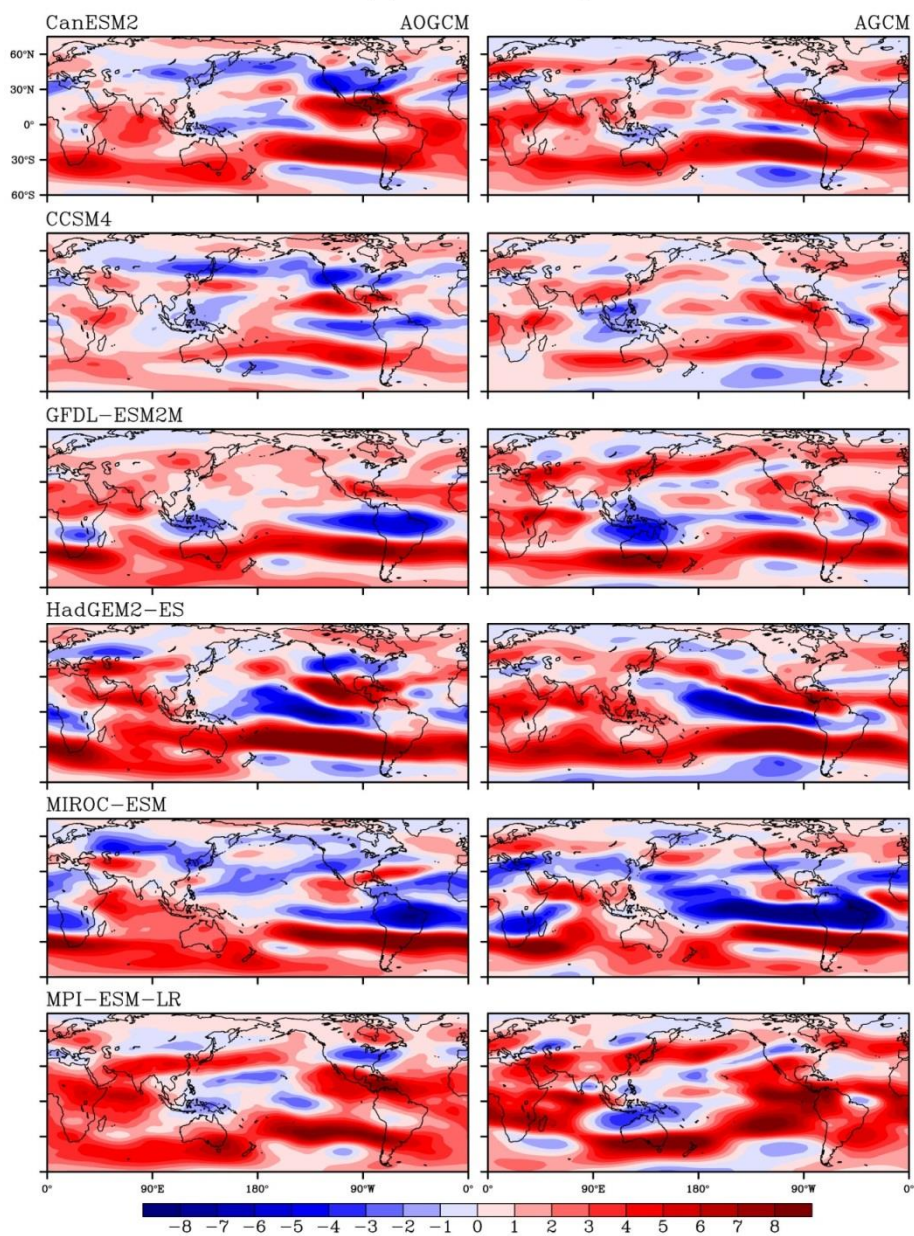
Figure 37: *u cosθ* at 200hPa in winter (Dec-Jan-Feb) for AOGCMs and AGCMs in 21C minus 20C (b) as (a) but in summer (Jun-Jul-Aug). Units are in m s^{-1}.

8.4   Relation between M_R and Tropical SST

In this section, we will move our focus on the relation between the response and SST forcing itself. It is well known that the interannual variability of AAM is highly associated with tropical Pacific SST (e.g., Black et al. 1996, Huang et al. 2003), and AAM has still a good correlation with tropical SST on the longer time scales, including decadal-to-centennial scales in the observations and simulations (e.g., Huang et al. 2001, Räisänen 2003, Paek and Huang 2012). The increased tropical SST under radiative forcing leads to the enhanced subtropical zonal jets by thermal wind balance and increase in M_R, so-called "one-way forcing" (Huang et al. 2004), which is implied in Figs. 34 and 35.

Even though the evolution of AAM and tropical SST are nonlinear in time, the AAM-SST relation is linear on the centennial scale under GHG forcing, and the ratio was suggested as a diagnostic tool (Huang et al. 2001, 2004). For our analysis, we use M_R and Nino3.4 index, defined as the average of the SST anomaly over a box in the equatorial central-eastern Pacific bounded by 120°W-170°W and 5°S-5°N, such that the ratio is $\Delta M_R/\Delta$Nino3.4 (Δ stands for 21C minus 20C). The results are shown in Table 9 and the numbers are close between AOGCMs and AGCMs due to the good reproduction of M_R of AGCMs compared with AOGCMs. It is also interesting that the ratios for AOGCMs ranges in 0.40-0.77 AMU °C^{-1}, for AGCM in 0.23-0.80 AMU °C^{-1}, with both averages of 0.54-0.55 AMU °C^{-1}, which are comparable to the findings in CMIP2 multi-models of Räisänen (2003).

We have focused on the centennial timescale in this study, however, Fig. 34b (except GFDL-ESM2M) which resembles qualitatively tropical SST anomaly of a dipole

94

pattern with the two off-equator maxima in 1976/77 regime shift, which has been reproduced in AGCMs forced by the observed SST (e.g., Huang et al. 2005), suggests that this experimental approach may be useful to understand the 1976-like interdecadal oscillations if the substantial increase of MR accompanied by the increased equatorial SST with a dipole pattern in central/ eastern Pacific are found from AOGCMs such as CMIP3/5 models.

8.5   Conclusion

We have conducted a pair of repeated seasonal cycle experiments using CAM 3.1 (AGCM) forced by the prescribed SSTs constructed from the means of the last 20 years of 20th and 21st centuries from the six CMIP5 simulations (AOGCM). The atmospheric response of the AGCM simulations to SST forcing was compared with that of the AOGCMs.

The key result of this study is that the global atmospheric response of AOGCMs to increased radiative forcing seems to be reproduced by the AGCMs using prescribed SSTs of the AOGCMs, qualitatively and quantitatively as illustrated in Fig. 35 and 36, confirming SST as a lower boundary condition plays an important role in regulating the global atmospheric changes (Stephenson and Held 1993).

Under global warming scenario, the atmospheric angular momentum of all AOGCMs is projected to shift up considerably in all seasons with larger increases in winter than in summer on the centennial timescale accompanied by the increases in SSTs. The amplitudes are comparable to the previous studies under doubled CO_2 concentration. The similar magnitude of increase in M_R of AOGCM is found from most of the AGCMs

forced by SSTs of the AOGCM. However, some AOGCMs show the relatively small increases in M_R in winter and summer.

The analysis of the zonal-mean zonal wind and weighted zonal wind at 200 hPa highlighted the strengthening of zonal wind with three maxima around 30 °N, 30 °S and 60 °S. The distinct tripole pattern is found in the Southern Hemisphere in winter, which has been presented in the observations and simulations under GHG forcing. This analysis also revealed that the underestimated M_R in some AGCMs comes from the mis-represented details of the zonal wind locally and globally, especially larger decrease in zonal wind at the equatorial band in the AGCMs than that in the AOGCMs.

To diagnose the atmospheric response to tropical SST, the sensitive parameters ($\Delta M_R/\Delta Nino3.4$) are evaluated. The range of the AGCMs is close to that of the AOGCMs due to similar magnitude of increase in M_R. The ratios are also comparable to those in CMIP2 models.

Chapter 9

9   SIMULATIONS: ANNUAL-TO-DECADAL PREDICTABILITY IN CMIP5

DECADAL SIMULATIONS

With increasing interest in the climate change in the near term, which is 10-30yr

referred to the "decadal" time scale among policy makers and climate researchers. The

previous research has mostly focused on the long-term climate projections and the short-

term predictions. The former such as CMIP5 centennial simulations is regarded as

"boundary condition problem" seeking the climate trend under the specified forcing. On

the other hand, the latter such as daily weather forecast and ENSO forecast is considered

as "initial value problem" for which the oceanic initial conditions are more important

(Meehl et al. 2009). The decadal predictions are a scientific challenge to fill the gap

between the short-term predictions and long-term projections (see Fig. 38).
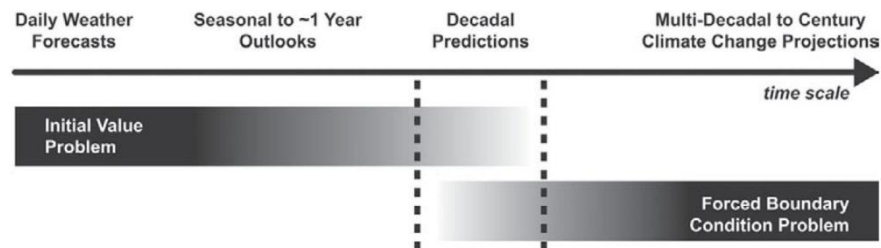
Figure 38: Schematic illustrating progression from initial value problems with daily weather forecasts at one end, and multidecadal to century projections as a forced boundary condition problem at the other, with seasonal and decadal prediction in between (Meehl et al. 2009).

For the social and scientific needs, the CMIP5 have newly introduced "Decadal

simulations" in state-of-the-art AOGCM simulations initialized with the observations

97

from 1960 to present (Taylor et al. 2012). In parallel, the decadal predictive skill has recently been studied independently of CMIP activity   (e.g., Keenlyside et al. 2008, van Oldenborg et al. 2012).

In this background, we will investigate the decadal predictive skill using CMIP5 Decadal simulations with multiple models. For this purpose, we choose global atmospheric angular momentum (AAM) associated with the location and strength of the upper atmosphere and Nino3.4 SST with a higher correlation with AAM on the wide range of timescales. In addition, a good agreement of decadal oscillations of AAM and Nino3.4 among the multiple reanalysis and reconstructed SST datasets is found (Paek and Huang 2012a, 2012b).

9.1   Datasets and analysis method

The decadal simulations of the 13 CMIP5 models (Taylor et al. 2012) from 1960 to 2010 (starting year 1960 to 2000) in Table 10 are used for this study. For model validation, NCEP/NCAR Reanalysis dataset (R-1) for atmosphere and Hadley Centre Sea Ice and Sea Surface Temperature dataset (HadISST) for ocean are used.

For the climate index, we will use the globally integrated atmospheric angular momentum (AAM) and Nino 3.4 SST Index for atmosphere and ocean component, respectively. The AAM consists of two components: relative angular momentum (M_R) associated with the location and strength of zonal wind and omega angular momentum (M_Ω) with the atmospheric mass distribution. Since the variability of AAM is mainly contributed by M_R (Huang and Sardeshmukh 2000), we focus on M_R only and the index is evaluated as Eq. (4-1). Some models have a finer vertical resolution in the stratosphere,

98

we integrate up to 10 hPa as an upper level for all models for a fair comparison. The inclusion of the data above 10 hPa does not affect our conclusions.

Table 10: The CMIP5 models and their ensemble members used in Chapter 9.

No.	Model	#ensemble	Resolution (Atmosphere; Ocean)
1	BCC-CSM1.1	4	2.8 °L26; 1 °×1-1/3 °L40
2	CanCM4	10	1.9 °L35; 1.4 °×0.94 °L40
3	CFSv2	4	0.9 °L64; 0.25 °-0.5 °L40
4	CNRM-CM5	10	1.4 °L31; 1 °L42
5	FGOALS-s2	3	2.8 °×1.66 °L26; 0.5 °-1 °L30
6	GFDL-CM2p1	10	2.5 °×2 °L24; 1 °L50
7	HadCM3	10	3.75 °×2.75 °L19; 1.25 °L20
8	IPSL-CM5A-LR	6	3.75 °×1.9 °L39; 2 °L31
9	MIROC4h	3	0.6 °L56; 0.28 °×0.2 °L48
10	MIROC5	6	1.4 °L40; 1.4 °×0.8 °L50
11	MPI-ESM-LR	10	1.9 °L47; 1.5 °L40
12	MPI-ESM-MR	3	1.9 °L47; 1.5 °L40
13	MRI-CGCM3	9	1.12 °L48; 1 °×0.5 °L51

To quantify the predictive skill, the root mean squared error (RMSE) and anomaly correlation coefficient (ACC) are used as :

$$ACC(\tau) = \frac{\sum_{j=1}^{n}(X'_{j\tau})(O'_{j\tau})}{\sqrt{\sum_{j=1}^{n}(X'_{j\tau})^2 \sum_{j=1}^{n}(O'_{j\tau})^2}} ,\qquad (9\text{-}1)$$

where, *X* represents a climate index such as AAM and Nino3.4 from model simulations, $X'_{j\tau}$ is the anomalies defined as the prediction removing the decadal average (Note that the discrepancies among different Reanalysis datasets come mainly from long-term mean and long-term trend in Paek and Huang (2012).), τ is the forecast lead time, *j* is the starting year. *O* represents that from observations similarly.

9.2   Atmospheric angular momentum

In order to investigate predictive skill on the annual timescale, we analyze the annual mean of the atmospheric angular momentum. Figures 39b-39n are the annual-mean anomalies of M_R (ΔM_R, Δ stands for anomaly) from the ensemble mean of individual models, and Fig 39a is that of multi-model mean, superimposed with that from the observations. In general, the differences between the individual models and observations are small for the 1st year, but the discrepancies increase sharply from the 2nd year accompanied by the increasing ensemble spread in lead time. In some models such as CFSv2, FGOALS-s2 and others, the discrepancies between predictions starting in year 1960 and observations are found to be large even in the 1st year lead time. It might be due to the scarce oceanic observations in early years leading to the different state of atmospheric observations. It is rarely seen in the later years. For the multi-model mean, it holds the similar trend to the individual models. The predictions start close to the observed values in the 1st year and drift to the model climatology from the 2nd year.

For the decadal predictability, we take the 4-year running average of the time series of ΔM_R. Figure 40 is similar to Figs. 39 but for the decadal time series. Compared with the annual timescale, Fig. 40 shows that the discrepancies between forecasts and observations are still large even though the time series is smoothed. Even the 1st year predictive skill in Fig. 39 is not observed since the larger discrepancies between the predictions and observations from the 2nd year in annual time series degrade the decadal predictive skill.
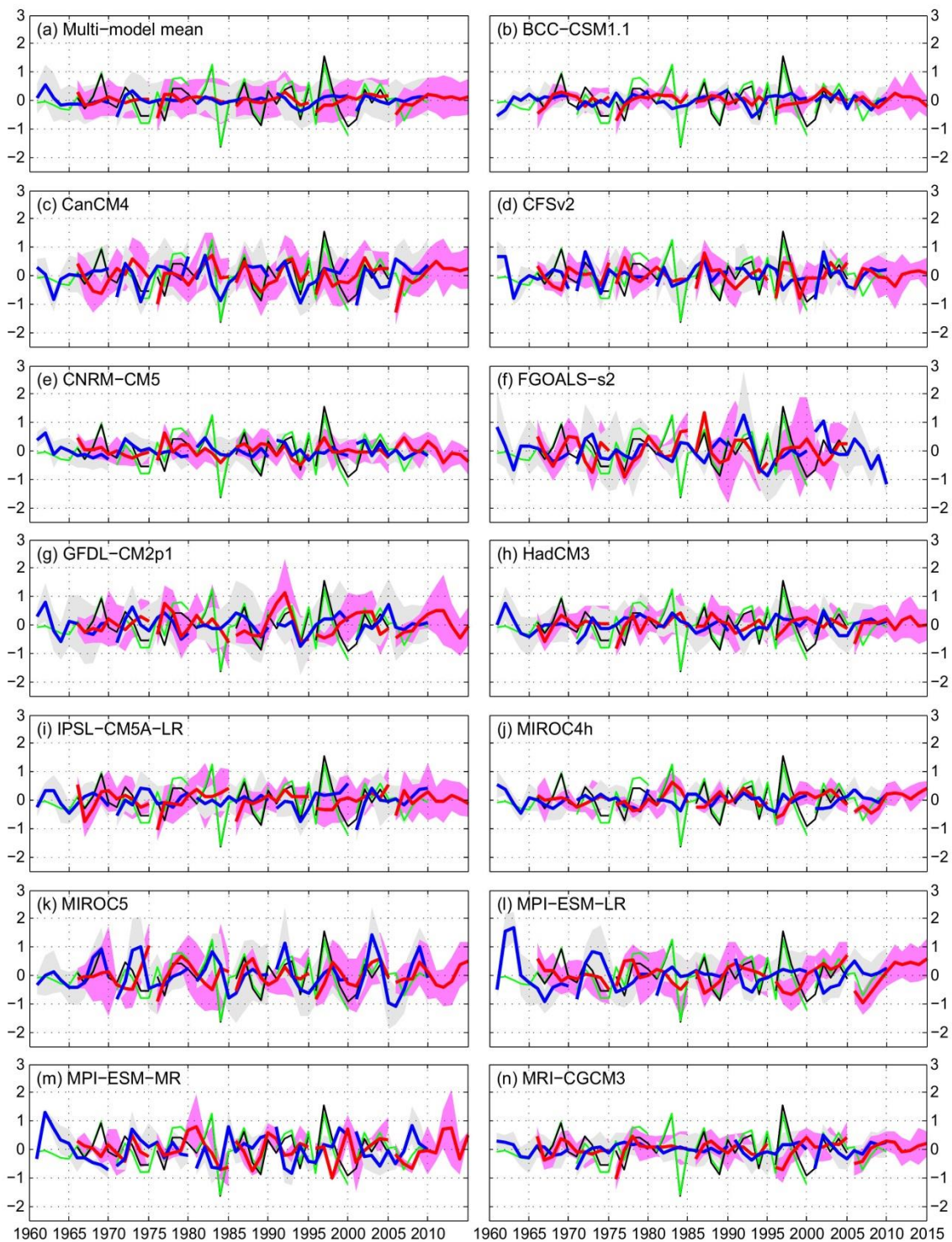
Figure 39: Annual mean AAM anomaly (ΔM_R) for NCEP R-1 (green and black) and Decadal runs of CMIP5 multi-models (blue and red). Shading stands for 1σ. Units in AMU.
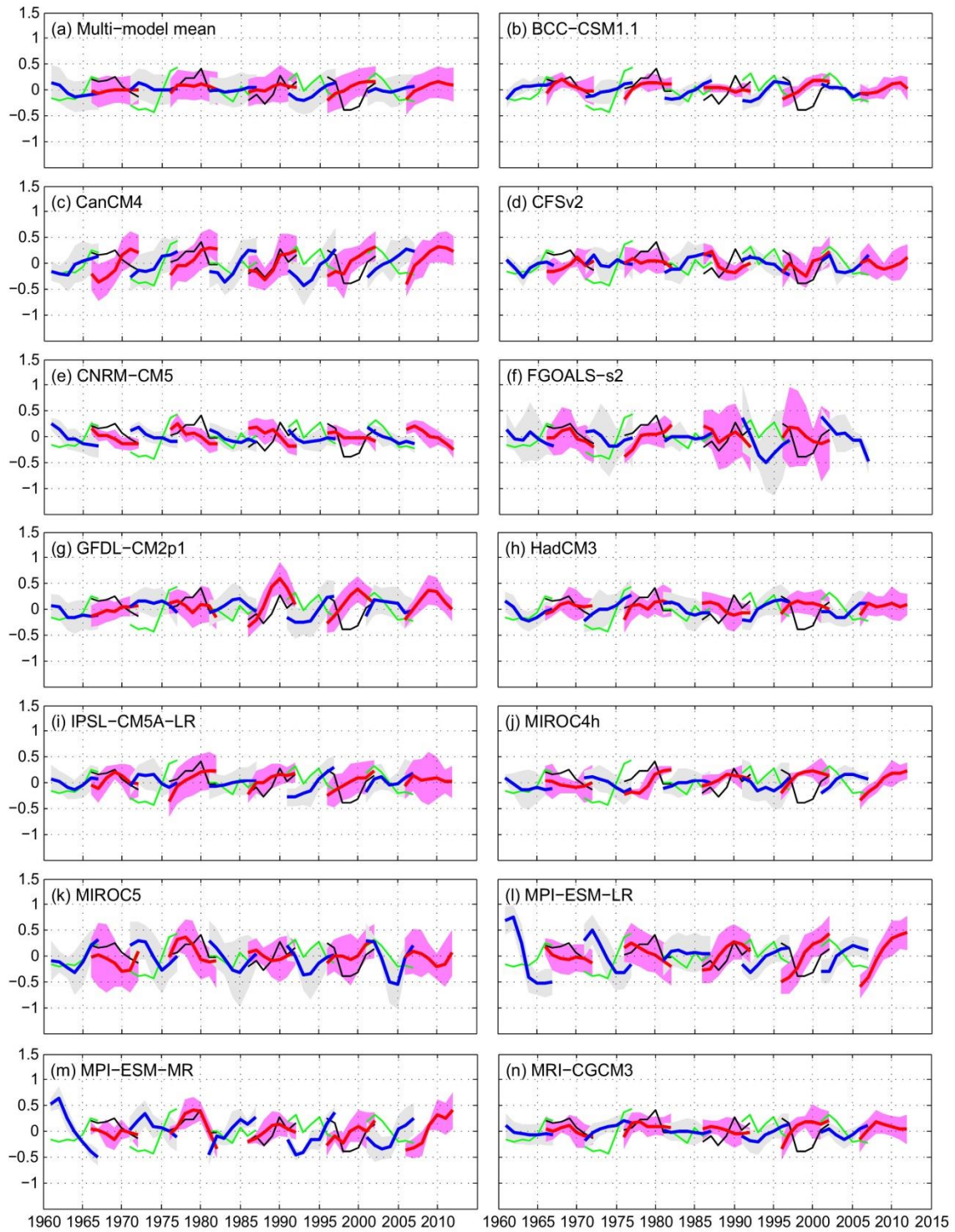
Figure 40: As Fig. 39 but for the decadal variability.
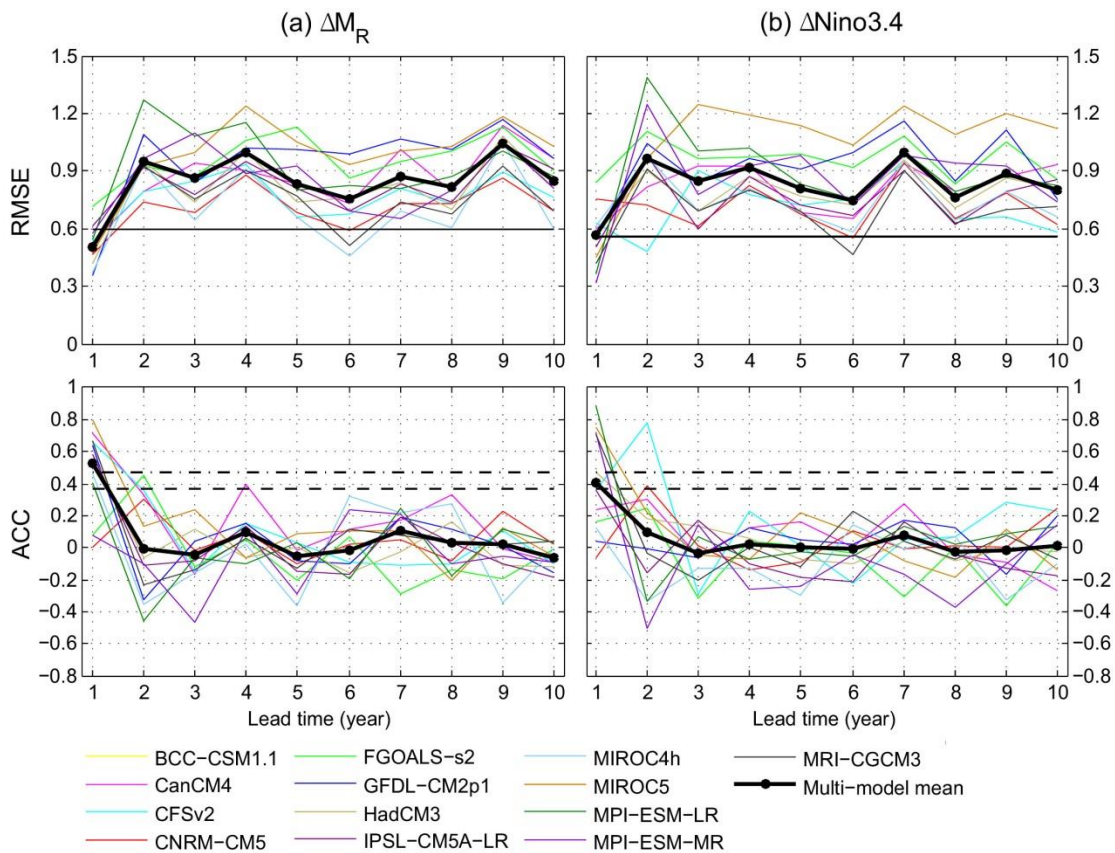
Figure 41: (a) Root mean squared error (RMSE) (top) and Anomaly Correlation Coefficient (ACC) (bottom) of ΔM_R during 1960-2010 between CMIP5 decadal individual models and Reanalysis-I for forecast lead years. Thin black solid line is the observed standard deviation. (b) As (a) but for ΔNino3.4 Index between CMIP5 models and HadISST. Dashed and Dash-dotted lines are 90% and 95% confidence levels, respectively.

To quantify the predictive skill, RMSE and ACC are evaluated for individual models and the multi-model mean as Figs. 41a and 42a. The figures highlight that the RMSE (ACC) substantially rises (drops) from the 2nd lead year with the 1st forecast skill on the annual timescale (Fig. 41a) while there is no predictive skill on the decadal timescale (Fig. 42a; far below the significant level over the whole lead years). This trend holds for both individual models and multi-model mean.

The models with a finer resolution such as CFSv2, CNRM-CM5, MIROC4h and MRI-CGCM3 do not outperform the forecast skill of the others. The multi-model mean does not outperform individual model, either.
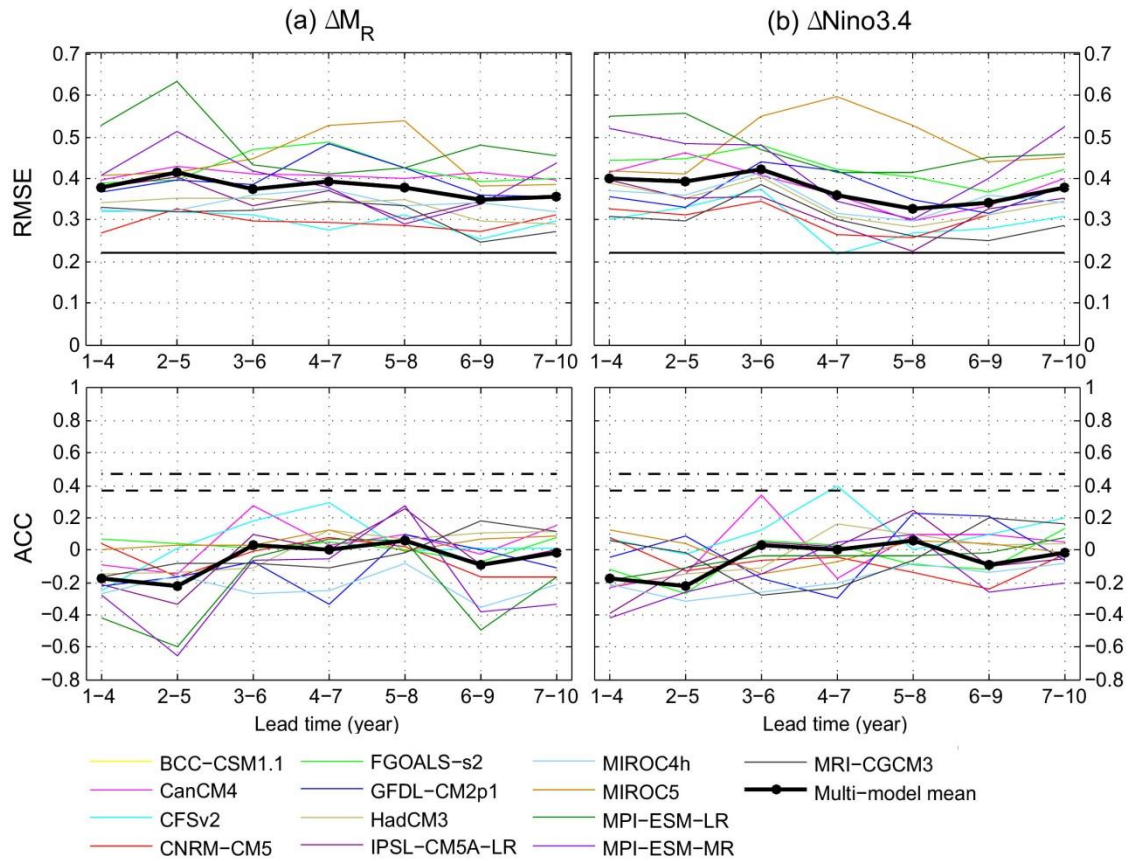
Figure 42: As Fig. 41 but for the decadal variability

9.3   Zonal mean zonal wind

Since the M_R is a globally integrated quantity, we will investigate the weighted zonal mean zonal wind ($u\cos\theta$), which is proportional to M_R in order to see the local predictive skill. Only the vertical level at 200 hPa is considered for a good proxy of M_R (Huang and Sardeshmukh 2000).

Figures 43a-43n are the ACC of annual mean 200 hPa zonal wind anomaly ($\Delta u\cos\theta$) between CMIP5 decadal runs and Reanalysis-I in the 1st lead year for individual models and multi-model mean. For the individual models, the ACC are different among models. However, they commonly show that the ACC is the maxima over the central and eastern Pacific near the equator. Many models also have positive ACC over the western Pacific (or warm pool region). The high ACC is located as the 3 bands at near the equator and at the midlatitudinal zonal jets at both Hemispheres. Some models also shows the another hemispheric symmetric bands of high ACC for the high latitudinal zonal winds. Compared with the Pacific, the ACC at the Indian and Atlantic basins are lower for the 1st predictive skill. For the multi-model mean, it clearly shows the three zonal bands with the high ACC over the central and eastern Pacific, and also positive ACC at the western Pacific.

Figures 44a-44n are similar to the counterpart in Figs. 43a-44n but for the average of the 1st 4 years on the decadal timescale. Compared with those on the annual timescale, the regions with high or positive ACC are mostly disappeared by the inclusion of predictions in 2-4years for both individual models and multi-model mean.
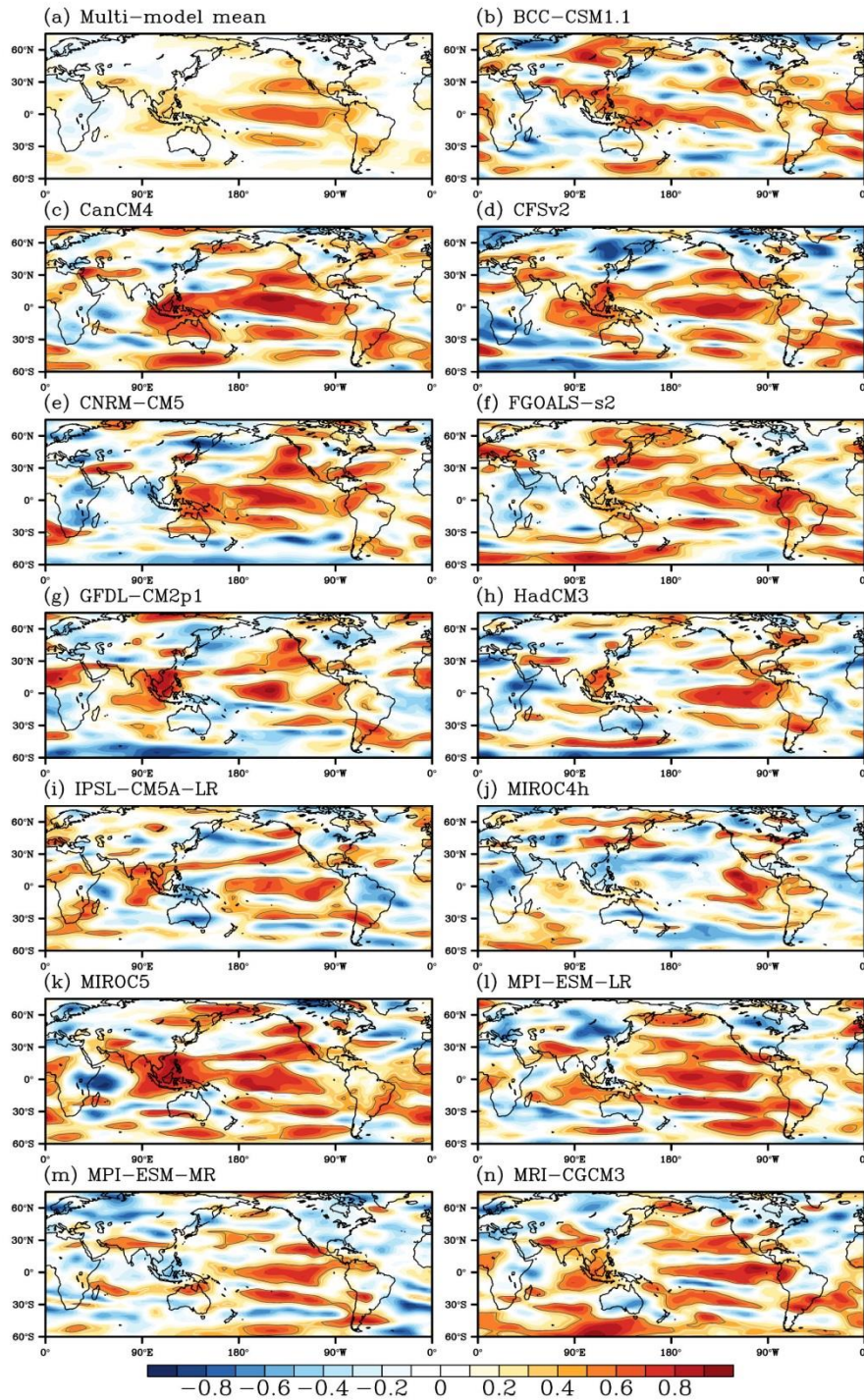
Figure 43: Correlation coefficient of annual mean 200 hPa zonal wind anomaly (Δ ucosθ) between CMIP5 decadal runs and Reanalysis-I for forecast year 1 (Year01). 95% significance level in solid gray line.

(a) Multi−model mean (b) BCC−CSM1.1

(c) CanCM4 (d) CFSv2

(e) CNRM−CM5 (f) FGOALS−s2

(g) GFDL−CM2p1 (h) HadCM3

(i) IPSL−CM5A−LR (j) MIROC4h

(k) MIROC5 (l) MPI−ESM−LR

(m) MPI−ESM−MR (n) MRI−CGCM3

−0.8 −0.6 −0.4 −0.2 0 0.2 0.4 0.6 0.8
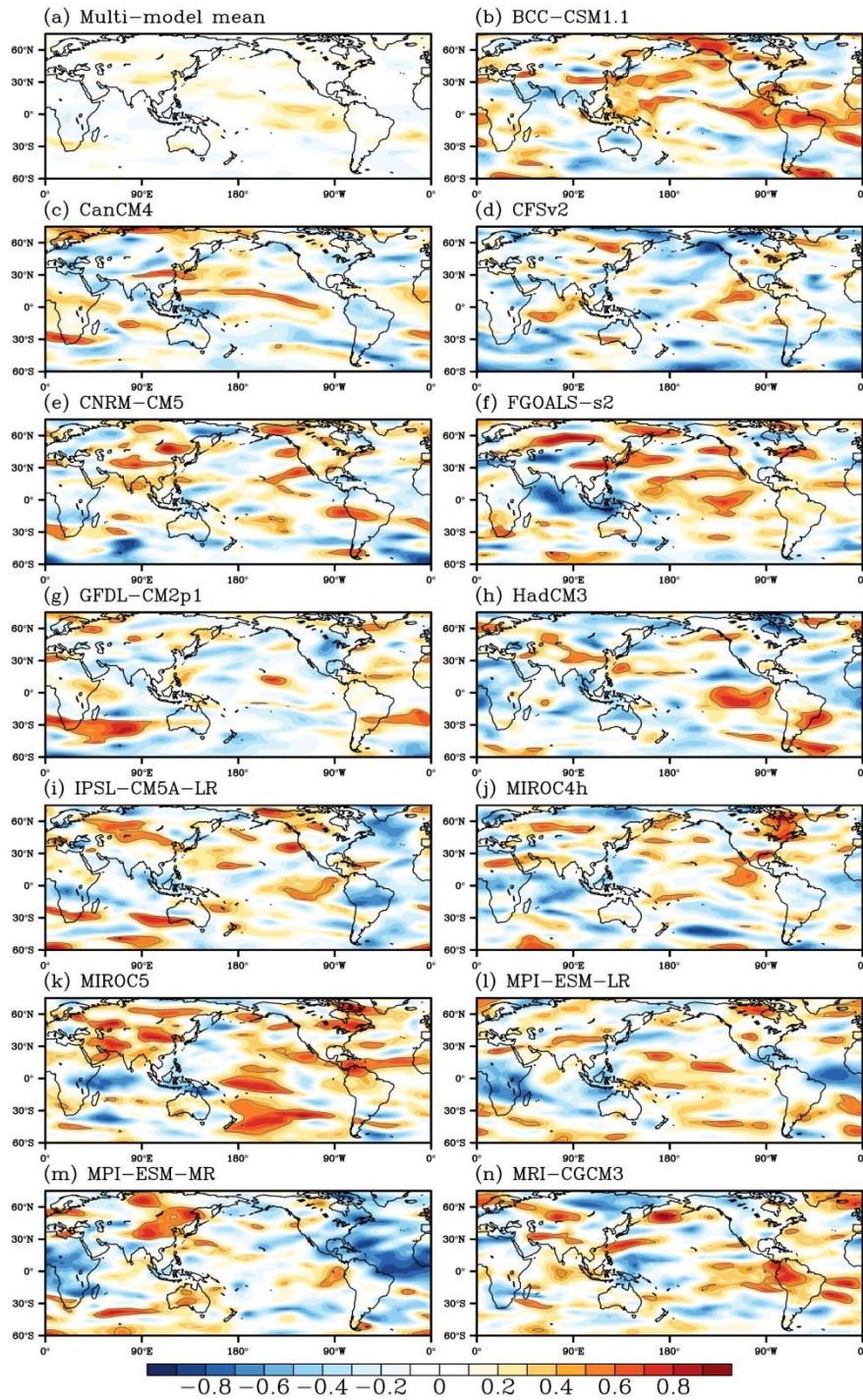
Figure 44: As Fig. 43 but for year 1-4 average (Year01-04).

107

9.4   Tropical SST

The similar analysis to Sec. 9.2 has been done to investigate the forecast skill for the tropical SST since AAM has a good relation to Nino3.4 on the wide ranges of timescales (see survey in Paek and Huang (2012a)). Figures 44 and 45 are similar to Figs. 39 and 40 but for the Nino3.4 Index. The figures show that time series of ΔNino3.4 are highly correlated with the counterpart ΔM_R with the ratio of $\Delta M_R / \Delta$Nino3.4 ≈ 1 AMU $°C^{-1}$ (Huang et al. 2003). The predictive behavior of the individual models and the multi-model mean is very similar to that of ΔM_R with the 1st year predictive skill on the annual timescale and no skill on the decadal timescale. Furthermore, the large discrepancies in the 1st lead year initialized in year 1960, support that the initial conditions of the ocean states result in the discrepancies of ΔM_R. The RMSE and ACC in Figs. 41b and 42b are also similar to the counterpart of ΔM_R in Figs. 41a and 42b.

These results of one year predictive skill are consistent with the ENSO forecast for 9 month at most (e.g., Penland and Sardeshmukh 1995), which also imply the low forecast skill on the longer timescales. The decadal forecast skill is also consistent with the recent findings of the low decadal forecast skill of Pacific SST (van Oldenborgh et al. 2012, Kim et al. 2012, Newman et al. 2013). On the other hand, the skillful decadal prediction was found in the Atlantic oceans (e.g, Keenlyside et al. 2008, Kim et al. 2012).
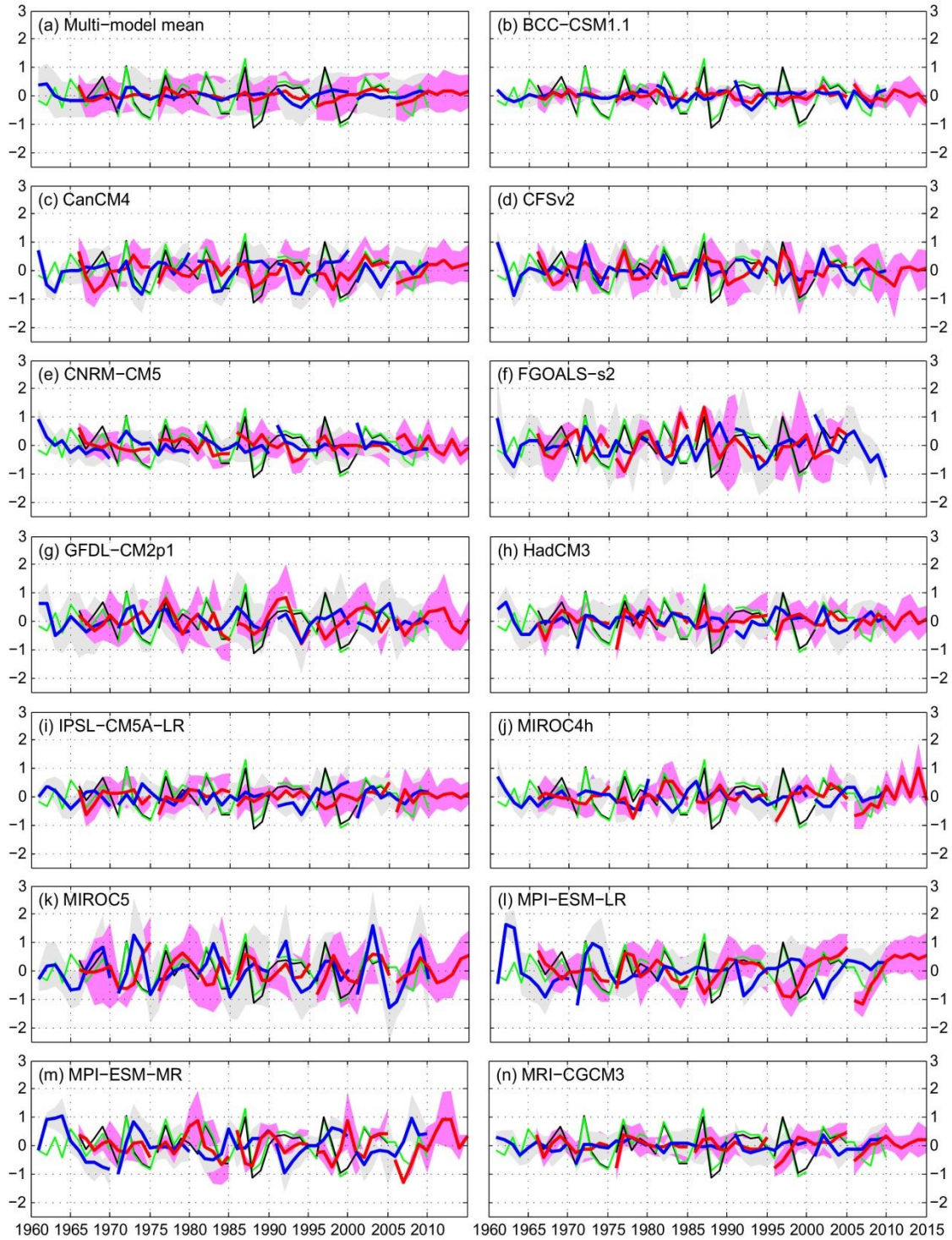
Figure 45: As Fig. 39 but for annual mean SST anomaly in the Nino3.4 region (ΔNino3.4) of HadISST and CMIP5 Decadal runs. Units in °C.
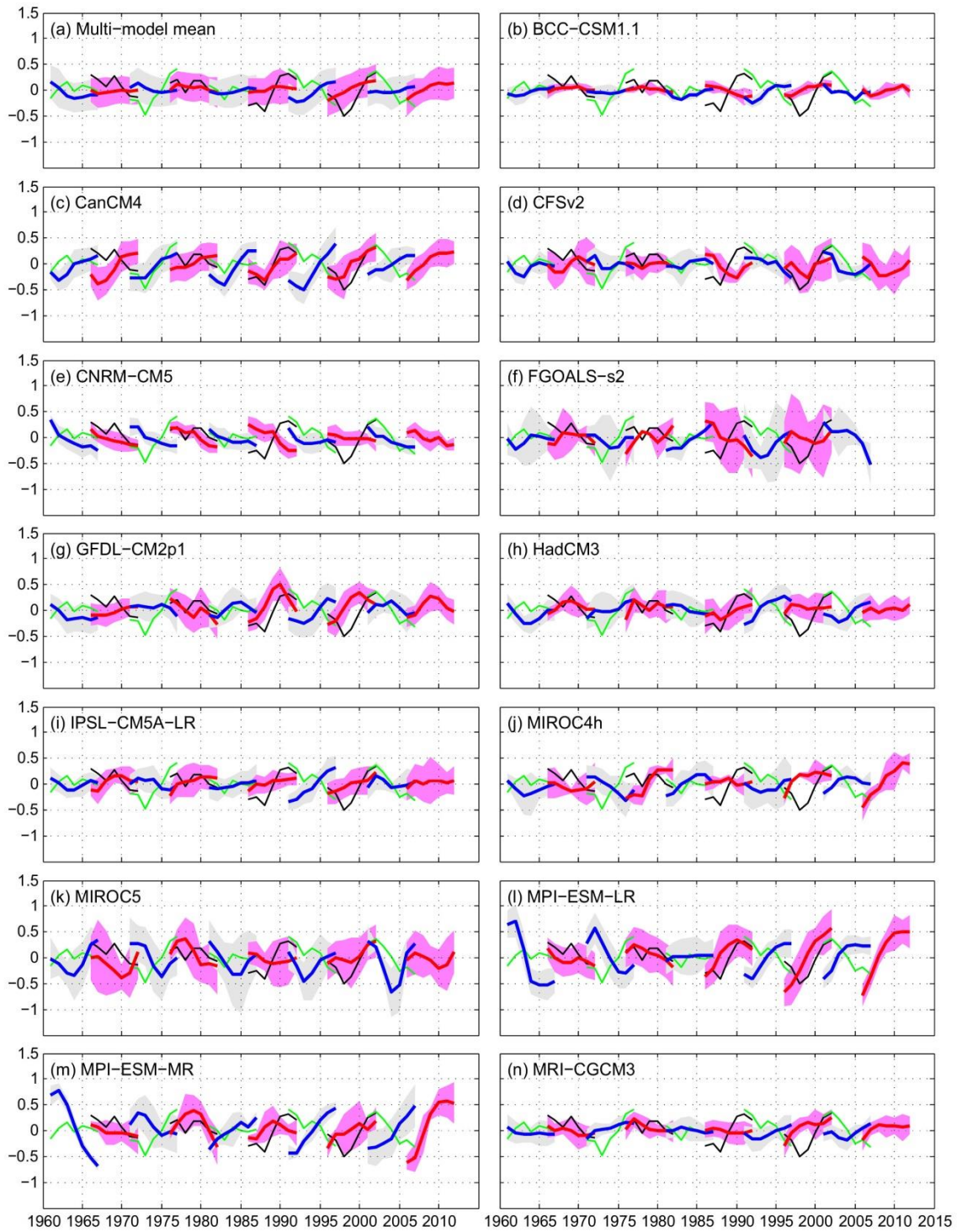
Figure 46: As Fig. 45 but for the decadal variability.

9.5   Conclusion

The CMIP5 decadal simulations of the 13 state-of-the-art models are analyzed using AAM and tropical SST for a climate index, RMSE and ACC for a quantifying metric. They are validated by the reanalysis and reconstructed SST.

On the annual timescale, the 1st year predictive skill was found and the skill drops substantially from the 2nd year. It is consistent with the short-term forecast such as ENSO events (e.g., Penland and Sardeshmukh 1995) even though the CMIP5 Decadal simulations are designed for the decadal prediction. Neither resolution dependency nor ensemble dependency are not clearly observed for the forecast skill. The discrepancies of ΔM_R and ΔNino3.4 between the predictions and observations in 1960 suggested that the uncertainly in the oceanic initial conditions led to the wrong predictions of the atmospheric component even in the 1st year.

On the decadal timescale, the predictive skill was never found in any lead time as it is expected from 1 year skill on the annual timescale. This is consistent with the findings of low predictive skill in Pacific SST. On the other hand, the decadal prediction is skillful in the Atlantic Ocean (e.g, Keenlyside et al. 2008, Kim et al. 2012) implying that more improvements in the models should be done for the Pacific Ocean.

Chapter 10

10   SUMMARY

This study performed the intercomparison of the climate variability and trend on the different timescales ranging from interannual to centenniel, using the reanalysis, the Coupled Model Intercomparison Project (CMIP) simulations and AGCM simulations. The dynamic variables of zonal-mean zonal wind and globally integrated atmospheric angular momentum (AAM) were used for the analysis.

For the observations, the validation of AAM of reanalyses with the independently measured length-of-day (LOD) on the interannual scales revealed a good agreement among almost all reanalyses but a relatively lower correlation of the AAM of the 20th Century Reanalysis (20CR) and LOD. This is related to the absence of coherent low-frequency variability, notably the Quasi-biennial oscillation (QBO), in the stratospheric zonal wind. A good agreement of M_R (wind component of AAM) was found on decadal-to-multidecadal variability among multiple reanalyses, including 20CR which assimilated only the surface pressure, for the second half of the 20th century. The most significant discrepancies among them are in the long-term mean and long-term trend. This indicates that 20CR can be reliably used for the analysis of decadal-to-interdecadal variability in the pre-1950 era with properly detrending. Based on the timeseries of M_R from the entire record of 20CR, the increase in M_R during the 1976/77 climate shift event is found to be the sharpest over the period from 1871-2008.

For the climate model simulations, the centennial climatology and trend of AAM for the 20th and 21st century from the CMIP3 and CMIP5 simulations are diagnosed and validated with 20CR. It is found that CMIP5 models produced a significantly smaller bias

and a narrower ensemble spread of the climatology and trend in the 20th century for both M_R and M_Ω compared to CMIP3, while CMIP3 and CMIP5 simulations consistently produced a positive trend in M_R and M_Ω for the 20th and 21st century with much greater trend in M_R than M_Ω. Both CMIP3 and CMIP5 models produced a wide range of the magnitudes of decadal and interdecadal variability of M_R compared to observation. For those quantities, the ensemble means of CMIP3 and CMIP5 are not statistically distinguishable for either the 20th- or 21st-century runs. The 21st-century simulations from both CMIP3 and CMIP5 produced only a small trend in the amplitude of decadal or interdecadal variability which is not yet statistically significant. This indicates that while the increase in greenhouse gas (GHG) induces an upward trend in AAM, it does not significantly affect its decadal-to-interdecadal variability in the 21st century.

To understand the relation between the dynamic response of the atmosphere to GHG forcing, the atmospheric general circulation model (AGCM) simulations forced by prescribed SST and sea ice concentration taken from CMIP5 simulations were carried out. The increase in AAM and zonal wind trend of the CMIP5 simulations to increased radiative forcing (due to GHG) are reproduced by the AGCM simulations, qualitatively and quantitatively. This confirms SST as an important mediator in regulating the global atmospheric changes under GHG forcing.

The predictive skill quantified using AAM and tropical SST in CMIP5 Decadal simulations. The 1st year predictive skill was found associated with the ENSO events, but no skill on the timescale more than a year even though the simulations are designed for decadal prediction.

113

In summary, we quantified the uncertainty in the reanalyses and CMIP simulations using major climate indices. We found that CMIP5 models have been improved substantially from CMIP3, reduced the uncertainty in the simulations compared with the uncertainty in the observations. However, there is still larger bias in CMIP5 compared with the uncertainty in the observations implying a room for further improvement in CMIP5. It should also be cautious using multi-model mean for policy decision for planning.

REFERENCES

Abarca del Rio, R., 1999: The influence of global warming in Earth rotation speed, *Ann. Geophys.*, **17**, 806-811

Abarca del Rio, R., D. Gambis, and D. A. Salstein, 2000: Interannual signals in length of day and atmospheric angular momentum. *Ann. Geophys.*, **18**, 347–364.

Alexander, M. A., I. Bladé, M. Newman, J. R. Lanzante, N.-C. Lau, J. D. Scott, 2002: The Atmospheric Bridge: The Influence of ENSO Teleconnections on Air–Sea Interaction over the Global Oceans. *J. Climate*, **15**, 2205–2231.

Alexander, M. A., R. Tomas, C. Deser, D. M. Lawrence, 2010: The Atmospheric Response to Projected Terrestrial Snow Changes in the Late Twenty-First Century. *J. Climate*, **23**, 6430–6437.

Allen, R. J., and S. C. Sherwood, 2008: Warming maximum in the tropical upper troposphere deduced from thermal winds, *Nature Geosci.*, **1**, 399-402

Arakawa, A., 2004: The cumulus parameterization problem: Past, present, and future. *Journal of Climate*, **17(13)**, 2493-2525.

Baldwin, M. P., and T. J. Dunkerton, 1999: Propagation of the Arctic Oscillation from the stratosphere to the troposphere, *J. Geophys. Res.*, **104**, 30937-30946

Black, R. X., D. A. Salstein, and R. D. Rosen, 1996: Interannual modes of variability in atmospheric angular momentum, *J. Climate*, **9**, 2834-2849.

Bryan, K., 1969: A numerical method for the study of the circulation of the World Ocean. *Journal of Computational Physics*, **4**, 347-376.

Cai, W., A. Sullivan, and T. Cowan, 2009: Rainfall teleconnections with Indo-Pacific variability in the WCRP CMIP3 Models, *J. Climate*, **22**, 5046-5071.

Chao, B. F., 1989: Length-of-day variations caused by El Nino Southern Oscillation and Quasi-biennial Oscillation, *Science*, **243**, 923-925

Collins, W. D., and Coauthors, 2006: The Community Climate System Model version 3 (CCSM3). *J. Climate*, **19**, 2122–2143.

Compo, G. P., J. S. Whitaker, and P. D. Sardeshmukh, 2006: Feasibility of a 100 year reanalysis using only surface pressure data, *Bull. Amer. Meteor. Soc.*, **87**, 175-190

Compo, G., and P. Sardeshmukh, 2009: Oceanic influence on recent continental warming, *Clim. Dyn.*, **32**, 333–342, doi:10.1007/s00382-008-0448-9.

Compo, G. P., J. S. Whitaker, P.D. Sardeshmukh, and coauthors, 2011: The Twentieth Century Reanalysis Project. Quart. *J. Roy. Meteorol. Soc.*, **137**, 1-28.

Covey, C., K. M. AchutaRao, U. Cubasch, P. Jones, S. J. Lambert, M. E. Mann, T. J. Phillips, and K. E. Taylor, 2003: An overview of results from the Coupled Model Intercomparison Project. *Global Planet. Change*, **37**, 103–133

Cox, M. D., 1970: A mathematical model of the Indian Ocean, *Deep-Sea Research*, **17**, 47-75.

Cox, C. M., and B. F. Chao, 2002: Detection of a large-scale mass redistribution in the terrestrial system since 1998. *Science*, **297**, 831–833.

Courtier P., Thepaut J-N, Hollingsworth A., 1994: A strategy foroperational implementation of 4D-Var, using an incremental approach. *Q. J. R. Meteorol. Soc.* **120**: 1367–1388.

Courtier P., Andersson E., Heckley W., Pailleux J., Vasiljevic D., Hamrud M., Hollingsworth A., Rabier F., Fisher M., 1998: The ECMWF implementation of three-dimensional variational assimilation (3DVar). I: Formulation. *Q. J. R. Meteorol. Soc.* **124**, 1783–1807.

Dee, D. P., E. Källén, A. J. Simmons, and L. Haimberger, 2011: Comments on "Reanalyses suitable for characterizing long-term trends." *Bull. Amer. Meteor. Soc.*, **72**, 65–70.

Dee, D. P., and coauthors, 2011: The ERA-Interim reanalysis: configuration and performance of the data assimilation system, *Q. J. R. Meteor. Soc.*, **137**, 553-597.

Deser, C., A. S. Phillips, 2009: Atmospheric Circulation Trends, 1950–2000: The Relative Roles of Sea Surface Temperature Forcing and Direct Atmospheric Radiative Forcing. *J. Climate*, **22**, 396–413.

de Viron, O., V. Dehant, H. Goosse, and M. Crucifix, 2002: Effect of global warming on the length-of-day, *Geophys. Res. Lett.*, **29**, doi:10.1029/2001GL013672.

Egger, J., K.-P. Hoinka, K. M. Weickmann, and H.-P. Huang, 2003: Angular momentum budget based on NCEP and ECMWF reanalysis data: an intercomparison, *Mon. Wea. Rev.*, **131**, 2577-2585.

Egger, J., K. Weickmann, and K.-P. Hoinka, 2007: Angular momentum in the global atmospheric circulation, *Rev. Geophys.*, **45**, RG4007.

Emanuel, K. A., J. D. Neelin, and C. S. Bretherton, 1994: On large-scale circulations in convecting atmospheres, *Q. J. R. Meteor. Soc.*, **120**, 1111-1143

Feldstein, S. B., and S. Lee, 1995: The intraseasonal evolution of angular momentum in aquaplanet and realistic GCMs, *J. Atmos. Sci.*, **52**, 625-649

Gent, Peter R., and Coauthors, 2011: The Community Climate System Model Version 4. *J. Climate*, **24**, 4973–4991. doi: http://dx.doi.org/10.1175/2011JCLI4083.1

Graham, N. E., T. P. Barnett, R. Wilde, M. Ponater, and S. Scuhbert, 1994: On the roles of tropical and midlatitude SSTs in forcing annual to interdecadal variability in the winter Northern Hemisphere circulation. *J. Climate*, **7**, 1416–1442.

Haynes, P. H., C. J. Marks, M. E. McIntyre, M. E. Shepherd, and K. P. Shine, 1991: On the "downward control" of extratropical diabatic circulations by eddy-induced mean zonal forcing, *J. Atmos. Sci.*, **48**, 651-678

Hide, R., and J. O. Dickey, 1991: Earth's variable rotation. *Science*, **253**, 629–637

Hoerling, Martin, and Coauthors, 2011: On North American Decadal Climate for 2011–20. *J. Climate*, **24**, 4519–4528.

Huang, H.-P., P. D. Sardeshmukh, and K. M. Weickmann, 1999: The balance of global angular momentum in a long-term atmospheric data set, *J. Geophys. Res.*, **104**, 2031-2040

Huang, H.-P., P. D. Sardeshmukh, 2000: Another look at the annual and semiannual cycles of atmospheric angular momentum. *J. Climate*, **13**, 3221–3238.

Huang, H.-P., K. M. Weickmann, and C. J. Hsu, 2001: Trend in atmospheric angular momentum in a transient climate change simulation with greenhouse gas and aerosol forcing, *J. Climate*, **14**, 1525-1534

Huang, H.-P., K. M. Weickmann, and R. D. Rosen, 2003: Unusual behavior in atmospheric angular momentum during 1965 and 1972 El Nino, *J. Climate*, **16**, 2526-2539

Huang, H.-P., M. Newman, R. Seager, Y. Kushnir, and Participating CMIP2+ Modeling Groups, 2004: Relationship between Tropical Pacific SST and global atmospheric angular momentum in coupled models, *LDEO Contributions*, Lamont-Doherty Earth Observatory of Columbia University, New York, 43 pp.

Huang, H.-P., R. Seager, Y. Kushnir, 2005: The 1976/77 transition in precipitation over the Americas and the influence of tropical sea surface temperature. *Climate Dyn.*, **24**, 721-740

Ihara, C., and Y. Kushnir, 2009: Change of mean midlatitude westerlies in 21st century climate simulations, *Geophys. Res. Lett.*, **36**, L13701, doi:10.1029/2009GL037674

117

IPCC, 1990: *Climate Change: The IPCC Scientific Assessment* [Houghton, J.T., G.J. Jenkins, and J.J. Ephraums (eds.)]. Cambridge University Press, Cambridge, United Kingdom and New York, NY, USA, 365 pp.

IPCC, 1996: *Climate Change 1995: The Science of Climate Change* [Houghton, J.T., et al. (eds.)]. Cambridge University Press, Cambridge, United Kingdom and New York, NY, USA, 572 pp.

IPCC, 2001: *Climate Change 2001: The Scientific Basis. Contribution of Working Group I to the Third Assessment Report of the Intergovernmental Panel on Climate Change* [Houghton, J.T., et al. (eds.)]. Cambridge University Press, Cambridge, United Kingdom and New York, NY, USA, 881 pp.

IPCC, 2007: *Climate Change 2007: The physical science basis*, Cambridge University Press, 996 pp.

Kalnay, E., and coauthors, 1996: The NCEP/NCAR 40-year reanalysis project. *Bull. Amer. Meteor. Soc.*, **77,** 437–470.

Kanamitsu, M., W. Ebisuzaki, J Woollen, S.-K. Yang, J. J. Hnilo, M. Fiorino, and G. L. Potter, 2002: NCEP-DOE AMIP-II Reanalysis (R-2). *Bull. Amer. Meteor. Soc.*, **83**, 1631–1643.

Kang, I.-S., and K.-M. Lau, 1994: Principal modes of atmospheric circulation anomalies associated with global angular momentum fluctuations, *J. Atmos. Sci.*, **51**, 1194-1205

Kaplan, A., M. Cane, Y. Kushnir, A. Clement, M. Blumenthal, and B. Rajagopalan, 1998: Analyses of global sea surface temperature 1856-1991, *J. Geophys. Res.*, **103**, 18567-18589.

Kaplan, A., Y. Kushnir, M. Cane, and M. Blumenthal, 1997: Reduced space optimal analysis for historical data sets: 136 years of Atlantic sea surface temperatures, *J. Geophys. Res.*, **102**, 27835 – 27860.

Kasahara, A., 1974: Various vertical coordinate systems used for numerical weather prediction, *Mon. Wea. Rev.*, **102**, 509–522.

Kasahara, A., and W. M. Washington, 1967: NCAR global general circulation model of the atmosphere. *Mon. Wea. Rev.*, **95**, 7, 389-402.

Kim, H.-M., P. J. Webster, and J. A. Curry, 2012: Evaluation of short-term climate change prediction in multi-model CMIP5 decadal hindcasts, *Geophys. Res. Lett.*, **39**, L10701, doi:10.1029/2012GL051644.

Kistler, R., and coauthor, 2001: The NCEP-NCAR 50-year reanalysis: monthly means CD-ROM and documentation, *Bull. Amer. Meteor. Soc.*, **82**, 447-267.

Kushner, P. J., I. M. Held, and T. L. Delworth, 2001: Southern hemisphere atmospheric response to global warming, *J. Climate*, **14**, 2238-2249.

Onogi, K., and Coauthors, 2007: The JRA-25 Reanalysis., *J. Meteor. Soc. Japan*, **85**, 369–432.

Richardson, L. F., 1922: *Weather Prediction by Numerical Process*. Cambridge University Press, Cambridge, United Kingdom. 236 pp.

Lambeck, K., 1980: *The Earth's variable rotation*, Cambridge University Press, 449 pp.

Lau, N. -C., 1997: Interactions between Global SST Anomalies and the midlatitude Atmospheric Circulation. *Bull. Amer. Meteor. Soc.*, **78**, 21–33.

Lehmann, E., and P. Névir, 2012: Uncertainties in relative atmospheric angular momentum computed from zonal winds in reanalysis data, *J. Geophys. Res.*, **117**, D09101.

Leith, C. E., 1965: Numerical Simulation of the Earth's Atmosphere, in *Methods in Computational Physics*, eds. B. Alder, S. Fernbach, and M. Rotenberg, Academic Press, 1-28.

Lu, J., G. A. Vecchi, and T. Reichler, 2007: Expansion of the Hadley cell under global warming, *Geophys. Res. Lett.*, **34**, L06805.

Manabe, S., J. Smagorinsky, and R. F. Strickler, 1965: Simulated Climatology of General Circulation with a Hydrologic Cycle, *Mon. Wea. Rev.*, **93**, 769-798.

Manabe, S., and K. Bryan, 1969: Climate Calculations with a Combined Ocean-Atmosphere Model. *J. Atmos. Sci.*, **26**, 786-789

Manabe, S., K. Bryan and M. J. Spelman, 1975: A Global Ocean-Atmosphere Climate Model. Part II. The Atmospheric Circulation. *J. Physical Oceanography* **5**: 30-46.

Manabe, S., R. J. Stouffer, M. J. Spelman and K. Bryan, 1991: Transient responses of a coupled ocean-atmosphere model to gradual changes of atmospheric CO2. Part I: Annual Mean Response. *J. Climate*, **4**, 785-818.

Marcus, S. L., O. de Viron, and J. O. Dickey, 2011: Abrupt atmospheric torque changes and their role in the 1976–1977 climate regime shift. *J. Geophys. Res.*, **116**, D03107.

Marshall, J., R. A. Plumb, 2007: *Atmosphere, Ocean and Climate Dynamics: An Introductory Text*, Academic Press, 344 pp.

Meehl, G. A., A. Hu, and B. D. Santer, 2009: The mid-1970's climate shift in the pacific and the relative roles of forced versus inherent decadal variability, *J. Climate*, **22**, 780-792

Meehl, G. A., C. Covey, T. Delworth, M. Latif, B. McAvaney, J. F. B. Mitchell, R. J. Stouffer, and K. E. Taylor, 2007: The WCRP CMIP3 multi-model dataset: A new era in climate change research, *Bull. Am. Meteor. Soc.*, **88**, 1383-1394

Meehl, G. A., L. Goddard, J. Murphy, R.J. Stouffer, and co-authors, 2009a: Decadal prediction: can it be skillful? *Bull. Am. Meteor. Soc.*, **90**, 1467-1485.

Meehl, G. A., A. Hu, and B. D. Santer, 2009b: The mid-1970s climate shift in the Pacific and the relative roles of forced versus inherent decadal variability, *J. Climate*, **22**, 780-792

Miller, A. J., D. R. Cayan, T. P. Barnett, N. E. Graham, and J. M. Oberhuber, 1994: The 1976-77 climate shift of the Pacific Ocean. *Oceanography*, **7**, 21–26

Mintz, Y., 1965: Very long-term global integration of the primitive equations of atmospheric motion. WMO Tech. Note No. 66; *UCLA Dept. of Meteorology Contribution No. 111*. WMO-IUGG Syrup. on Res. and Develop. Aspects of Long Range Forecasting, Boulder, Colo., 1964. Geneva, 1965, pp. 141-167.

Moss, R. H., and Coauthors, 2010: The next generation of scenarios for climate change research and assessment, *Nature*, **463**, doi:10.1038/nature08823

Nakicenovic, N., and Coauthors, 2000: *IPCC Special Report on Emissions Scenarios*. Cambridge University Press, 599 pp.

Oldenborgh, G.J. van, F.J. Doblas-Reyes, B. Wouters and W. 311 Hazeleger, 2012: Skill in the trend and internal variability in a multi-model decadal prediction ensemble. *Clim. Dyn.*, **38**, 1263-1280, doi:10.1007/s00382-012-1313-4.

Paek, H., H.-P. Huang, 2012a: A Comparison of Decadal-to-Interdecadal Variability and Trend in Reanalysis Datasets Using Atmospheric Angular Momentum. *J. Climate*, **25**, 4750–4758. doi: http://dx.doi.org/10.1175/JCLI-D-11-00358.1

Paek, H., H.-P. Huang, 2012b: A Comparison of the Interannual Variability in Atmospheric Angular Momentum and Length-of-day using multiple Reanalysis datasets. *Journal of Geophysical Research*, **117**, D20102, doi:10.1029/2012JD018105

Peixoto, J. P., and A. H. Oort, 1992: *Physics of Climate*. American Institute of Physics, 520 pp.

Penland, C., P. D. Sardeshmukh, 1995: The Optimal Growth of Tropical Sea Surface Temperature Anomalies. *J. Climate*, **8**, 1999–2024.

Polvani, L. M., D. W. Waugh, G. J. P. Correa and S. -W. Son, 2011: Stratospheric Ozone Depletion: The Main Driver of Twentieth-Century Atmospheric Circulation Changes in the Southern Hemisphere, *J. Climate*, **24**, 795-81

Räsänen, J., 2003: CO2-induced changes in atmospheric angular momentum in CMIP2 experiments, *J. Climate*, **16**, 132-143

Ratcliff, J. T., and R. S. Gross, 2009: Combinations of Earth orientation measurements: SPACE2007, COMB2007, and POLE2007, *JPL Publ.*, 09–18

Rayner, N. A., and Coauthors, 2003: Global analyses of sea surface temperature, sea ice, and night marine air temperature since the late nineteenth century, *J. Geophys. Res.*, **108**, No. D14, 4407 10.1029/2002JD002670

Rienecker, M. M., and Coauthors, 2011: MERRA: NASA's Modern-Era Retrospective Analysis for Research and Applications. *J. Climate*, **24**, 3624–3648.

Rosen, R. D., 1993: The axial momentum balance of Earth and its fluid envelope. *Surv. Geophys.*, **14**, 1–29.

Rosen, R. D., and D. A. Salstein, 1983: Variations in atmospheric angular momentum on global and regional scales and the length of day. *J. Geophys. Res.*, **88**, 5451–5470.

Rosen, R. D., and W. J. Gutowski, 1992: Response of Zonal Winds and Atmospheric Angular Momentum to a Doubling of CO2, *J. Climate*, **5**, 1391–1404.

Saha, S., and Coauthors, 2010: "The NCEP Climate Forecast System Reanalysis. *Bull. Amer. Meteor. Soc.*, **91**, 1015-1057.

Sausen, R., R. Barthel, and K. Hasselmann, 1998: Coupled ocean-atmosphere models with flux correction. *Climate Dyn.*, **2**, 145-163.

Schneider, E. K., M. J. Fennessy, J. L. Kinter, 2009: A Statistical–Dynamical Estimate of Winter ENSO Teleconnections in a Future Climate. *J. Climate*, **22**, 6624–6638.

Seidel, D. J., Q. Fu, W. J. Randel, and T. J. Reichler, 2008: Widening of the tropical belt in a changing climate, *Nature Geoscience,* **1**, 21-24, doi:10.1038/ngeo.2007.38

Sen Gupta, A., L. Muir, J. N. Brown, S. J. Phipps, P. J. Durack, D. Monselesan, S. E. Wijffels, 2012: Climate drift in the CMIP3 models. *J. Climate*, **25**, 4621–4640. doi: http://dx.doi.org/10.1175/JCLI-D-11-00312.1

Smith, T.M., R.W. Reynolds, T. C. Peterson, and J. Lawrimore, 2007: Improvements to NOAA's Historical Merged Land-Ocean Surface Temperature Analysis (1880-2006), *J. Climate*, **21**, 2283 – 2296.

Son, S.-W., L. M. Polvani, D. W. Waugh, H. Akiyoshi, R. Garcia, D. Kinnison, S. Pawson, E. Rozanov, T. G. Shepherd, and K. Shibata, 2008: The impact of stratospheric ozone recovery on the Southern hemisphere westerly jet, *Science*, **320**, 1486-1489

Stephenson, D. B., I. M. Held, 1993: GCM Response of Northern Winter Stationary Waves and Storm Tracks to Increasing Amounts of Carbon Dioxide. *J. Climate*, **6**, 1859–1870.

Taylor, k. E., R. J. Stouffer, and G. A. Meehl, 2012: An overview of CMIP5 and the experiment design, *Bull. Am. Meteor. Soc.*, **93**, 485-498

Thorne, P. W., and R. S. Vose, 2010: Reanalyses suitable for characterizing long-term trends: Are they really achievable? *Bull. Amer. Meteor. Soc.*, **91**, 353–361.

Thorne, P. W., and R. S. Vose, 2011: Reply. *Bull. Amer. Meteor. Soc.*, **92**, 70–72.

Trenberth, K. E., 1990: Recently observed interdecadal climate changes in the Northern Hemisphere, *Bull. Amer. Meteor. Soc.*, **71**, 988-993

Trenberth, K. E., 1996: El Niño Definition, *Exchanges, Newsletter of the Climate Variability and Predictability Programme (CLIVAR)*, Volume 1, No.3, 6-8.

Uppala, S. M., and coauthors, 2005: The ERA-40 re-analysis, *Quart. J. R. Meteorol. Soc.*, **131**, 2961-3012

Veerse F., Thepaut J-N., 1998: Multiple-truncation incremental approach for four-dimensional variational data assimilation. *Q. J. R. Meteorol. Soc.,* **124**: 1889–1908.

Von Storch, H., and F. W. Zwiers, 2002: *Statistical analysis in climate research*, Cambridge University Press, 496 pp.

Weickmann, K. M., G. N. Kiladis, and P. D. Sardeshmukh, 1997: The dynamics of intraseasonal atmospheric angular momentum oscillations, *J. Atmos. Sci*., **54**, 1445-1461

Whitaker, J. S., G. P. Compo, X. Wei, and T. M. Hamill, 2004: reanalysis without radiosondes using ensemble data assimilation, *Mon. Wea. Rev.*, **132**, 1190-1200

Yin, J. H., 2005: A consistent poleward shift of the storm tracks in simulations of the 21st century climate, *Geophys. Res. Lett.*, **32**, L18701, doi:10.1029/2005GL023684